

DIGITAL ACCESS TO SCHOLARSHIP AT HARVARD
DASH.HARVARD.EDU

HARVARD LIBRARY


Single Atom Detection via Transparency Techniques

Citation

Sumarac, Tamara. 2024. Single Atom Detection via Transparency Techniques. Doctoral dissertation, Harvard University Graduate School of Arts and Sciences.

Link

https://nrs.harvard.edu/URN-3:HUL.INSTREPOS:37379817

Terms of use

This article was downloaded from Harvard University's DASH repository, and is made available under the terms and conditions applicable to Other Posted Material (LAA), as set forth at

https://harvardwiki.atlassian.net/wiki/external/NGY5NDE4ZjgzNTc5NDQzMGIzZWZhMGFlOWI2M2EwYTg

Accessibility

https://accessibility.huit.harvard.edu/digital-accessibility-policy

Share Your Story

The Harvard community has made this article openly available.
Please share how this access benefits you. Submit a story

HARVARD
Kenneth C. Griffin

GRADUATE SCHOOL
OF ARTS AND SCIENCES

THESIS ACCEPTANCE CERTIFICATE

The undersigned, appointed by the

Department of Physics

have examined a dissertation entitled

Single Atom Detection via Transparency Techniques

presented by Tamara Sumarac

candidate for the degree of Doctor of Philosophy and hereby certify that it is worthy of acceptance.

Signature _____

Typed name: Prof. Mikhail Lukin

Signature _____

Typed name: Prof. Vladan Vuletić (MIT)

Signature _____

Typed name: Prof. Philip Kim

Date: August 23, 2024

Single Atom Detection via Transparency Techniques

A DISSERTATION PRESENTED
BY
TAMARA ŠUMARAC
TO
THE DEPARTMENT OF PHYSICS

IN PARTIAL FULFILLMENT OF THE REQUIREMENTS
FOR THE DEGREE OF
DOCTOR OF PHILOSOPHY
IN THE SUBJECT OF
PHYSICS

HARVARD UNIVERSITY
CAMBRIDGE, MASSACHUSETTS
AUGUST 2024

©2024 – Tamara Šumarac
all rights reserved.

Thesis advisor: Professor Vladan Vuletić, Mikhail D. Lukin Tamara Šumarac

Single Atom Detection via Transparency Techniques

Abstract

Over the last decade, atom arrays have emerged as a powerful platform for quantum technologies, enabling applications in simulation, computation, metrology and sensing. While having many unique features especially useful for quantum computing, there are areas where this platform can be improved, and this thesis presents tools developed to enhance its speed. The first tool developed is a fast non-destructive qubit readout, intended for improving computational speed of this platform, in particular, mid-circuit measurements. This method utilizes tweezers filled with ensembles of atoms to collectively readout a single Rydberg qubit via Electromagnetically Induced Transparency (EIT) improving readout speed by several orders of magnitude compared to conventional methods. We test several configurations of these ensemble detectors and provide an understanding of the underlying physical mechanisms in each scenario. The second tool developed is a method for single-atom loading and imaging in high magnetic fields, based on combination of fluorescence imaging, responsible for detection, and D_2 EIT cooling, responsible for preserving the atoms during detection. This tool, combined with continuous loading technique, has the potential to reduce the experimental cycle time of the neutral atom platform by several orders of magnitude. While work in this thesis primarily focused on developing more efficient quantum computing apparatus for single atom arrays, an accidental discovery during this research led to the creation of a Bose-Einstein Condensate (BEC) inside a micro-ensemble using only polarization gradient cooling (PGC). This finding challenges the long-held belief that PGC alone is insufficient to generate BEC, and illustrates the non-linear nature of the research process, where interesting discoveries can occur unexpectedly.

Contents

Title Page **i**

Copyright **ii**

Abstract **iii**

Table of Contents **iv**

Dedication **viii**

Acknowledgments **ix**

Citations to previously published work **xiii**

1 Introduction **1**
- 1.1 Thesis overview . . . 6

2 Theory and Experimental Techniques for Neutral Atom Experiments **8**
- 2.1 Neutral atoms introduction . . . 8
- 2.2 Vacuum chamber . . . 10
- 2.3 Laser trapping . . . 15
- 2.4 Laser cooling . . . 19
- 2.5 Imaging . . . 25
- 2.6 Micro-ensemble generation by blue-detuned squeezing . . . 28

3 Theory and Experimental techniques for Rydberg atoms **32**
- 3.1 Theory . . . 32
- 3.2 Finding Rydberg transitions . . . 35
- 3.3 Electric field zeroing . . . 37
- 3.4 Rydberg state preparation using microwave drive . . . 39
- 3.5 Rydberg lifetime and coherence time measurements . . . 40

4 Electromagnetically Induced Transparency 42
4.1 Introduction . . . 42
4.2 Theory . . . 43
4.3 Rydberg EIT . . . 46
4.4 EIT for cooling . . . 48

5 Fast, local Rydberg qubit detection 51
5.1 Introduction . . . 51
5.2 Fast neutral atom detectors . . . 52
5.3 Our detection scheme based on Rydberg EIT . . . 52
5.4 Experimental parameters . . . 54
5.5 Detection results . . . 54
5.6 Rydberg qubit within a micro-ensemble . . . 57
5.7 Probability that single Rydberg atom is prepared . . . 58
5.8 Qubit coherence time . . . 58
5.9 Conclusion and Outlook . . . 60

6 Bose-Einstein condensation by polarization gradient laser cooling 62
6.1 Introduction . . . 62
6.2 Experimental setup and machine learning optimized trap loading . . . 64
6.3 BEC observation in a time of flight measurement . . . 66
6.4 Dimple hypothesis . . . 67
6.5 Dimple hypothesis - experimental tests . . . 69
6.5.1 BEC formation dependence on the trap waist and alignment . . . 69
6.5.2 BEC formation on-demand using SLM . . . 69
6.6 Loss of BEC atoms during time-of-flight . . . 70
6.7 Conclusion and outlook . . . 71

7 Long range detection of a single Rydberg atom via hopping with Rydberg polaritons 73
7.1 Introduction . . . 73
7.2 Experimental setup . . . 75
7.3 Interaction model and regimes . . . 77
7.4 Control over the Rydberg atom-polariton interaction regime . . . 78
7.5 Non-local Readout of a Rydberg qubit using Rydberg polaritons . . . 81
7.6 Conclusion and outlook . . . 83

8 High Magnetic Field Loading and Imaging of Single Atom Arrays 84
8.1 Introduction . . . 84
8.2 Experimental setup . . . 86
8.3 Results . . . 88

8.4 Conclusion and outlook 92

9 Conclusion and Outlook 94
9.1 Summary 94
9.2 Outlook 95
9.2.1 Array of micro-ensembles next to an array of single atoms for fast mid-circuit readout 96
9.2.2 Fast cycle time setup 97

Appendix A Supplement for chapter 5 100
A.1 Experimental setup 100
A.2 Preparation of an atom in the Rydberg state 101
A.3 Loss of the Rydberg atom and creation of Rydberg impurity during detection . . 102
A.4 Repeated (non-destructive) detection 105
A.5 Measurements of Rabi oscillations 106
A.6 Rydberg blockade 107

Appendix B Supplement for chapter 6 109
B.1 Gallery of observed BECs 109
B.2 Machine Learning Optimization 110
B.3 Definition of classical phase space density 113
B.4 Hyperfine states of atoms 114
B.5 Dipole trap extinction measurements 114
B.6 Three-body loss in TOF 115
B.7 Atom number fitting procedure 116

Appendix C Supplement for chapter 7 117
C.1 Experimental Setup 117
C.2 Three-photon preparation 118
C.3 Site-selective preparation and detection using AOD on the control field 119
C.4 Choice of Rydberg states: $D - P$ vs. $S - P$ 120
C.5 Full interaction space experiment 122
C.6 Evidence of Rydberg blockade 122
C.7 Evidence of dipolar hopping: experimental details 124
C.8 Parameters affecting detection fidelity 125
C.9 Microwave Rabi oscillation: experimental details 127
C.10 Rydberg coherence time 127
C.11 Multiple Rydberg detectors experiment 128
C.12 Our phenomenological theory 129

Appendix D Supplement for chapter 8 131

D.1 Experimental Setup 131
D.2 Monte Carlo temperature fit details 132
D.3 2D High B field imaging 133
D.4 Imaging dependence on trap depth 134

References **151**

To Dragoslav, Slavica, Miloš, Sandra and my Boris

Acknowledgments

My PhD journey has been an incredibly transformative period, and I am deeply thankful for the experiences and the people who have significantly impacted me.

First and foremost, I would like to thank my advisors. Working with Prof. Vladan Vuletić has convinced me that Nikola Tesla is the second-best scientist Serbia has ever produced, with Vladan being the first (not me). It is impossible to count the times Vladan's intuition pinpointed the issues we faced in the lab, even when our explanations were confusing and puzzling. I am infinitely grateful for the opportunity to learn from his approach of doing things well enough and moving on, rather than surrendering to perfectionist ideals. This mindset has transformed me from a "thinker" and "philosopher" into a "doer", a change for which I will forever be thankful to Vladan. Additionally, I appreciate Vladan's patience and mentorship; his responses to questions never revealed whether they were stupid, and there certainly were many such questions.

Prof. Mikhail D. Lukin was my primary advisor for the first three years of PhD. Although the project we worked on, not described in this thesis, never worked out, I am truly grateful I had the chance to work with Misha. His cheerleading attitude, trust, and belief in me meant the world. I learned so much from his way of instilling optimism and drive in others, while allowing a lot of freedom, inspiring students to give their utmost effort. I hope to carry these lessons into the next stages of my life. I am forever grateful to him for the education I received on AMO and Quantum Information topics through his well-designed classes, and for his pioneering work on Electromagnetically Induced Transparency, which was the basis of the large part of my thesis.

I would also like to thank Prof. Philip Kim for serving on my thesis committee and always being very supportive and available for our progress report meetings.

The work presented in this thesis is the result of contributions from a group of dedicated individuals who worked with me on these projects. I would especially like to thank Wenchao Xu, with whom I overlapped for three years, including one and a half years spent building a new setup. I learned so much from her example, from work ethic to problem-solving techniques. She would always think of the new tool to develop in order to debug the problem and her statement "we are different from animals because we can build tools" will always stay with me.

I am also very grateful to Aditya Venkatramani and Sergio Cantú for their teachings and support during my transition into their lab. Aditya taught me so much about running experiments, and I have notes on every move and click he made as we worked together on the local Rydberg detection project. I am continually inspired by his brilliance and optimism. Sergio is a type of person that can debug

anything in lab. I am grateful I had the opportunity to experience a few things breaking in the lab while he was there and to witness his debugging wizardry firsthand.

During my PhD, I had the privilege of mentoring several students in the lab, with Emily Qiu being one of the first. Even when she just started, she was impressively skillful and independent, efficiently completing her projects and quickly engaging in experimental developments. Over the years, our relationship evolved from mentor and mentee to partners, forming a fantastic team by the end of my PhD. I really enjoyed our physics discussions both in the lab and out, and it was super fun debugging many confusing signals together. I greatly appreciate her dedication to maintaining thorough documentation, keeping the lab organized, and contributing to a positive lab atmosphere. It was a pleasure to see her grow as a researcher, and I am really excited to see where the experiment will go under her leadership. I am so glad she is the person with whom I had the longest overlap in PhD, as working with Emily made the everyday struggles of experimental work far more enjoyable.

Other junior students I worked with were Matthew Peters and Peiran Niu. I am grateful to them for being very efficient in their projects and respectful young male colleagues. I am especially grateful to Matthew for his tech wizardry and for updating our software system to labscript, that our lab greatly benefited from.

I am also grateful to Shai Tsesses, a postdoc in our lab who joined during my last year. His optimism and strategic thinking were invaluable during the final, most productive year of my PhD.

I am thankful to Adrian Menssen, a postdoc collaborator who worked with us part-time for the last two years of my PhD, for many engaging discussions on both physics and non-physics topics. I greatly appreciated his efforts in keeping our fun lunch club alive.

I am also grateful to Simone Colombo, Zeyang Li, Ashish Kalakuntla, Valentin Klüsener and Ashrit Verma for their contributions to the experiment; Christoph Hotter and Valentin Walther for collaborating with us on theory.

Before joining Vladan's lab, I worked in Misha's lab on an NV project, where I met many people I need to acknowledge. I spent large portion of that time working with Elana Urbach and Helena Knowles. I am thankful to them for being the NV know-how and introducing me to American culture. I am especially thankful to Elana and Kristine Rezai for introducing me to weightlifting and making it enjoyable with fun gossip sessions. The 7 a.m. morning discussions with Javier Sanchez-Yamagishi were invaluable, and I am deeply grateful for his encouraging words, especially when I needed them most. Despite spending only couple of months with Igor Lovchinsky, I am so grateful that he kept in touch with me after he graduated. I am also grateful to our collaborators Soonwon Choi, Bo Dwyer, Trond Andersen, Ryan Cimino, Philip Vetter, Alexei Bylinskii, Nabeel Aslam, Kristian de Greve and Nathalie de Leon for their helpful contributions and Joonhee Choi, Harry Zhou, Renate Landig and Emma Rosenfeld for fun physics discussions.

The transitional time between NV field and cold atoms was emotionally hard and there are couple of people that really helped me through this time. I am thankful to Alex Keesling for being an incredibly supportive friend and a fun person to be around not just during this time but in general. I am especially grateful for him providing the insights that helped me join the right team and complete my PhD happily. I am also thankful to Ruffin Evans for his support and I am especially grateful for his guidance in helping me communicate my decision to switch fields.

I also benefited a lot from discussions with many other people from these groups. In Vladan's group I am thankful to Zak Vendeiro for his invaluable documentation and insightful thesis that helped us in many debugs. Enrique Mendez was very helpful with MLOOP debugging and made fun lunches even more fun. I am also grateful to Beili Hu, Alyssa Rudelis, Eugene Knyazev, Josiah Sinclair, David Spierings, Guoqing Wang for their helpful debugging tips. More broadly, I would like to thank all members of Vladan's and Misha's groups for sharing their knowledge, which we used daily in the lab, and for fostering a fun lab atmosphere.

I am also grateful for the opportunity to be a teaching assistant for Prof. Markus Greiner's lab class on Optics and Waves, which brought me an incredible amount of enthusiasm for physics.

I am very thankful to the Harvard Physics Department for their outstanding efforts to improve student life, especially by establishing the G1 lounge, which greatly improved connections within our cohort. I am especially thankful to Lisa Cacciabaudo, Carol Davis and Jacob Barandes for their helpful advice and their patience in answering my many questions. Additionally, I appreciate Samantha Dakoulas for everything she did and for always being a fun person to talk to.

Through this time I've made a lot of friends who feel like family. Tamara Đorđević and Giovanni Scuri literally became my family by asking me to be kuma at their weddings. I am grateful for fun years we spent together at 10 Soden Street, many Thanksgivings, bbqs, movie nights, fun Stoja parties we had together and I am also honoured to have been invited to all three of their weddings. With Sarah Battat, I developed a deep friendship that usually forms only during childhood. We had so many fun discussions over dinners, shared enthusiasm for putting eyeliner on every day and it was super fun working late into the night in the department together and taking Harvard shuttle bus home. Houri Tarazi is also a friend I consider family. We met in our first year on the hallway in our dorm and bonded over our shared Balkan heritage. Since then, we've attended numerous parties together, spent Thanksgivings, and had lively, controversial discussions during COVID Christmases.

There are also friends that have continued to be family even with us being far apart. Every interaction with Tamara Čukić, Andrijana Janjušević, Matej Milićević, Nevena Nikolić, Emily Bloch and Dimitra Pefkou feels as if no time has passed and we always find something fun to do or a fun gossip to share. With Emily and Dimitra I had a pleasure of spending good amount of time in Boston too, creating countless memorable moments.

During my PhD, I stayed connected to my roots through many fun Serbian/Balkan groups. The initial core group included Tamara Đorđević, Denis Božić, Nataša Dragović, Djordje Radičević, and Ignat Kalinov ♡. Ana Trišović, Maja Kulić, Ognjen Marković, and Petar Stojanov were integral parts of our "Kvantni Sistemi" group, filled with many internal jokes. We also enjoyed memorable trip to Arizona with our Balkan friends from both the west and east coasts. It was incredibly fun to keep the culture alive with these people.

Before starting my PhD, several people instilled in me a love for physics that kept me motivated on this journey. My high school, Matematička Gimnazija, fostered an environment where I grew up among peers who were as passionate about STEM fields as I was and it also provided us with excellent physics and math professors who helped us develop our skills early on. Nataša Čaluković wrote books that have inspired every young Serbian physicist to pursue physics research. At university, I am particularly grateful to Zoran Hadžibabić for all the knowledge and advice he shared with me. His

cool approach to physics showed me that you can be both a great physicist and a cool person. During my undergraduate time, I also worked in the labs of Akio Kawasaki and Boris Braverman in Vladan Vuletić's group, as well as lab of Tony Zhou in Amir Yacoby's group. I am grateful to professors for the opportunity they provided and thankful to these students for their mentorship, which further solidified my decision to pursue a PhD in physics.

Finally, I would like to thank my parents Dragoslav and Slavica, who have always supported me in everything I do. They provide an example of resilience and determination despite all of life's challenges. My brother Miloš and sister Sandra have greatly influenced the person I am today. I am especially grateful to Sandra for being the coolest sister and always reminding me of the importance of fashion. I cherish the many years we spent with our dog Džesika ♡. I am grateful to my extended family, especially my aunts and "sisters", for staying in touch and providing invaluable support over the years. Lastly, I would like to thank my life constant for the last 12 years, my Boris. Words cannot fully describe how patient and supportive Boris has been throughout my PhD journey. With my graduation, I feel he has also earned a PhD in listening and cheerleading. I am so grateful for his calm attitude and approach to life and I am continually amazed by his smarts and curiosity. I am also thankful to his wonderful huge family for always making our time together fun.

Citations to previously published work

Parts of this dissertation cover research reported in the following articles:

Chapter 5 and Appendix A have been published as

> "Fast Preparation and Detection of a Rydberg Qubit Using Atomic Ensembles", W. Xu*, A. V. Venkatramani*, S. H. Cantú*, T. Šumarac, V. Klüsener, M. D. Lukin, V. Vuletić, *Physical Review Letters*, 127, 050501 (2021).

Chapter 6 and Appendix B have been published as

> "Bose-Einstein Condensation by Polarization Gradient Laser Cooling", W. Xu*, T. Šumarac*, E. H. Qiu*, M. L. Peters*, S. H. Cantú, Z. Li, A. Menssen, M. D. Lukin, S. Colombo, V. Vuletić, *Physical Review Letters*, 132, 233401 (2024).

The material contained in Chapter 7 and Appendix C is currently in preparation for publication.

The material contained in Chapter 8 and Appendix D is currently in preparation for publication.

Chapter 3 contains content from Supplementary Material of Chapter 7.

* These authors contributed equally to this work.

1

Introduction

Physics stories often start with researchers having a clear goal in mind and working linearly towards achieving that specific goal. However, in reality, it is often difficult to fully and very clearly motivate why we do what we do until things get done. One explanation for why we do what we do, that I believe is certainly true, is that we, as humans, have an inherent desire to make tools, build things, and understand and explore the universe we live in.

This thesis follows a similar pattern: we have a general vision of our future goals and the type of

device we aim to construct. However, intrinsically, we are also very motivated by the development of tools and equipment needed to reach these goals, and we become fascinated by learning about how our universe works, and in the case of this thesis, how our quantum universe works.

Quantum physics has been an intriguing topic for more than a century now. Unlike classical physics, which describes the macroscopic world we can see and intuitively understand, quantum physics describes the behavior of particles at the microscopic level, where particles no longer behave deterministically, but can also show their probabilistic nature. It first emerged as a way to explain a few puzzling experiments in late 1800s, early 1900s that could not be explained with classical physics including black-body radiation and the photoelectric effect. These experiments motivated theoretical developments that laid the foundation for quantum mechanics, introducing the concepts such as quantized energy and discrete packets of light called photons.

Theory of quantum mechanics continued to be developed further in 20s and 30s that gave us famous formulations and postulates, that we use every day in lab. Some famous concepts include wave-particle duality, which proposes that particles, such as electrons, exhibit both wave-like and particle-like properties; the Heisenberg uncertainty principle, which states that it is impossible to simultaneously know both the position and momentum of a particle with absolute precision; and the Schrödinger wave equation which describes how the quantum state of a physical system changes over time. Majority of these concepts were observed and utilized in my experiments, with the Schrödinger equation being one that I've likely written at least a hundred or several hundred times throughout my PhD.

One might question the importance of studying a field that seems so detached from everyday experiences. Why would it be helpful to know that electron can behave both like particle and like wave, when in real life we mostly experience it as a particle. However, this perception is far from right, and this can be appreciated only in hindsight. We now know that understanding the "unseen" quantum nature of the microscopic world has revolutionized our modern technology. Semiconductors, which

are fundamental to the computers we use daily, rely on principles of quantum mechanics. Lasers, essential for the functioning of the internet and various communication technologies, also depend on quantum properties. Furthermore, medical diagnostic tools like magnetic resonance imaging (MRI), operate based on quantum mechanics. These are just a few examples of how studying quantum mechanics has led to the development of technologies that are integral to contemporary life.

In the last 50 years a new technology inspired by quantum mechanics has emerged called quantum computing. It all started in 1980s when Richard Feynman, proposed the idea that classical computers are inherently inefficient at simulating quantum systems due to the exponential growth of computational resources required and he introduced the concept of quantum computing, where quantum bits (qubits) could exist in superpositions and be entangled, allowing quantum computers to perform many calculations simultaneously. He motivated the use of quantum computers to simulate quantum physics problems more efficiently than classical computers [1].

Since then, serious theory and experimental efforts have been invested in this direction. At this point we believe that quantum computing, apart from answering physics questions by simulating complex systems [2,3,4,5], can also be useful in enhancing our technology particularly in cryptography [6], materials science [7] and drug discovery [8]. These goals provide motivation for such system to be built, but as history thought us, developing this technology will probably also result in tools we cannot even predict today.

Currently, numerous systems have demonstrated qubit behavior, but only a few have demonstrated high level of controllability at scale, which is essential for creating a practical quantum computer. Among these, superconducting qubits [9], trapped ions [10], and neutral atoms [11] stand out. Each of these systems has followed a different development path over the years and has their own advantages and disadvantages, but the platform of choice in this thesis is the neutral atom platform.

Neutral atoms have been studied for the longest out of qubit candidates, long before quantum computing gained traction. Initially the focus was on developing laser techniques for trapping [12], cool-

ing[13] and manipulating atoms, and this technology allowed us to detect new phases of matter including Bose-Einstein condensation[14,15], where a collection of atoms behaves like a single wave, exhibiting quantum mechanical properties on a macroscopic scale. Additionally, this technology improved the accuracy of atomic clocks[16], which are important for GPS, telecommunications, and fundamental physics tests.

Until recently, neutral atoms have not been considered serious candidates for quantum computing due to several inherent challenges. For example, trapping individual atoms in optical dipole traps (tweezers) has a stochastic filling probability, typically of $50\,\%$[17]. If we want to fill out a specific array of traps, with stochastic filling, that would result in different configurations of arrays filled for each experimental run. For quantum computing, this means that the computation results would need to be post-selected for a certain circuit connectivity, which would severely limit the platform's scalability and the feasibility of achieving a quantum speedup. This problem was largely overcome by applying real-time feedback to optical tweezers[18,19,20]. Atoms can now be loaded, imaged, and subsequently, deterministically rearranged into fully filled arrays of arbitrary geometries in 1D, 2D and even 3D[21].

Another significant challenge with neutral atoms is that they are inherently neutral, and thus, they do not interact with their environment much, making it difficult to create two-qubit gates for which interaction is essential. To overcome this, neutral atoms can be excited to high-lying Rydberg states[22], where they behave like large electric dipoles, and, as such, they can interact very strongly with each other. This feature has been explored extensively[23], but two-qubit gate fidelity remained at around $80 - 90\,\%$ for some time. Recently, with technical improvements in laser control and excitation schemes, excess of $99\,\%$ fidelity for both single-qubit and two-qubit gates was achieved in several platforms including ^{87}Rb[24], ^{88}Sr[25] and ^{171}Yb[26].

These developments have unlocked very unique features of neutral atoms that are particularly useful for quantum computing. For example, with deterministic loading, large scales with neutral atoms can be achieved, making scalability one of the platform's strongest attributes. Nowadays sys-

tems with hundreds of atoms are routinely achieved[27,28,29] and a recent demonstration included a system size of even 6100 qubits[30]. Furthermore, it was demonstrated that this platform can be controlled at the excess of 99% gate fidelities at these large scales. The initial challenge of stochastic loading led to the development of tools, that now allow for another unique feature of the system where computing architectures can be modified mid-sequence[31]. The high quality level of control, paired with re-configurable architecture at scale, facilitated recent demonstration of encoded logical qubits – a key milestone towards error-corrected logical qubits and fault-tolerant computation[11].

While all these features make neutral atom platform very appealing, there are areas for improvement, especially in platform speed. Compared to typical experimental cycle times of superconducting qubits, ranging from microseconds to milliseconds, neutral atom speeds are on the order of seconds, which is considerably slower. This speed can limit the platform's applicability to problems requiring faster data rates[32], and experimental drift occurring on this timescale can negatively affect qubit control fidelities. Hence, improving these systems such that they operate at fast timescales remains an important goal.

The major limitation to the platform's speed is the loading and preparation of fully filled arrays of single atoms, typically taking several hundred milliseconds to half a second. This issue is envisioned to be mitigated in the future by operating neutral atom experiments in fully continuous mode, which would require developing methods to continuously load and image atoms at high magnetic fields. Recent efforts towards continuous loading of atoms have validated the promise of this idea[33,34,35], but single-atom loading and imaging in high magnetic fields have yet to be demonstrated for alkali atoms. On the computational side, gate operations are typically shorter than a microsecond, but the slow qubit readout, usually taking several tens of milliseconds, is the computational speed bottleneck, especially for error-correction methods requiring several mid-circuit readouts to be performed[36].

The work in this thesis focused on developing tools to improve the speed of neutral atom platform. Specifically, we developed a fast, non-destructive imaging technique intended for mid-circuit

readout, and a method for single-atom loading and imaging in high magnetic fields to enable fully continuous operation mode. The method for fast non-destructive readout utilizes tweezers filled with ensembles of atoms that collectively readout a single Rydberg qubit via Electromagnetically Induced Transparency (EIT). This idea was tested in two cases, when Rydberg qubit is placed inside the ensemble detector and when placed outside. Our study shows that detection works in both cases, though with better fidelity when qubit is placed inside the ensemble. We also found that physics mechanism behind detection is different in two cases, driven by the competition between Rydberg blockade and Rydberg exchange interaction mediated by the same dipole-dipole interaction. While modifying the setup to host both single atom tweezers and ensemble detector tweezers, we worked on resolving the issue of single atom loading and imaging in high magnetic fields. We found that combination of fluorescence imaging, responsible for detection, and D2 EIT cooling, responsible for preserving the atoms during detection, fixes this problem. While developing this quantum computing apparatus we stumbled upon a physics observation, that was not in our original goal, as we accidentally created Bose-Einstein condensation using the simplest form of cooling, polarization gradient cooling (PGC), overturning a long-held paradigm that PGC alone is insufficient for reaching quantum degeneracy.

1.1 Thesis overview

This thesis is structured as follows: the first three chapters provide the theoretical and experimental background necessary to understand the experimental results presented in the subsequent four chapters.

Chapter 2 provides theoretical understanding and experimental techniques for trapping, cooling and imaging of neutral atoms, including methods specific to our setup, such as generating round micro-ensemble arrays. Chapter 3 provides theory and experimental background to understand Rydberg atoms. Chapter 4 describes Electromagnetically Induced Transparency, the main technique used

for both detection methods explored in this thesis. Theoretical background is provided for both the resonant case, explored in Chapters 5 and 7, and the off-resonant case important for cooling used in Chapter 8.

The subsequent chapters focus on experimental results. Chapters 5 and 7, along with their respective appendices, provide one story together, of using Rydberg EIT on micro-ensemble arrays to speed up the readout process of single atoms in a non-destructive way, useful for the mid-circuit measurements. Chapter 5 provides a result where Rydberg atom was prepared inside the detector micro-ensemble, while in Chapter 7, Rydberg atom was prepared and positioned outside of the detector micro-ensemble. Chapter 7, specifically in its appendix, also provides a theoretical model explaining the difference in detection mechanism between Chapter 5 and Chapter 7, governed by the competition between Rydberg blockade and Rydberg exchange interaction mediated by the same dipole-dipole interaction.

Chapters 6 to 8 were conducted in a completely renovated setup, including a new vacuum chamber that I, alongside my team mates, assembled in late 2020 and early 2021. Chapter 6 details accidental discovery of Bose-Einstein condensate while attempting to generate arrays of small micro-ensembles, intended for the use in Chapter 7, and optimizing their density via machine learning. Finally, Chapter 8 provides our results on achieving single atom loading and imaging in high magnetic fields.

2

Theory and Experimental Techniques for Neutral Atom Experiments

2.1 Neutral atoms introduction

Over the last 40 years, the cold atom platform has emerged as one of the leading experimental systems for studying quantum phenomena. During this time, the community has made significant progress,

resulting in key discoveries such as the Bose-Einstein Condensate and the development of highly precise atomic clocks. These advancements have paved the way for the use of cold atom systems in constructing small-scale quantum computers.

What makes this platform so powerful and versatile is the wide-range of tools that have been developed for it over these decades. It began with pioneering efforts in creating laser cooling [13] and trapping techniques [12], which provided essential tools for isolating and controlling small collections of atoms and even individual atoms. This progress allowed us to cool these atoms to ultra-low temperatures, where atoms behavior can be dominated by quantum effects, leading to the first experimental realization of the Bose-Einstein condensate. While laser techniques and controls were being developed, laser technology was also improving, and combination of these gave us very precise lasers and very advanced controls for manipulating internal states of atoms leading to a development of very precise atomic clocks. In the last decade, addition of various diffraction tools, has sparked another revolution in the field, where precise arrangement of arrays of single atoms on arbitrary grids, extending to sizes of several hundred and even thousands of atoms is now possible. The integration of these tools has allowed the neutral atom community to venture into the quantum computation and quantum simulation space, establishing itself as one of the forefront platforms of quantum computing research.

In this chapter, I will introduce all these instrumental tools for cold atom experiments that my teammates and I developed, which enabled the experiments in this thesis. Starting with an empty table and an open vacuum chamber, I was fortunate to be involved and lead the development of these tools from scratch. This chapter is organized as follows: First, I will provide a brief introduction to the standard techniques in the field and detail how we implemented them in our system, including the design and assembly of the vacuum chamber, laser trapping, laser cooling, and standard imaging techniques such as absorption and fluorescence. Finally, I will present some specific, non-standard, techniques we developed for our system, such as the method for generating micro-ensembles with small aspect ratios, which was crucial for the fast non-destructive Rydberg detection project.

2.2 Vacuum chamber

The first step in every cold atom experiment sequence is laser cooling and trapping. Unfortunately, typical optical dipole traps are not very deep, meaning, if these traps were generated in atmospheric pressure environment, atoms that we want to trap, in this thesis case ^{87}Rb atoms, would be easily ejected out of the trap due to collisions with surrounding atoms, including atoms from the air such as oxygen and nitrogen. To prevent this from happening, cold atoms need to be generated in low vacuum pressure environments, typically ranging from $10^{-8} - 10^{-9}$ Torr pressure, or with ever increasing system sizes, even stricter requirements of $10^{-12} - 10^{-13}$ Torr pressure levels are needed. To get a sense how low this pressure is, this pressure level is comparable to the pressure found between the Earth and the Moon!

To reach this low pressure level, standard techniques in the community involve using series of pumps including roughing pump, turbo pump, ion pump and titanium sublimation pump, that we also used to create our own vacuum. However, using these techniques alone would not get us to the pressure levels needed for these experiments. In order to do that, one needs to additionally bake the vacuum chamber at high temperatures for few days while pumping, to get rid of any buildup of the material on the chamber walls, that would otherwise limit the vacuum pressure that can be achieved.

By applying all these techniques, we achieved a vacuum pressure of 2×10^{-10} Torr, which was sufficient for our purposes. Pressure level that we achieved was constrained by the temperature at which we baked the chamber, that was limited by the in-vacuum components, in particular achromatic lenses, as it will be described below.

In the middle of COVID-19, in late 2020 and early 2021, we assembled a new vacuum chamber for our experiment, completing the baking process on January 26, 2021. The new vacuum chamber is an upgraded version of the vacuum chamber as described in Thibault's thesis [37] with the full assembly presented in Figure 2.1. The majority of upgrades focused on improving the optical access to the

a) Side view x-z direction

b) Top view

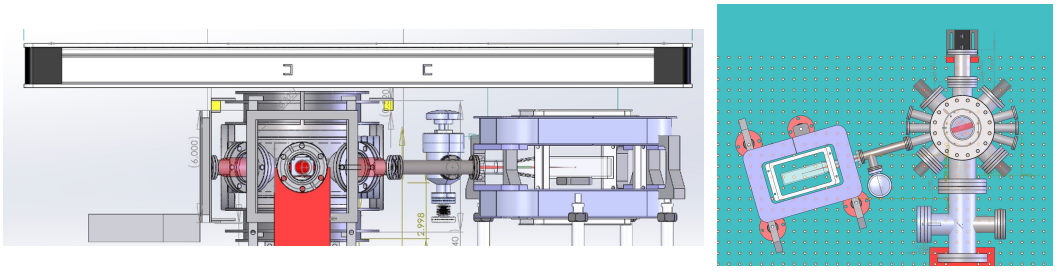


Figure 2.1: Schematic of an upgraded vacuum chamber: a. Side view of the chamber showing glass cell and the steel chamber (main chamber) connected via differential pumping stage. Bellow that holds Rb ampule is connected to the glass cell side via valve that controls the level of Rb atoms in the glass cell and the main chamber. **b.** Top view of the chamber illustrating the angle at which the glass cell is oriented relative to the main chamber. This view also shows the cross-nipple with a 45° in-vacuum mirror that was added to allow optical access along the y direction that was not available before the upgrade.

atoms and eliminating obsolete components from the old chamber. The main upgrades include:

1. **Substitution of the Re-entrant Viewports:** Two flat vertical $6''$ viewports were replaced with two re-entrant bucket windows, providing better optical access to the atoms in vertical direction, where now we can use up to $NA = 0.65$ lens at this window, compared to about $NA = 0.25$ that was available without this upgrade.

2. **Removal of Channeltron:** The obsolete Rydberg detector, channeltron, was removed, and a flat $2.75''$ viewport was added at that flange, which allowed for optical access along y direction that was not available before the upgrade.

3. **Cross-Nipple Addition:** A cross-nipple with a 45° in-vacuum mirror was added to allow for the optical access on the other side of the chamber along the y direction.

4. **Lens Cage Mount:** A four lens cage mount with four new in-vacuum lenses was installed to improve optical access to atoms along the x and y direction.

5. **Electric Field Plates:** New electric field plates were mounted on the lens-cage mount, and these plates were essential in zeroing of electric fields for Rydberg atom experiments.

6. **Glass Cell Addition:** A glass cell with a differential-pumping stage was added, connecting it to the main chamber. The main purpose of the glass cell was to allow for chamber to have two parts that can be separately controlled, which is useful for continuous loading techniques[33,34,35].

7. **Rubidium Source:** We changed the rubidium source for the new chamber from dispensers to ampule that is held inside the bellow connected via valve to the glass cell. We also installed two dispensers inside the steel chamber that are currently not in use.

8. **Side Viewport Replacement:** The six side Kurt J Lesker 1.33" viewports were replaced with MPF viewports, which provide significantly lower laser beam aberrations.

Re-entrant windows (MPF Products Inc. A20460-1) in Figure 2.2 were designed such that when mounted on the chamber, glass windows are 18 mm away from the atom's plane, which is approximately 50 mm closer compared to where the glass was in the old vacuum chamber. This change allowed us to use larger NA objectives to focus traps and image atoms, with maximal numerical aperture we can use with this viewport up to about $NA = 0.65$. With this upgrade, we were able to create arrays of optical dipole traps (tweezers) of waists smaller than 2 μm. Objective we used for all the experiments described in this thesis is Mitutoyo M Plan Apo NIR B 20X 378–867–5 with numerical aperture $NA = 0.4$, as this was the highest NA objective commercially available with the large enough working distance of 25 mm. The bottom re-entrant window has one set of electric field plates mounted on them, and the upper re-entrant window has both the second set of electric field plates mounted as well as the 4-lens cage mount. Details on electric field plates and their connections are given in chapter 3.

The cage lens mount, shown in Figure 2.2, contains four lenses arranged in two pairs. First pair of lenses (Edmund Optics 49-349, $NA = 0.3$) is mounted opposite each other along the y-axis, while

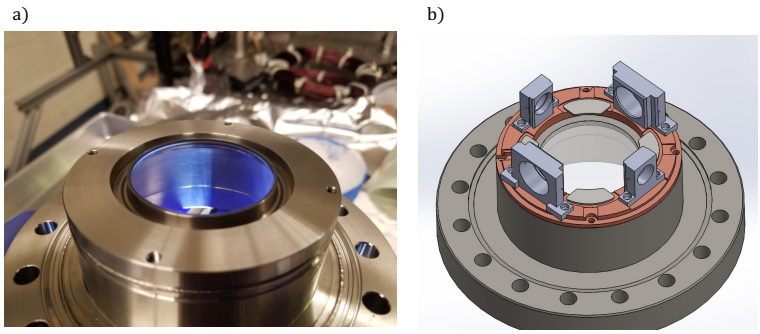


Figure 2.2: Re-entrant viewport and lens cage mount: a. A re-entrant viewport image displaying the viewport with its four screw holes, where the cage mount is attached. **b.** CAD drawing of that re-entrant window showing how it looks like with lens cage mount attached to it. The drawing also illustrates how the electrodes are mounted on the cage by being soldered between the lens mounts. Attached to the top re-entrant window is the cage mount featuring all four lenses and the four electrodes, while the bottom re-entrant window holds only additional four electrode plates.

the other pair of lenses (Edmund Optics 49-787, $NA = 0.2$) are mounted opposite each other along the x-axis. All in-vacuum lenses used are achromats, intentionally chosen for their ability to produce significantly lower levels of aberrations compared to single aspheric lenses. Our $NA = 0.2$ lenses have very low aberrations and are utilized for focusing side trap, side sheets, and side control light for Rydberg excitation and detection experiments. On the other hand, our $NA = 0.3$ lenses have higher amount aberrations, which can sometimes result in star-like patterns and irregularly shaped traps, particularly when used for imaging high optical density (OD) ensembles, as described in section 2.6. With that being said, this is acceptable for our purposes, since these $NA = 0.3$ lenses are not used for beam focusing but solely for diagnostic imaging and not for scientific experimental data. One thing to note about these cage lenses, that we noticed only when assembling the vacuum chamber, is that when we center light on side viewports, then light is not perfectly centered on the lenses. When light along this direction is centered on the lenses, the light will then be slightly off-centered on the side viewports. We believe that this misalignment is due to lower tolerance level in the machining of the old vacuum chamber, but this issue didn't prevent us from aligning these beams properly.

The glass cell and differential pumping stage can be seen in Figure 2.1 and these have not been in

use for any of the experiments in this thesis. The original plan was to use this cell to create a magneto-optical trap (MOT) that would then be transferred to the main chamber, as we were uncertain at the time whether we can create a stable MOT in the main chamber using MOT construction design as described in section 2.4. The differential pumping stage, looks like a straw and it is 12 cm long with 6 mm diameter. It is mounted on $1.33''$ diameter flange of the main chamber on one side and a glass cell on the other side. From conductance calculations, we estimate that the pressure in the glass cell is approximately $70\times$ higher than in the main chamber. Although this upgrade was not used for any of the experiments in this thesis, having the system with two separate regions where atoms can be independently manipulated with light and magnetic fields – glass cell and the main chamber, is a necessary setup to have that can allow for continuous loading experiments[33,34,35]. By incorporating these components, we have prepared the system for future experiments that require continuous atom loading, thereby enhancing the versatility and capability of our experimental apparatus.

The bellow holding the ampule (Sigma Aldrich 276332-1G) containing the Rb source can be seen in Figure 2.1. Initially, after baking the chamber and a couple of weeks later when we connected the coils and set up the optical paths to create a MOT, we were unable to detect the MOT despite setting all parameters correctly. We then heated the bellow to 60° C as Vladan's suspicion was that ^{87}Rb is still coating the walls of the chamber and that is why we cannot see MOT in the main chamber, and heating the ampule can help in coating the walls faster. He was totally right. This bake lasted for a day, and after that we never heated the bellow again. In addition to the ampule, we also have two Rubidium dispensers (SAES Getters, RB/NF/4.8/17 FT 10+10) in the main chamber that we degassed during the bake. We confirmed that they work, initial MOT we got in February 22 2021 was done with dispensers, but since then we didn't use them much as we had sufficient rubidium source just from the ampule alone. The dispensers are still connected to the chamber and the feedthroughs connecting to them are labeled.

The decision to replace the six side $1.33''$ Kurt J Lesker viewports was motivated by Zak's observa-

tions[38]. He compared beams transmitted through the Kurt J Lesker viewports with those transmitted through the MPF viewports and found that the MPF viewports exhibited significantly lower aberrations. Our tests confirmed these findings, and as a result, the current side viewports in the setup are MPF Q24175.

For assembling the vacuum chamber, cleaning vacuum components, and the pumping procedure, we followed the standard protocols as described in the bible reference[39] and Thibault's thesis[37]. We incorporated a few modifications not described in these references and in the thesis so far. Compared to Thibault's thesis, we used vacuum compatible Kapton tape to tape down the wires connecting the electrodes to the chamber's feedthroughs to ensure that these wires are not blocking the optical access to atoms. In addition, given our choice of achromatic in-vacuum lenses, the glue on these lenses limited the maximum baking temperature to about 120° C.

2.3 Laser trapping

Interactions between atoms and light affect the internal degrees of freedom of atoms by changing their electronic states. Since photons carry both energy and momentum, these interactions can influence the motional states of the atoms as well. This principle is used daily in cold atom experiment labs, where lasers of various wavelengths and beam shapes are used to create either dissipative or conservative forces on the atoms[40]. Dissipative forces are used to cool atoms to low temperatures, while conservative forces are used to trap atoms in specific positions. In this section, I will focus on the conservative forces, specifically optical dipole traps also known as optical tweezers. These traps leverage the dipole interaction to confine atoms in potential wells created by the intensity gradients of laser light. The next section will address dissipative forces, specifically laser cooling techniques, without which atoms would not have low enough energy to be trapped inside of these optical dipole traps.

Optical dipole traps use highly focused laser beam to trap and move atoms in space. Laser beams

generating dipole traps have wavelength that is far detuned from the main atomic absorption lines resonance – D1 and D2 transition, transitions to the first and second excited states respectively. When atoms are illuminated with light of large detuning, they behave in light field similarly to how electric dipoles behave in electric field. If we consider the atom as a polarizable classical dipole d in a polarizing electric field E, its energy is $-E \cdot d$. Applied fields with frequencies below the resonance will induce a dipole which oscillates in phase with the field, yielding a decrease in energy. Excitation above resonance induces a dipole which is π out of phase with the applied field, yielding an increase in energy. Consequently, atoms in red-detuned laser fields will seek the field maximum where energy is lowered, while atoms in blue-detuned fields will seek the field minimum where energy is increased[40]. This "seeking" of field maximum or field minimum is how atoms get trapped with laser light, and the sign of detuning defines whether atoms will be trapped by light, red-detuned beams, or antitraped by light, blue-detuned beams. In this experiment we used both types of laser beams - commonly used red-detuned beams to trap atoms as will be explained in this section, but also the less commonly used - blue-detuned beams, that we applied to squeeze atoms inside the red-detuned trap as will be explained in more detail in section 2.6.

Apart from qualitative description of optical dipole traps as given above, these are also very well understood quantitatively. The trap potential that these beams create is given by the following formula[12]:

$$U_{dip} = \frac{3\pi c^2}{2\omega_0^3}\frac{\Gamma}{\Delta}I(r) \tag{2.1}$$

where c is the speed of light, ω_0 is the resonant atomic transition frequency, Γ is the transition linewidth, Δ is the laser detuning from the atomic resonance and $I(r)$ is the intensity of the beam. The trapping force can be derived from this potential as its spatial gradient, which in turn depends on the spatial gradient of the light intensity. This means that if we have chosen the wavelength of the laser we

want to trap atoms with, stronger trapping forces will be achieved by using more tightly focused beams with higher light intensity gradients. For all the experiments described in this thesis, Gaussian beams were used to generate optical dipole traps. In these beams, atoms behave like harmonic oscillators and oscillate around the beam center. The radial and longitudinal trapping frequencies for a Gaussian beam trap have the following dependencies on trap waist and power:

$$\omega_r \propto \sqrt{\frac{P}{\Delta}\frac{1}{w_b^2}} \quad \text{and} \quad \omega_z \propto \sqrt{\frac{P}{\Delta}\frac{1}{w_b^3}} \tag{2.2}$$

where P is the laser power, Δ is the laser detuning and ω_b is the beam's waist.

By measuring the trap depth and trapping frequencies, one can fully characterize the quality of the trap in the experiment. Typical measurements for our experiment are shown in Figure 2.3. To measure the trap depth for atomic ensembles, we use absorption imaging (described in section 2.5) with a typical duration of 10 μs. We first measure the resonance position of the imaging light when the trap is on during the 10 μs imaging segment and then compare it to the resonance position when the trap light is off. To measure the trapping frequency, we use a standard parametric heating technique[41], where by modulating the trap depth sinusoidally at specific frequencies, atoms can get heated out of the trap. These modulation frequencies are twice the trap's trapping frequency. In our experiment, we perform several hundred milliseconds of oscillations to measure these frequencies.

The traps for the measurements in Figure 2.3 are created using an 808nm laser, with laser diode Thorlabs VHG LD808-SEV500 amplified by Toptica BoosTA Pro. To generate multiple traps, we place either a spatial light modulator (SLM, Hamamatsu x13138-02) or an acousto-optic deflector (AOD, AA Opto-Electronics DTSXY-400-800) at the Fourier plane in the laser path in a 4-f configuration, as described in[42]. The primary difference between these two tools lies in their capabilities: while AODs can only generate rectangular array patterns, SLMs can create arbitrary array patterns, as depicted in Figure 2.4. Additionally, SLMs can correct for any beam aberrations by adjusting the

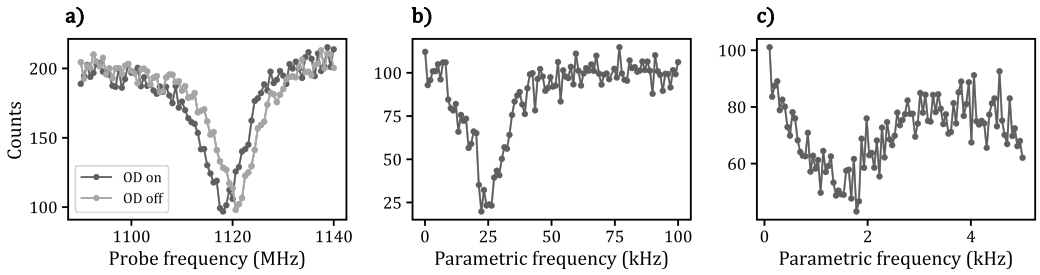


Figure 2.3: Trap characterization measurements: Trap depth and trapping frequency measurements for the approximately $2\,\mu$m traps initially used in the Rydberg detector project. **a.** Light shift measurements reveal trap depth of about 2.5 MHz. **b. c.** Radial and longitudinal resonances respectively measured in parametric heating experiment. The loss feature is observed at roughly twice the trapping frequency, from which we extract radial trapping frequency of $\omega_r = 2\pi\,13$ kHz and longitudinal trapping frequency of $\omega_l = 2\pi\,1$ kHz.

phase pattern of the reflected beam at the Fourier plane which AODs cannot do. However, this arbitrary control comes at a cost: changing the SLM pattern is relatively slow, with switching times greater than 1 ms. In contrast, AODs have a much faster switching time of around $10\,\mu$s, which is highly advantageous in single-atom experiments for initial arrangement of atoms on arbitrary trap grids [19,18] and for mid-circuit reconfiguration of atoms [31]. In our detection experiment, we utilized this feature to both squeeze atoms, as described in section 2.6, and control which ensembles were illuminated by the laser beam at different parts of the sequence, as detailed in chapter 7.

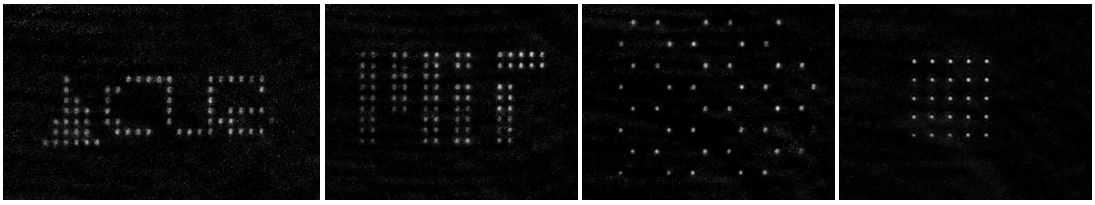


Figure 2.4: Example of arbitrary beam patterns generated using an SLM: The data show absorption imaging measurements where atomic ensembles are loaded into arbitrary beam potentials created by the SLM. This capability is unique to the SLM; in contrast, AODs would only be able to generate the last pattern.

Here, I will note some issues we encountered during the first installation of the SLM in our experiment. Initially, we chose the beam size such that the beam waist matched half of the SLM's shorter window size, a common practice in the field. With this configuration we couldn't get the trapping fre-

quency ratios to approximately match the expected beam waist after the microscope, no matter how much correction we did with our SLM. More specifically, our ensemble size in the longitudinal direction was too long, so much so that we couldn't proceed with this problem and we had to investigate the issue. We found that when we clip the beam waist, Rayleigh range gets much longer, where it is even few times bigger than the Rayleigh range expected for the new clipped waist and it is dependent on the amount of clipping. This means that when we match the beam waist to the half of the SLM's shorter window size, we would clip the beam on the SLM, which would result in a larger Rayleigh range than expected, creating smaller curvature in the longitudinal direction, which would cause smaller longitudinal trapping frequencies and longer ensembles. By reducing the beam size to limit clipping on the SLM, we were able to measure the correct Rayleigh range at the intermediate plane before the chamber. Consequently, the observed trapping frequency ratios approximately matched the expected beam waist after the microscope and our ensembles were looking shorter in longitudinal direction.

2.4 Laser cooling

Outside of scientists circles, lasers are typically associated with burning things, like lasers used for LASIK surgery, laser hair and tattoo removals. However, in cold atom experiments field, lasers are actually used to cool atoms down, and they can do that very efficiently, cooling atoms down to nano-Kelvin low temperatures!

The simplified picture of how the most simple cooling technique, Doppler laser cooling, works is presented in Figure 2.5 and it relies on the Doppler effect and the fact that photons carry energy and momentum. For this laser cooling to work, atom needs to move opposite to photon's direction, so that photon's momentum kick will slow atom down, and in that way reduce atom's kinetic energy. In this case, in atom's frame of reference, photon's energy will be blue-shifted i.e. the atom will "think" photon approaching it has higher energy than what it really has. Since atoms have a finite bandwidth

of laser frequencies they can absorb, efficient laser cooling requires the laser light to be slightly red-shifted, for optimal laser absorption accounting for the Doppler effect.

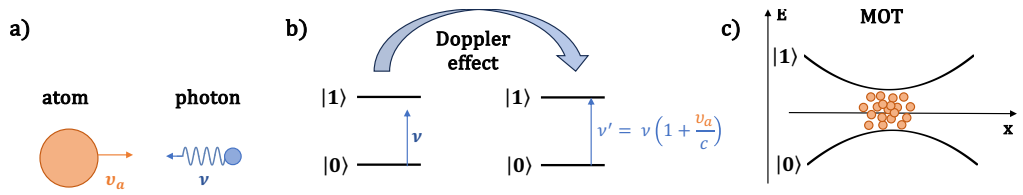


Figure 2.5: Sketch of necessary ingredients for laser cooling of atoms using magneto-optical-trap: a. A photon with frequency ν moving in the opposite direction to an atom with velocity v_a will slow the atom down via a momentum kick. **b.** Because of the finite absorption linewidth of atoms and the Doppler effect, laser light must be slightly red-shifted to be efficiently absorbed by the atoms. **c.** Sketch showing how magnetic field gradient bends the internal energy level structure of atom such that laser beam of fixed ν can continue to cool slower and slower atoms. This gradient also traps atoms in space.

To achieve laser cooling in all directions, the most common laser configuration involves three orthogonal, retro-reflected laser beams illuminating the atoms inside the vacuum chamber. This ensures that for any direction an atom moves, there is a photon moving in the opposite direction to it. The Doppler effect ensures that atoms preferentially absorb light moving opposite to their motion, as this light is shifted closer to atomic resonance, while light moving in the same direction is shifted away from resonance, preventing atoms from absorbing photons that would increase their energy. To adjust for the atoms slowing down as we cool them and thus Doppler effect getting smaller, which would affect how efficiently atoms can absorb light, internal atomic states are changed using gradient coils, such that at the center of the vacuum chamber slowest atoms will be on resonance with laser light and will be cooled there, whereas hotter atoms will be more efficiently cooled a bit further away from the center. This combination of gradient coils and laser light also creates a trapping area for atoms. Constructing such configuration in setup constitutes the essential component of every cold-atom lab, and this is called the magneto-optical-trap (MOT).

In our experiment, we have an unconventional MOT configuration. Instead of the standard three orthogonal retro-reflected beams, we use three retro-reflected beams where two in-plane beams are or-

thogonal and the out-of-plane beam is at 37° angle relative to the vertical. The reason why we have this MOT configuration is the limited optical access we have to the vacuum chamber and the fact that our microscope objective (Mitutoyo M Plan Apo NIR B 20X 378–867–5) that is used to create small traps is covering majority of our re-entrant window and has back focal plane inside of the objective, meaning it is difficult to generate collimated light though this objective. As such, our MOT beams along the vertical direction are sent around the microscope objective to the chamber using top MOT construction as shown in Figure 2.6. The idea behind this construction is to send a perfectly vertical beam from outside the chamber to the construction, which then adjusts the light inside the chamber to the required angle. The light is captured by the same construction at the bottom re-entrant window, making the beam vertical again for retro-reflection. This construction was 3D printed and made out of stainless-steel material. Four dichroic filters (Edmund Optics 69-218) were glued onto the construction using UV-cured glue. The choice of dichroic filters over regular mirrors was due to them being much thinner, and as such, would be able to allow the adequate angles to be achieved with this construction. The construction was then secured to the main chamber using five-minute epoxy, with the epoxy applied to the sides of the construction.

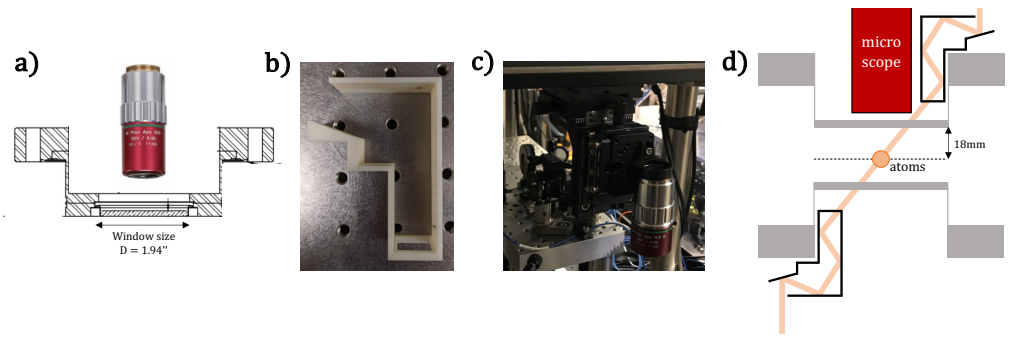


Figure 2.6: Details of top MOT construction: a. Representation of the vertical re-entrant window with depiction of where our microscope objective is relative to it. **b.** 3D printed model of MOT construction, printed out of plastic. In the main chamber, MOT construction is printed out of stainless steel to have stronger support. **c.** Representation of how microscope objective is mounted in our experiment: we use two $1''$ translational stages to adjust the $x-y$ position of the microscope and one 5-axis stage to adjust the z direction and the angle of the microscope. **d.** Depiction of top MOT beam path. Light is sent from the top around the microscope objective and retro-reflected at the bottom.

In addition, apart from unconventional MOT configuration, we also use different parameters to generate the MOT compared to most groups. For the in-plane MOT beams, we use fairly standard, large beams of 25 mm diameter, but for the top MOT construction, we use the largest beam we could possibly send along that direction, which is around 6 mm in diameter - much smaller than the typical $15 - 25$ mm used in cold atom labs. We use approximately 35 mW of power in the 2D direction per beam and around 5 mW in the top MOT direction. This power level is significantly higher than the typical $10 - 20$ mW total power used for all MOT beams in other experiments, but we opted for these higher powers because we wanted to load a large number of atoms into the small volume defined by our top MOT beam. Additionally, to stabilize our MOT against daily humidity and temperature changes in the lab, we use a higher gradient for the gradient coil in the steady-state MOT, specifically 14 G/cm^2, compared to the typical $\sim$10 G/cm^2. With these adjustments, our MOT remains very stable even with humidity changes of 30 % and temperature changes of a few degrees. In extreme cases like this, the MOT may shift slightly, but we can still load a similar number of atoms into our traps.

The Doppler cooling method described thus far has a fundamental temperature limit to which it can cool atoms down to, known as the Doppler temperature. On one hand, cooling happens as higher-energy photons are emitted compared to the ones that are absorbed, but the emission process itself, where atoms scatter a photon in random directions is also causing atoms to heat up, as with release of photon in random direction, atom will get a momentum-kick in the opposite direction that will heat the atom, meaning that there will exist a steady state down to which atoms can be cooled with this method. This steady-state temperature, Doppler temperature, is 146 μK for ^{87}Rb atoms[43]. This atomic temperature would have been too high to make experiments in this thesis work, so we had to develop more cooling techniques. In this experiment we used following cooling methods successfully: polarization-gradient cooling[13], non-degenerate Raman sideband cooling[44], Lambda-gray molasses cooling[45] and D2 EIT cooling[46]. We also tried to make degenerate Raman sideband[47] cooling work,

however, we were unable to do this for ensembles. Most likely cause of this was the too-high atomic densities of our ensembles, which is why we switched to doing non-degenerate Raman sideband cooling on a D1 line as discovered was more suitable for these scenarios in different Vladan's subgroup[44].

In our experiment, polarization gradient cooling is implemented using the same beams as the MOT beams, where this initially surprising cooling effect is explained in[13]. It was done in so called compressed MOT stage, where MOT is compressed by ramping up the gradient coils to nearly twice the steady-state level. Optimal parameters, discovered through machine learning, achieved temperatures around $40\,\mu$K and even led to the formation of a Bose-Einstein Condensate (BEC). Detailed methods and parameters are discussed in chapter 6 and its appendix. This cooling technique was applied to all ensemble experiments and a modified version was used for single atom experiment in chapter 8.

Raman sideband cooling was implemented in our experiment in both degenerate[47] and non-degenerate setting[44] with the aim to cool micro-ensembles for the chapter 7 project. As mentioned, only the non-degenerate case worked for our ensembles, but in the end, we ended up not using it to obtain the final signal of our chapter 7 project. This is because despite managing to achieve lower temperature ensembles, that came at the cost of reduced atom number. The decrease in atom number had a more negative impact on our final signal than the improvement gained from the lower temperature. As a result, we decided not to use this cooling technique in the final measurement.

The lambda-gray molasses cooling technique was explored during the transition between projects involving ensemble arrays in chapter 7 and single atom arrays in chapter 8. We wanted to improve single-atom loading efficiency using this established method[45] and we even optimized the sequence with our machine learning package[48]. Although we achieved around 80% average single atom loading efficiency for the array of traps, compared to standard loading of around 50% without this technique, we did not adopt this technique for the experiments in chapter 8 due to its significant increase in cycle time which we found to be an unnecessary cost to pay at that point in time.

Finally, the D2 EIT cooling technique[46] was crucial for the experiment described in chapter 8. Details of this technique are described in chapter 4.

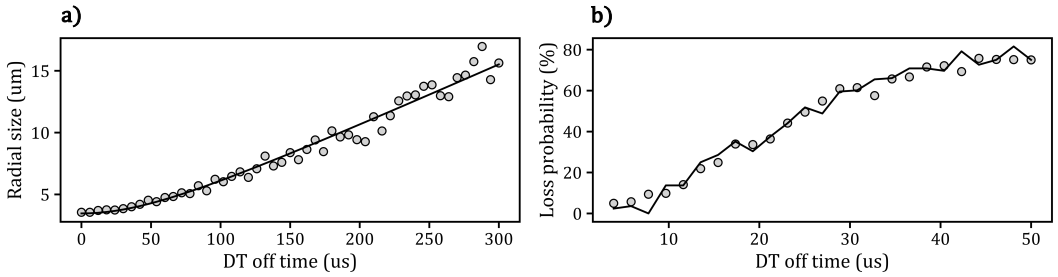


Figure 2.7: Temperature Characterization Measurements: a. Temperature measurement of atomic ensemble using the time-of-flight technique. The data presented shows the temperature measurement in the radial direction of the trap, with a fit revealing a temperature of approximately $26\,\mu$K. A similar temperature is obtained when fitting the longitudinal size of the ensemble. **b.** Temperature measurement of a single atom using release-and-recapture technique. This measurement can only measure the radial temperature of single atoms inside the trap. A Monte Carlo simulation, which provides the fit in this figure, reveals a temperature of approximately $50\,\mu$K.

To measure temperature of trapped ensemble atoms we do a time-of-flight (TOF) measurement[49]. In this measurement we release the atoms from the trap just before a short, typically $10\,\mu$s long, absorption imaging, varying the time between release and imaging. By fitting the size of the ensemble at different points in time, we measure how quickly the atoms expand from the released trap, and from there we can deduce the atomic temperature inside of trap. For experiments in chapter 6 and chapter 7, typical TOF measurements revealed around $30-40\,\mu$K temperatures for trap waists in the range $2-5\,\mu$m and trap depth of about 2.5 MHz. In contrast, to measure the temperature of single atoms in the trap, we use the release and recapture technique[50]. This involves releasing the atom from the trap for a varied period of time and measuring the likelihood of its recapture. Monte Carlo simulation, simulating the likelihood of recapture based on trap parameters such as trap waist and trapping frequencies, reveals the single atom temperature. Typical data for each technique is shown in Figure 2.7.

2.5 Imaging

During my PhD, I had the pleasure of exploring various imaging methods for different purposes. A significant part of my thesis work involved developing novel imaging techniques, such as fast non-destructive imaging and high magnetic field imaging. In this section, I will not present these new methods, which was done in Chapters 5, 7 and 8, but instead I will focus on the most commonly used imaging techniques in our field, absorption and fluorescence imaging, which we used daily in our lab.

In simple words the difference between absorption and fluorescence imaging is that in absorption, the observed signal is the absence of light and in fluorescence, the observed signal is the presence of light. Absorption imaging involves directing an image light into the camera, such that an ensemble of atoms that we want to image is positioned in between the imaging light and the camera. The atoms will absorb that light and scatter it in all directions, resulting in camera detecting reduced light intensity compared to the case when the atoms are absent. In contrast, for fluorescence imaging, light is not directed into the camera. Atoms absorb this light and scatter it in all directions, with the camera capturing a small portion of this scattered light. Thus, in fluorescence imaging, the camera measures the presence of light emitted from the atoms. This is illustrated in Figure 2.8.

From this intuitive picture, one could come to a wrong conclusion that absorption imaging would be better in detecting atoms compared to fluorescence imaging. However the opposite is true[51], fluorescence imaging shows better signal-to-noise-ratio (SNR) compared to absorption imaging. Large part for this is that, in fluorescence imaging, since signal appears only when the absorber is there, the background is very clean. In contrast, for the absorption imaging, the background can have interference fringes creating "fake" absorption lines as shown Figure 2.8, and thus for absorption imaging one needs to take an image with atoms followed by the image with no atoms and divide the two to get rid of interference fringes and achieve a better SNR. It is also common to use principal component analysis (PCA) methods to additionally correct for fringes changing in time between the two images[38].

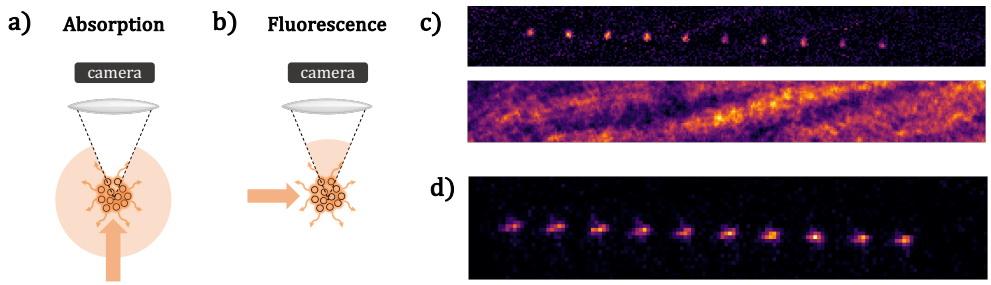


Figure 2.8: Illustration of the difference between absorption and fluorescence imaging: a. In absorption imaging probe light is directed towards the camera, indicated by the orange arrow. The shaded region represents the fraction of scattered light that does not reach the camera created by absorption of incident beam, leaving only small fraction of incident light to be transmitted and small fraction of scattered light from atoms to be detected. **b.** In fluorescence imaging probe light is directed away from the camera. The shaded region indicates the fraction of scattered light, collected by a lens, that reaches the camera and generates the signal in fluorescence imaging. **c.** Data showing the influence of interference fringes on the absorption imaging. The upper image is absorption imaging data referenced to a no-atom image, while the lower image is not. This example shows how strong interference fringes affect the quality of the absorption imaging. **d.** Fluorescence image of single atoms showing no fringing effects without taking reference image, illustrating a better signal-to-noise ratio compared to absorption imaging.

In experiments described in this thesis we used absorption imaging to detect ensembles, and fluorescence imaging to detect single atoms. Our typical absorption imaging was $10 - 50\,\mu$s long, on-resonance with atoms and we would typically send $I \leq 0.1\, I_{\text{sat}}$ of imaging laser intensity. This low amount of intensity was limited by EIT measurements, specifically self-blockade as described in chapter 5 and its appendix. In contrast, fluorescence imaging of single atoms was much longer, typically $30 - 60$ ms long, about 50 MHz red-detuned from the bare resonance (not taking into account the trap light shift) and we would typically send 3 retro-reflected beams of $0.5 - 1$ mm waist with intensity $I \sim I_{\text{sat}}$ in each. When we did fluorescence imaging of ensembles instead, we did manage to do it on resonance and in much shorter time with much lower laser intensity. At some point we tried to do Rydberg EIT in fluorescence imaging on ensembles for Rydberg detection project in chapter 7, with the goal of improving detection SNR by doing fluorescence imaging. In this case, we used low intensity imaging light, that was on resonance during fluorescence. Despite being able to observe Rydberg EIT in fluorescence imaging, our fluorescence detection suffered from atom loss more than the

absorption measurement did, and we didn't end up using this technique for that reason in the end.

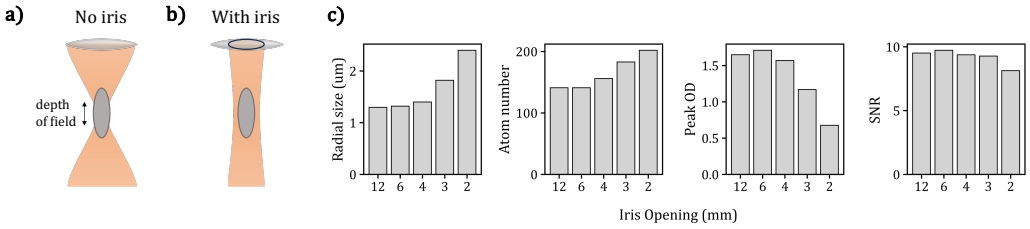


Figure 2.9: Illustration of the iris effect and corresponding experimental results: a. Demonstrates how light from ensembles is collected by the full aperture of the lens, resulting in a small depth of field and atoms falling out of the field. **b.** In contrast, by limiting the lens size, the Rayleigh range of the collected light can be extended, allowing efficient collection from longer ensembles. **c.** Shows experimental results after adding an iris to the setup. While with clipping we were able to observe larger ensembles in radial direction (because of lower resolution) and fit more atoms, the peak optical density (OD) decreased, leading to a slight reduction in the signal-to-noise ratio (SNR). Thus, the addition of the iris did not improve the imaging SNR.

I will note here one interesting imaging problem we had, and solution we tried to find. Despite the solution ultimately not helping, I believe this attempt is worth mentioning. This problem was related to us trying to improve our imaging SNR for the project in chapter 7. We were at the time using $2\,\mu$m waist traps with our atomic cloud sizes being approximately $\sigma_x = \sigma_y = 0.7\,\mu$m and $\sigma_z = 8\mu$m. We observed a consistent issue where the estimated number of atoms was $2-3$ times lower when imaging along the vertical direction compared to the horizontal direction. This discrepancy was problematic because vertical imaging was our preferred direction, as we could generate and detect 2D arrays of atoms in this direction only. We realized that this issue was due to the large longitudinal size of our atomic clouds, causing a significant portion of ensemble to fall outside the microscope's depth of field as depicted in Figure 2.9, unlike in horizontal imaging. To circumvent this, we tried to add iris in the Fourier plane right before the camera, as we wanted to make our microscope objective of effectively lower NA, and extend the depth of field with clipping such that we allow light from the edges of the cloud to hit the camera more efficiently. Our findings are given in Figure 2.9. Main takeaway is that with clipping we were able to fit larger number of atoms, but ultimately because the peak OD

decreased our effective SNR didn't increase and it even decreased.

2.6 Micro-ensemble generation by blue-detuned squeezing

As explained in section 2.3, when atoms are trapped using optical tweezers, they are confined due to the intensity curvature of the trapping light along both the radial and longitudinal directions. For Gaussian-shaped beams, which are the only beams we used in this thesis, the trapping in the longitudinal direction is weaker compared to the radial direction by a factor of $\sqrt{2}\frac{\omega_b \pi}{\lambda}$, where ω_b is the trapping beam waist and λ is the trapping beam wavelength. This means that the ensemble size in the longitudinal direction will be larger than in the radial direction by the same factor. For a typical red-detuned trap for ^{87}Rb with a very small trap waist of $2\,\mu$m, this factor is approximately 11.

For Rydberg detector experiment in chapter 7, the optimal micro-ensemble is a $r_{\text{rms}} \sim 3 - 4\,\mu$m round ensemble, which cannot be generated using only one Gaussian optical tweezer. To create such round ensembles, we use the trap configuration presented in Figure 2.10. Initially, atoms are loaded into red-detuned $\lambda = 808$ nm tweezers generated by the spatial light modulator (SLM). We then use two sheets of blue-detuned 770 nm traps to dynamically compress the atoms into smaller volumes.

Experimental details are the following. We first trap atoms from compressed MOT cloud using red-detuned 808nm traps of $5\,\mu$m waist, with which we get ensembles of size $\sigma_x = \sigma_y \sim 2\,\mu$m and $\sigma_z = 32\,\mu$m. To compress atoms along the longitudinal direction we use two sheets of blue-detuned 770nm beams of waist $4\,\mu$m $x32$ μm. Two sheets are generated using one-dimensional AOD (AA Opto-Electronics DTSX-400-800.850) and focused on the ensembles by in-vacuum lenses of numerical aperture $NA = 0.2$. Longitudinal size of the ensemble is dynamically compressed with these sheets by chirping the RF tones sent to the AOD, which is consequently changing the distance between these blue-detuned beams.

I'll note here the alignment procedure of the blue-detuned beams, as these beams do not trap

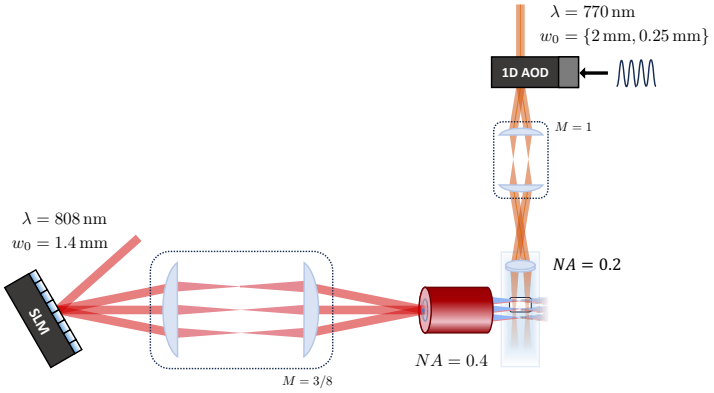


Figure 2.10: Schematic of a beam configuration setup used to generate round micro-ensembles: Ensembles are initially loaded inside of red-detuned 808 nm traps of waist $5\,\mu$m, and they are longitudinally squeezed using two sheets of blue-detuned 770 nm beams of waists 4μm $x32\,\mu$m. Red-detuned traps are generated using SLM, and blue-detuned beams are generated using one-dimensional AOD.

atoms, so we had to come up with a procedure to align them. To get initial alignment, we diffract only one beam using AOD. We first sent 785 nm beam along that direction, that generates red-detuned trap that will trap atoms. By looking at atoms in absorption imaging, we can adjust the position of the traps and we adjust the home-built rotational mount holding the AOD, so that we assure that as we squeeze, beams are only changing vertically and not horizontally. After this step is done, we send 770 nm beam along this path. Given that we have achromatic lenses in this beam's optical path (including the in-vacuum lenses), our beam position with this change of wavelength will change a bit, though not too much, so slight further alignment is necessary. For the next step, we send 785 nm beam from the other side of the chamber and position it where the 770 nm beams should go. We then adjust the alignment of 770 nm beam such that we deplete atoms loaded in 785 nm traps as good as we possibly can. To finalize the alignment, we diffract two beams and adjust the alignment that allows for the best squeezing of the 808 nm SLM traps.

Experimental results of squeezing are given in Figure 2.11 and they show how the atom number inside the ensemble, as well as longitudinal and radial sizes fitted from side absorption imaging are

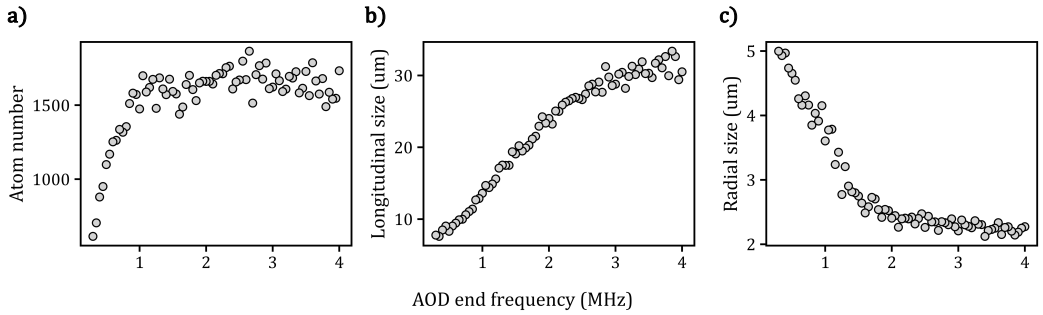


Figure 2.11: Experimental results showing the effects of squeezing: Initially, traps are loaded inside a red-detuned 808 nm trap, and they are longitudinally squeezed using two sheets of blue-detuned 770 nm beams. The red-detuned traps are generated using an SLM, and the blue-detuned beams are generated using a one-dimensional AOD. **a.** Atom number as a function of the end squeezing frequency. **b.** Longitudinal size (the size being squeezed) as a function of the end squeezing frequency, showing that squeezing does indeed work. **c.** Radial size as a function of the end squeezing frequency. The observed change in radial size is not real and it is an imaging effect that occurs at very high-density small ensembles, as explained in the main text.

changing as a function of end separation between two sheets, i.e. frequency difference between them. For all the measurements squeezing lasted 80 ms, chirping was done using DDS, where the number of steps for the frequency chirping was also set to pre-optimized number of 80. We can see that atom number starts to decrease when sheet frequency separation is approximately 1 MHz corresponding to 30 μm separation. This is quite fascinating given that starting ensemble waist is 32 μm, meaning that we can compress ensemble by factor of two with this squeezing without loosing any atoms! For smaller separations, we start to see atom loss as we squeeze, and interestingly, in radial direction, we start to see an increase in size. To test if this observation is real, we repeat this squeezing measurement but we use top absorption imaging instead, along the SLM beam direction, and in this case we don't observe any radial expansion in that direction. We attribute this "increase in size" to the large aberrations of the in-vacuum lenses of numerical aperture $NA = 0.3$, supported by weird star-shaped size of the ensemble present whenever ensemble density is very high. Because of this effect we also cannot fully trust the final longitudinal size of the ensemble in Figure 2.11b. However, for all of our detection measurement, final separation between sheets was 15 μm, with 770 nm beam waist in longitudinal

direction of $4\,\mu$m, meaning that atoms are then confined in the region $15 - 2 \times 4 = 7\,\mu$m, making longitudinal ensemble size $\sim 3 - 4\,\mu$m.

3

Theory and Experimental techniques for Rydberg atoms

3.1 Theory

As described in chapter 2, systems of cold neutral atoms have become one of the key platforms for studying quantum phenomena. To study complex quantum systems, atoms need to interact, typi-

cally with each other. Neutral atoms, by nature, do not interact strongly with each other. However, they can be made to interact strongly when positioned very close to each other, as seen in Bose-Einstein Condensate experiments. This approach has led to remarkable experiments, which explore quantum phase transitions and entanglement in optical lattices[2,3,4]. These experiments, though groundbreaking, come at the cost of high experimental complexity, requiring sophisticated cooling techniques and advanced technical developments to observe atoms in close proximity.

Alternatively, neutral atoms can be made to interact very strongly with each other, in a technically simpler way, by exciting these atoms into higher n energy levels, commonly known as Rydberg levels or Rydberg states. When atoms are excited to these states, they behave like small electric dipoles, allowing two atoms in these excited states to interact very strongly with each other. For example, one can achieve interaction strengths of several tens of MHz at distances of several tens of micrometers, and GHz interactions are possible at closer distances. The advantage of this approach lies in its technical simplicity. Positioning atoms at distances ranging from several tens of micrometers down to a few micrometers can be readily achieved with diffraction-limited optics, as described in section 2.3. Additionally, this method allows for on-demand, controllable interactions that can be turned on and off as needed during the experimental sequence. In the experiments described in this thesis, we used this approach to get atoms to interact with each other. The properties and behaviors of Rydberg atoms are well understood[52,53] and here I will provide the most important information needed to understand the experiments in this thesis.

A Rydberg atom is an atom in which one of its valence electrons is excited to a very high principal quantum number n, ranging from ten to even hundreds. The properties of these atoms scale with this principal quantum number n. The binding energy of these Rydberg atoms is given by the formula:

$$E_{\mathrm{nlj}} = -\frac{R\mathrm{y}}{(n-\delta_{\mathrm{nlj}})^2} \tag{3.1}$$

where Ry is the Rydberg constant, n, l, and j are the principal, angular momentum, and total angular momentum quantum numbers respectively, and δ_{nlj} is the quantum defect. These quantum defects are well known for the atoms used in this thesis and we generally used this formula within the software packages provided by Šibalić [52] and Weber [53] to find the wavelengths at which we should tune our lasers to observe transitions from the ground state to Rydberg states.

Atoms excited to Rydberg states can exhibit strong interactions due to their large dipole matrix elements, which arise from their significant size. The average size of a Rydberg atom is given by $\langle r \rangle = n^2 a_0$, where a_0 is the Bohr radius. These large sizes result in enhanced dipole-dipole interactions. Moreover, atoms in Rydberg states can have remarkably long lifetimes, on the order of hundreds of microseconds, compared to the typical lifetime of atoms in the first excited state, which are on the order of several tens of nanoseconds. In fact, the lifetime of a Rydberg state scales as n^3, meaning the higher the principal quantum number n, the longer the electron can remain in that state.

Given these scalings, one might think that working at very high n would be ideal for experiments, but that is not always the case. One reason is that for a fixed laser power, the rate at which you can excite an atom to state n scales as $n^{-\frac{3}{2}}$. In these experiments, the quality of preparation often depends on how quickly transitions can be driven, so lower n values are preferred in this case. Additionally, at high n levels, Rydberg atoms behave almost like ions and become highly sensitive to electric fields, with electric field sensitivity scaling as n^7. This means that, experimentally, at these high n levels, we need to precisely zero the electric fields, which can sometimes be challenging. For example, electric fields at the atom position can easily fluctuate due to proximity to dielectric materials, such as glass windows, which can accumulate charge when exposed to high-power lasers that we typically use in these experiments.

To find optimal Rydberg n level for the experiment, it is important to consider the interaction scaling as well. Two atoms excited to Rydberg states can interact either through resonant dipole-dipole interaction or via Van der Waals interaction. In case of resonant dipole-dipole interaction, interaction

strength at distance R scales as $C_3 \propto \frac{n^4}{R^3}$, and in case of van der Waals interaction as $C_6 \propto \frac{n^{11}}{R^6}$.

Typically, in experiment, one chooses n level taking into account all these scalings, with interaction strength and excitation drive scaling being the most important ones. In the experiments described in this thesis, Rydberg states with n in the range $50 - 100$ were explored.

3.2 Finding Rydberg transitions

Here, I will briefly describe how we find Rydberg transitions in our experiments and the laser configuration we used to do this. To excite a ground state atom to a Rydberg state, we use two-photon excitation scheme. This involves using a 780 nm laser to excite atom from the $5S_{1/2}$ state to the $5P_{3/2}$ state, followed by a 480 nm laser to excite the atom from the $5P_{3/2}$ state to the nS or nD Rydberg state. The 780 nm laser can be tuned using ground state atoms by, for example, finding resonance in absorption imaging. This laser is typically beat-note locked or injection locked with the master laser, 780 nm Moglabs Tunable Cat Eye Laser. We lock this master laser to an Ultra-Low Expansion (ULE) cavity from Stable Laser Systems, with full-width half-maximum (FWHM) linewidth of approximately 40 kHz at this wavelength. The master laser linewidth is estimated to be 10 kHz using the standard technique of determining the standard deviation of the voltage variation of the error signal when the laser is locked, and then applying voltage-to-frequency conversion using the Pound-Drever-Hall (PDH) lock signal [54].

The second laser, the 480 nm laser, determines which Rydberg n level we couple to, as Rydberg levels are typically quite separated, often by many GHz or more, depending on the n level. The 480 nm laser, a Toptica TA-SHG Pro 1W, is derived from a frequency-doubled 960 nm laser. To lock this laser, we send the 960 nm beam to the ULE cavity for PDH locking, achieving an estimated linewidth of 3 kHz. To simultaneously lock the 480 nm laser to the ULE cavity and tune it to the desired atomic transition, we use an electro-optic modulator (EOM). By locking an EOM sideband of the 960 nm

laser to the ULE cavity and tuning the EOM frequency, we can shift the carrier frequency of the 480 nm laser to be on resonance with the atoms.

To find Rydberg transitions we use calculations from Šibalić [52] and tune 480nm laser such that on the 200 MHz resolution wavelength meter, High Finesse WS6-200, we can see that we are in the vicinity of that number. Then we further tune the frequency of the laser with atoms in the experiment by depleting MOT. Once we find that wavelength, we start scanning the laser frequency in $20 - 50$ MHz range, making sure we are still depleting MOT. We then adjust the EOM frequency until we can see that TEM_{00} mode is transmitted through the cavity while atoms are depleted. With that, we roughly have the EOM frequency that we will eventually use in the experiment, but further fine-tuning is needed with atom signal at specific magnetic fields we will work at. For that, for all experiments in this thesis, we used Rydberg laser to excite ensemble atoms in EIT configuration, and then EIT transmission at 780nm resonance is what we would use to further tune the 960nm EOM frequency.

During my PhD, we explored a wide range of Rydberg *n* levels as part of our experiments, particularly those discussed in chapter 7. The states I investigated throughout my PhD include:

$$62S_{1/2} \rightarrow 62P_{1/2},\ 62P_{3/2}$$
$$91S_{1/2} \rightarrow 90P_{3/2},\ 91P_{3/2},\ 91P_{1/2}$$
$$58S_{1/2} \rightarrow 58P_{3/2}$$
$$54D_{3/2} \rightarrow 55P_{1/2},\ 55P_{3/2}$$
$$54D_{5/2} \rightarrow 55P_{3/2}$$
$$74D_{5/2} \rightarrow 75P_{3/2}$$

3.3 Electric field zeroing

As mentioned in the theory part of this chapter, Rydberg atoms have a very high electric field polarizability, which strongly depends on the principal quantum number n. In practice, this means that if there is no control over the electric field in the experiment, one should work with low n, probably lower than 70. But even with electric field control, care must be taken when sending high-power lasers through dielectric viewports. These viewports, being very close to the atoms (about 18 mm), can accumulate electric charge when exposed to high-power lasers, such as a 480 nm laser at hundreds of mW for extended periods. This accumulated charge leads to uncontrolled fluctuations in the electric field. If electric field control is not available, an alternative method was found by the community to remove charges on the viewports by shining UV light on them [55].

Ideally, for Rydberg experiments, the chamber should be designed to include electric field control. In our experiment, this is achieved using eight in-vacuum electric field plates mounted on the re-entrant viewport windows. The schematic of the electric field plate labeling and an image showing how they are connected to the wires connecting them to the vacuum chamber feedthroughs are provided in Figure 3.1.

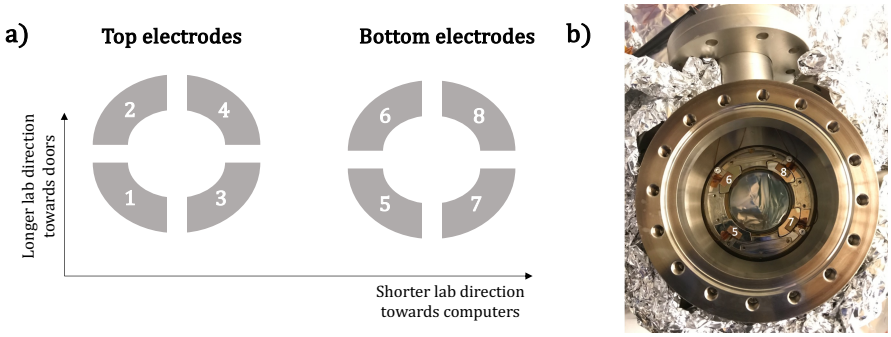


Figure 3.1: In-vacuum Electric Field Plates: a. Schematic of the top and bottom electrodes labeling. **b.** An image of the bottom electrodes taken during the vacuum assembly. Wires were soldered onto the electrodes using vacuum-compatible solder wire and connected to the chamber feedthroughs. During assembly, we confirmed that the electrodes are not connected to the chamber wall, ensuring independent control for each electrode.

Each plate is controlled by an analog output from a National Instruments NI 6733 PCI card. These eight electrodes collectively control the electric fields in three directions according to the following formulas:

$$V_x = V_1 + V_2 + V_5 + V_6 - V_3 - V_4 - V_7 - V_8$$
$$V_y = V_1 + V_3 + V_5 + V_7 - V_2 - V_4 - V_6 - V_8$$
$$V_z = V_5 + V_6 + V_7 + V_8 - V_1 - V_2 - V_3 - V_4$$

To zero the electric fields, we perform Electromagnetically Induced Transparency (EIT) with Rydberg atoms and measure how far off resonance the 480 nm control light is as a function of the field. Typical dependencies observed for nS states are shown in Figure 3.2.

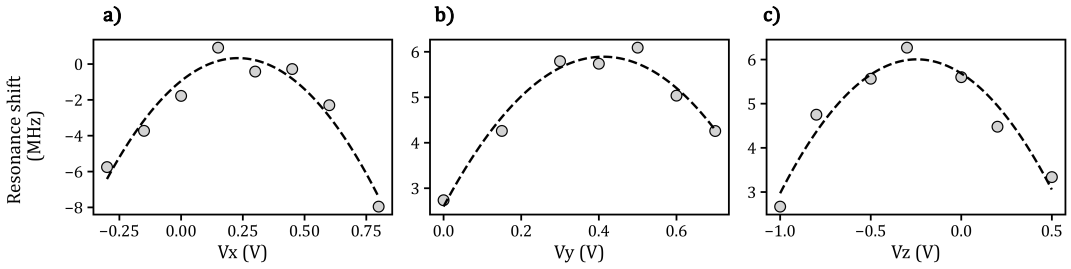


Figure 3.2: Electric Field Zeroing Data: This data was taken by varying the electric field in one direction and observing the consequent resonance shift of the EIT. **a.** Control light resonance shift as a function of V_x. **b.** Control light resonance shift as a function of V_y. **c.** Control light resonance shift as a function of V_z.

Once the electric field is zeroed out, and as long as no high-intensity 480 nm light is sent to the experiment in steady-state for a long time, the electric field remains stable over many months.

3.4 Rydberg state preparation using microwave drive

What has been described so far covers how we find Rydberg transitions using Rydberg EIT and how we zero out the electric field. In this section, I will focus on how we prepare a Rydberg atom and manipulate its state by driving microwave (MW) transitions between different Rydberg levels. Even in our preparation scheme, we use MW drive, so I will first provide details on how we perform MW driving before discussing the preparation scheme.

The microwave drive is applied using a MW antenna, which in our application was just an unterminated SMA cable. Initially, for the experiments described in chapter 5, this antenna was not fixed, which resulted in us needing to do frequent calibration of the MW drive. For the experiments described in chapter 7, we fixed this issue by securing the antenna on a homemade stage, and this ensured long-term stability. To create polarized MW drive, multiple antennas can be used; in chapter 5, this was achieved using two antennas.

To calibrate the MW frequency, one can apply the MW drive while performing Rydberg EIT and extract the MW drive frequency from the MW EIT triple-dip feature. This method was used in chapter 5 to both calibrate the MW Rabi frequency and create polarized MWs. This was done by adjusting the phase of the MW drive between the two antennas to decrease the coupling on transitions driven by unwanted MW polarization. However, for ensembles with lower optical density (OD), i.e., OD smaller than 2, like the ones used in chapter 7, this feature can be challenging to resolve. In this case, we calibrated the MW Rabi by parking on the EIT transmission peak, scanning the MW drive, and observing where the largest absorption signal was found. While this measurement does not provide the most precise measurement of the MW Rabi frequency, it gives a reasonable estimate.

To prepare a Rydberg atom within the ensemble, we use a three-photon process scheme involving a 780 nm beam, a 480 nm beam, and a MW drive and more details can be found in Chapters 5 and 7 and their respective appendices. Most single atom Rydberg experiments utilize a two-photon process

without the MW drive to prepare a Rydberg atom. However, in our experiments, we require the 480 nm beam to be on resonance for the EIT measurement during ensemble readout, which would typically be detuned in the two-photon single atom preparation case. Since this laser is directly locked to the ULE cavity, we cannot easily change its frequency mid-sequence by a large amount. Instead, we blue-detune the 780 nm laser and adjust MW frequency accordingly by the same amount $\delta = 100\,\mathrm{MHz}$ to avoid populating the intermediate states, while keeping 480 nm fixed.

To prepare a single Rydberg atom inside of the ensemble, we choose high Rydberg n level and we tune the preparation linewidth to be small enough to assure single Rydberg is being prepared. For experiments in chapter 7 we prepare Rydberg atom in the state $|75\mathrm{P}_{3/2}, m_J = 3/2\rangle$ with $C_6 = 45\,\mathrm{GHz}\,\mu\mathrm{m}^6$, and we obtain a power-broadened linewidth of $\gamma_{3\mathrm{ph}} \approx 500\,\mathrm{kHz}$, corresponding to a blockade radius of $\left(C_6/\gamma_{3\mathrm{ph}}\right)^{1/6} = 6.7\,\mu\mathrm{m}$, which is sufficient to block the ensemble and ensure only a single Rydberg atom is prepared. Our preparation scheme involves turning on all three beams simultaneously, and we observe saturation of the preparation signal with a characteristic timescale of $\approx 3\,\mu\mathrm{s}$ in the overdamped regime. We do not observe Rabi oscillations consistent with the preparation of a $|W\rangle$ state, in which fast dephasing on the order of a few hundred nanoseconds has been experimentally observed[56]. We attribute our observations to fast dephasing of the collective $|W\rangle$ state, thus preparing a statistical ensemble consisting of a single Rydberg excitation randomly distributed within the cloud with an upper-bounded-fidelity of $N/N+1$, where N is the number of atoms[57].

3.5 Rydberg lifetime and coherence time measurements

Once the Rydberg atom is prepared within the ensemble, it can be addressed using a different MW drive and manipulated between different Rydberg n levels. Some examples of this includes coherence time measurements, and that will be described in this section.

Before checking the coherence time, we first measure the lifetime of an atom in the Rydberg state.

Theoretically, lifetimes are expected to be on the order of hundred microseconds, depending on the n level, with the higher n levels exhibiting longer lifetimes. Our measurement for the $62P_{3/2}$ level, presented in Figure 3.3, reveals a lifetime of approximately $76\,\mu$s. To do this measurement, we first prepare a single Rydberg atom within the ensemble in the desired Rydberg state, which in this case was $62P_{3/2}$. We then wait for an extended period and use our detection method, as described in chapter 5, to verify if the Rydberg atom remains in the desired state.

Coherence time between two Rydberg states is typically shorter than the lifetime of each state, but theoretically, it can be up to twice as long as the lifetime. To measure coherence time, we first prepare a Rydberg atom and then perform a Ramsey measurement. This involves applying two $\frac{\pi}{2}$ MW pulses on resonance with the transition we want to measure, and we vary the time interval between the two pulses. A typical coherence time measurement, as shown in Figure 3.3, revealed approximately $12\,\mu$s coherence time between the $74D_{5/2}$ and $75P_{3/2}$ states.

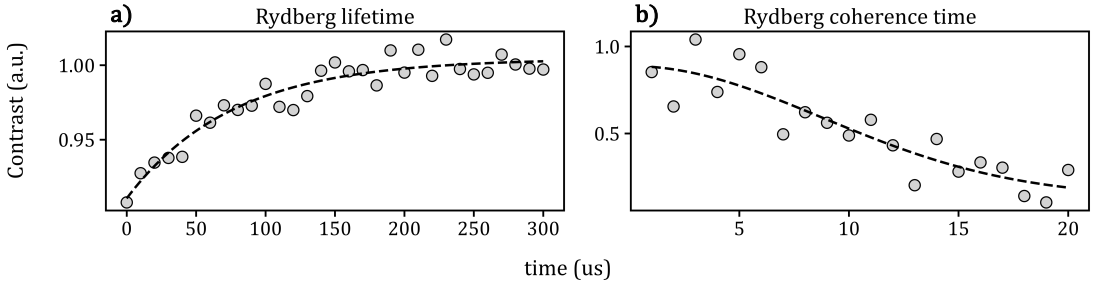


Figure 3.3: Rydberg lifetime and coherence time measurements: Example of Rydberg lifetime and coherence time measurements with Rydberg atoms held inside the dipole trap. **a.** Lifetime measurement for the $62P_{3/2}$ Rydberg state with the fitted lifetime of $76\,\mu$s. **b.** Coherence time measurement for the $74D_{5/2} \rightarrow 75P_{3/2}$ transition with the fitted coherence time of approximately $12\,\mu$s.

Both the coherence time and the lifetime measurements were done with the trap light on, which can influence the results as the Rydberg atom is anti-trapped by the traps used for ground state atoms. Despite this, we managed to obtain reasonably good coherence time and lifetime values, so we did not pursue further improvements.

4

Electromagnetically Induced Transparency

4.1 Introduction

Electromagnetically Induced Transparency (EIT) is a phenomenon where an optical medium, such as an ensemble of ^{87}Rb atoms, becomes transparent to a resonant probe light within a narrow frequency range in the presence of a strong coupling beam. Normally, in absence of the strong coupling beam, the medium would absorb the resonant probe light. Initially, this might seem like a fascinating scien-

tific curiosity, but EIT has numerous practical applications in the field of neutral atoms: from using EIT to slow down and even stop the light, to studying optical non-linearity at a single photon level to using it to cool atoms and ions more efficiently. In this dissertation, we used EIT for majority of these applications. This chapter provides the necessary theoretical background and initial calibration measurements essential for understanding the experiments in Chapters 5, 7, and 8.

I will also note here that, technically speaking, many applications in this work were done in the Autler-Townes regime rather than EIT. These two effects are very similar, and experimentally, they produce similar looking results. On the surface level, the difference lies in the strength of the control field that modifies the absorption line of the probe light: in the Autler-Townes regime, the control light is strong, whereas, in the EIT regime, the control light is weaker, though still stronger than the probe light. Additionally, EIT requires Fano interference, while the Autler-Townes effect comes purely as a consequence of two dressed states, without relying on interference [58,59,60].

4.2 Theory

Theory of EIT has been extensively studied, and it is now even part of the regular curriculum for AMO classes, with my go-to reference being Misha's lecture notes [40]. In addition, Rydberg EIT has been described in detail in various sources [61], including the PhD theses of former graduate students from this lab [62,63,37]. In this section, I will present the most important equations and conclusions necessary to understand the context of this thesis, primarily drawn from the referenced sources.

In atomic physics, we typically examine how applied laser fields induce transitions within an atomic system. However, to understand EIT, we must also consider the impact that atoms have on the applied field itself, which is particularly important when the field is applied to a collection of atoms. An example from every day life where material alters the light is when light passes through a highly opaque medium, light gets absorbed, and as such, the medium altered the light field. Similarly, when

light encounters a water surface, it is refracted, traveling at a different angle and speed through the water, thereby water changed the light field. In the same way, when an electromagnetic field, such as a laser, is applied to atoms, it excites atomic transitions, inducing atomic dipole moments and these dipole moments generate electric fields that influence the propagation of the laser field.

The property of a medium that determines how light is changed as it propagates through the medium is called susceptibility, χ. When light travels through the medium, the electric field $E(z)$ changes according to the following formula: $E(z) = \mathcal{E}e^{ikz\chi/2}$. Here, the susceptibility χ can be a complex quantity with both real and imaginary parts. Specifically, $\Im[\chi]$ results in exponential attenuation or amplification of the beam intensity, while $\Re[\chi]$ causes a linear phase shift of the field with distance. This phase shift can be understood as a modification of the wavevector k or a change in the refractive index. If the applied field has a finite bandwidth, the frequency dependence of the susceptibility begins to matter, where the the susceptibility term proportional to the frequency will be responsible for the group velocity of the field inside the medium.

To derive the susceptibility of a collection of atoms under a strong control drive probed by weak probing field, we can treat each atom within the ensemble as a three-level system, with an example of levels used in Rydberg EIT indicated in Figure 4.1. Systems driven in this manner can be described by the following Hamiltonian:

$$H = \begin{pmatrix} 0 & \Omega_p/2 & 0 \\ \Omega_p/2 & -i\Gamma - \Delta_p & \Omega_c/2 \\ 0 & \Omega_c/2 & -i\Gamma_r + \Delta_p - \Delta_c \end{pmatrix} \tag{4.1}$$

where Γ is the excited state decay rate (6 MHz for ^{87}Rb atoms), Γ_r is the Rydberg state decay rate (typically a few kHz and can usually be neglected), Ω_p and Ω_c are the Rabi frequencies of the probe and control fields, respectively and Δ_p and Δ_c are the detunings of the probe and control fields.

One can solve this Hamiltonian in steady-state to obtain the atom's density matrix. This requires

assuming weak probe light such that we expect that most of atom's population is in the ground state. The atomic susceptibility will then be proportional to the coherence between the ground and excited states, ρ_{ge}. This leads us to the following formula for the susceptibility:

$$\chi \propto \frac{-i\Gamma_r + (\Delta_p - \Delta_c)}{(\Gamma + i\Delta_p)(\Gamma_r + i(\Delta_p - \Delta_c)) + \Omega_c^2} \tag{4.2}$$

From this expression, we can see that for negligible Γ_r and when $\Delta_p = \Delta_c$, the imaginary part of the susceptibility vanishes. This implies that there will be no attenuation of the probing field, meaning the probe field will be transmitted. The conditions for transmission are also illustrated in Figure 4.1.

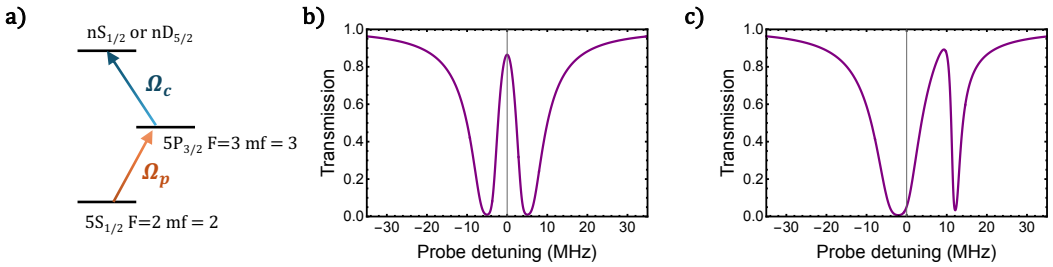


Figure 4.1: EIT in a three-level system: a. Level diagram used for Rydberg EIT experiments. Atoms are optically pumped into the $|5S_{1/2}, F = 2, m_F = 2\rangle$ state. The σ^+ probe light couples them to the $|5P_{3/2}, F = 3, m_F = 3\rangle$ state, from where we use σ^+ control light to couple them to the $nD_{5/2}$ state or σ^- light to couple them to the $nS_{1/2}$ state. **b.** Example of a transmission curve through the atomic ensemble as the probe frequency is scanned, with a 10 MHz control light drive applied on resonance ($\Delta_c = 0$ MHz) to an ensemble with optical density $\mathrm{OD} = 5$. A transmission peak, characteristic of EIT, is observed when the probe light is resonant with the atoms. **c.** Transmission curve showing EIT when the control light is off-resonance by 10 MHz. Here, EIT transmission occurs when $\Delta_p = \Delta_c$, as expected from the susceptibility formula discussed in the main text.

From the real part of the susceptibility, one can derive the refractive index and determine the group velocity of the light within the medium. In this way we can get that the delay time of a probe pulse inside the medium, compared to a pulse traveling in a vacuum is $\mathrm{OD}\frac{\Gamma}{\Omega_c^2}$. From this equation, it is evident that the weaker the Ω_c, the slower the light field propagates within the medium and when $\Omega_c = 0$, the light can be completely stopped within the medium! This phenomenon of light storage has been extensively explored both theoretically[64] and experimentally[65].

4.3 Rydberg EIT

In this section, I will provide some experimental details about Rydberg EIT, how this signal looks like in experiment, what it depends on and how it can be optimized.

Rydberg EIT in this experiment primarily involved coupling the $5S_{1/2}$ state to the $nS_{1/2}$ or $nD_{5/2}$ states through the intermediate $5P_{3/2}$ state. This is a two-photon process as shown in Figure 4.1, where the first transition occurs at 780 nm and the second at 480 nm. For this experiment, both the 780 nm and 480 nm lasers were kept on resonance. Since the 780 nm light couples the ground state to the excited state, resonance for this laser can be easily found using absorption imaging. To find the resonance for the 480 nm laser, we followed the procedure described in section 3.2.

To optimize Rydberg EIT signal one needs to make sure that 480 nm laser beam is aligned properly (same for 780 nm beam, but that one is easier to align since it is 1 mm in waist), that electric field is zeroed out properly and that atoms are correctly optically pumped.

To adjust the alignment of the focused 480 nm laser beam, we used different techniques depending on the 480 nm beam's propagation path. When the control light was sent through an AOD and co-propagated along the same direction as the traps generated by the SLM, as done in chapter 7, the alignment process was more straightforward. In this case, we ensured that the 480 nm beam and the traps were co-propagating before the microscope objective at various points. By adjusting the 480 nm alignment in the intermediate image plane before the microscope, and ensuring that the trap beams and 480 nm beams were perfectly aligned there, the beams were then perfectly aligned in the atomic plane as well. However, if the 480 nm beam comes from an orthogonal direction relative to the trap propagation, the alignment process is different. In this case, we used depletion method. Initially, we align the 480 nm beam using a side trap that co-propagates with the 480 nm beam. This side trap is first aligned with the traps created by the SLM such that it intersects them. Then, we align the 480 nm beam to the side trap beam, depleting atoms in the side trap first and afterwards those in the SLM traps.

It is important to mention here that this alignment process required motorized mirror mounts, and fortunately Chi Shu, a graduate student in Vladan's group, together with Prof. Markus Greiner made motorized mirror mounts that were very cheap for us to build and that made this possible for our lab.

Electric field zeroing is another crucial aspect of optimizing Rydberg EIT, particularly at high Rydberg n levels. When high-intensity 480 nm light (hundreds of mW) is left on for extended periods, it can cause charges to accumulate on the re-entrant window. This accumulation can result in significant electric field changes, which can drastically alter Rydberg atom transitions. For instance, during one experiment at $n = 91$, we observed a 20 MHz resonance shift due to such an electric field change. We corrected this by zeroing out the electric field following the procedure described in section 3.3.

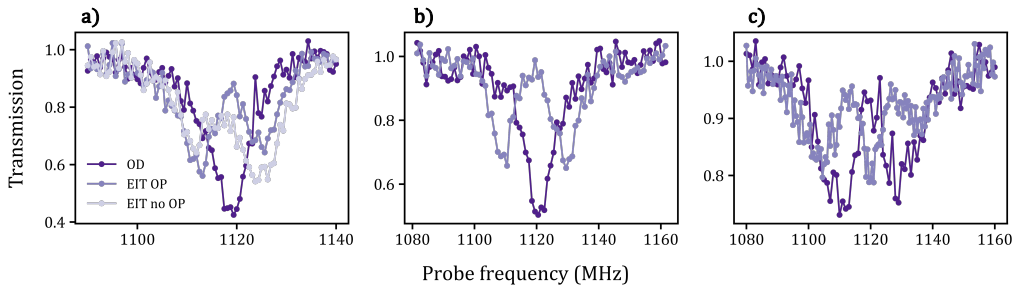


Figure 4.2: Rydberg EIT in Experiments: a. Data illustrating the drastic effect of optical pumping (OP) on the EIT signal. **b.** Example of nice-looking EIT data when all issues mentioned in the main text are resolved. The dark purple curve represents the reference OD curve. **c.** Data showing the resolved MW EIT signal with characteristic triple dip feature. This is contrasted with the EIT data to highlight that MW EIT shows transmission peaks where EIT has dips, and MW EIT shows dips where EIT normally has transmission peaks.

Lastly, optical pumping of atoms into the appropriate state is crucial for achieving the best EIT signal. We followed the procedure described in Zak's thesis [38] to pump our ground state atoms into the $|5S_{1/2}, F = 2, m_F = 2\rangle$ state. Figure 4.2a shows how Rydberg EIT looks like when optical pumping works compared to when it doesn't. I will just mention here that this is not our best looking Rydberg EIT data, as at that time we had an issue we realized only later on. It is noticeable from the data that OD looks a bit slanted, which also affects the EIT signal to look slanted. This distortion was due to our ensembles being very small and dense, causing a lensing effect that bent the imaging light [66]. At

the time we took this data, our camera was looking at the atom plane a few micrometers away from the center of the atomic ensemble, where OD appeared the largest. By adjusting the camera position, we were able to obtain more level OD curves, resulting in significantly better looking EIT signals.

Figure 4.2b shows typical Rydberg EIT spectrum when all these issues are addressed. In our experiments we used mainly $nS_{1/2}$ and $nD_{5/2}$ states for Rydber EIT. Figure 4.2c shows typical MW EIT signal. For experiment in chapter 7, we used this signal only to calibrate the MW drive. This signal can also be used to create polarized MW drives as done in chapter 5.

4.4 EIT FOR COOLING

As mentioned Electromagnetically Induced Transparency can be used for cooling purposes as well. The theory and idea was developed in the late 90s, early 2000s[67] and it was experimentally tested on ions also around that time[68], and more recently to cool down single neutral atoms[46].

In essence, EIT cooling can be intuitively understood as a process where the transition that typically heats atoms is made transparent using the EIT technique, while the transition that cools atoms is made opaque i.e. has high absorption. As a result, atoms predominantly absorb the cooling light and not the heating light, effectively reducing their overall energy.

To achieve EIT cooling, the control light needs to be blue-detuned, as will be explained shortly, while the probe and control light are on two-photon resonance, resulting in the EIT spectrum shown in Figure 4.3b. Atoms inside the trap can be effectively modeled as harmonic oscillators. In a harmonic trap, there are many potential levels n that the oscillator can occupy, and when atoms are hot, they occupy many of these levels.

The energy level diagram used for EIT cooling is shown in Figure 4.3a, where the ground states of the $5S_{1/2}$ level are $|f\rangle = |F = 2, m_F = 1\rangle$ and $|g\rangle = |F = 2, m_F = 2\rangle$. In the EIT process, the control light is stronger than the probe light and performs optical pumping, placing atoms into the $|g\rangle$

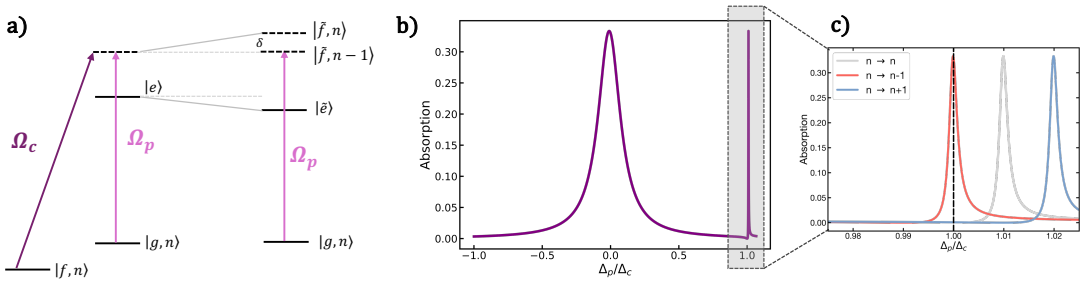


Figure 4.3: D2 EIT Cooling Scheme: a. Level diagram illustrating the transitions used for D2 EIT cooling. By choosing blue-detuned control light that applies the right AC Stark shift δ, the dressed state $|\tilde{f}, n-1\rangle$ can be made resonant with $|g, n\rangle$, for the probe detuning that sets $|g, n\rangle \rightarrow |f, n\rangle$ on EIT resonance. **b.** Blue-detuned EIT absorption spectrum showing two strong absorptions at $\Delta_p = 0 - \delta$, corresponding to the $|\tilde{e}\rangle$ state, and $\Delta_p = \Delta_c + \delta$, corresponding to the $|\tilde{f}, n\rangle$ state. **c.** Zoomed-in level diagram around $\Delta_p = \Delta_c$. This data shows that with the choice of $\delta = \frac{\Omega_c^2}{4\Delta_c} = \nu$ (where ν is the trapping frequency), atoms predominantly absorb light on the "red-sideband" ($|g, n\rangle \rightarrow |\tilde{f}, n-1\rangle$), which cools atoms, rather than on the "blue-sideband" ($|g, n\rangle \rightarrow |\tilde{f}, n+1\rangle$), which would heat atoms.

state. The probe light then probes transitions from this level to the excited state $|e\rangle = |F = 2, m_F = 2\rangle$ of the $5P_{3/2}$ state.

Figure 4.3a shows that strong control light Ω_c, blue-detuned by Δ_c, dresses the $|f\rangle$ and $|e\rangle$ states into AC Stark shifted states $|\tilde{f}\rangle$ and $|\tilde{e}\rangle$, respectively. These states correspond to the two bright states where absorption is high, shown in Figure 4.3b. By keeping the probe and control light detunings equal ($\Delta_p = \Delta_c$) and setting the AC Stark shift $\delta = \frac{\Omega_c^2}{4\Delta_c} = \nu$ (where ν is the trapping frequency), one can make the $|g, n\rangle \rightarrow |\tilde{f}, n-1\rangle$ transition resonant with this probe frequency. Once in $|\tilde{f}, n-1\rangle$ state, atoms will qickly decay to $|g, n-1\rangle$, which causes atoms starting from $|g, n\rangle$ states to predominantly transition to $|g, n-1\rangle$ states, as the scattered light does not change the vibrational frequency level. This process results in the atoms reducing their energy by one vibrational level splitting with each excitation event.

As shown in Figure 4.3c, with the choice of $\Delta_p = \Delta_c$, atoms predominantly scatter photons off of the "red-sideband" that cools atoms, while the $|g, n\rangle \rightarrow |f, n\rangle$ transition remains on pure EIT resonance and hence does not scatter light. The "blue-sideband" transition $|g, n\rangle \rightarrow |\tilde{f}, n+1\rangle$, which

would predominantly heat atoms, has small absorption at this probe detuning but is much weaker than the "red-sideband" absorption[69]. This explains why blue-detuning is necessary for cooling, as it allows the dressed states to be shifted upwards, allowing for cooling transitions to be resonant with the right probe detuning while supressing the heating transitions.

5

Fast, local Rydberg qubit detection

5.1 Introduction

Fast and reliable state initialization and readout of qubits are essential requirements for implementing scalable quantum information systems. Recently, individually-controlled highly excited Rydberg atoms have emerged as a promising platform for quantum simulation and computation[70,22,71,72]. These systems are enabled by the strong coherent interaction between Rydberg atoms at distances

exceeding several micrometers. In combination with the demonstrated ability to deterministically assemble large arrays of individual atoms [19,18,21,73,28,45,20], Rydberg-atom arrays have been used to simulate quantum spin models [22] with more than 250 qubits [74,75,76,77] to perform multiple-qubit gate operations [78,79,80,81,82,83], or to create large maximally entangled states [84]. While these quantum simulation and computation systems can operate on microsecond time scales, they could benefit substantially from faster qubit preparation and detection, as both the array preparation process and the optical state readout in most systems require several to many milliseconds [19,18,21]. Moreover, fast and high-fidelity single-shot qubit readout without atom loss could enable a new generation of experiments with error mitigation, such as quantum error correction and fault tolerant quantum processing [85].

5.2 Fast neutral atom detectors

Prior approaches for individual Rydberg-qubit detection include state-dependent ionization and detection of the ions, a relatively fast ($\tau \sim 0.1$ ms) process that has only moderate fidelity [86], and the state-dependent removal of atoms followed by relatively slow ($\tau \sim 10$ ms) fluorescence imaging of the remaining atoms [87,74,83,88] with relatively high fidelities of $F \gtrsim 0.95$. Fast high-intensity fluorescence detection within 20 μs with single-atom resolution has been achieved in Ref. [89]; however, this method as demonstrated is not compatible with atomic arrays, as it does not have the necessary spatial resolution and also requires a large magnetic field. Both ion detection and fluorescence imaging are destructive readout processes, and require a new atomic array to be prepared subsequently, further limiting the cycle time of the quantum processor.

5.3 Our detection scheme based on Rydberg EIT

Our detection scheme is based on the proposal by Günter *et al.* [90] to use Rydberg interactions in combination with electromagnetically induced transparency (EIT) [91,92] for collectively enhanced imaging.

This method has previously been used to observe Rydberg dynamics[93] without, however, experimentally achieving single-atom resolution. A similar approach has also been used to demonstrate a single-photon switch and a single-photon transistor using Rydberg interactions[94,95,96].

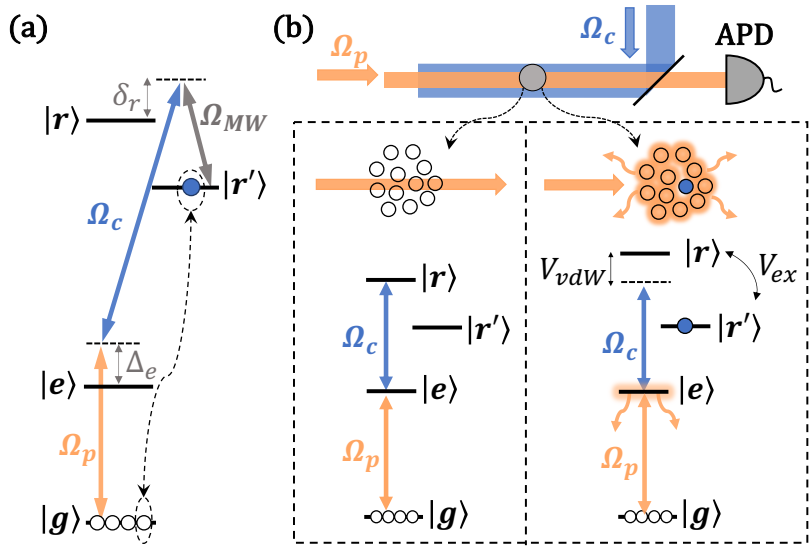


Figure 5.1: Fast collective detector of a single Rydberg atom. a. State initialization. An atom is prepared in the Rydberg state $|r'\rangle$ through a three-photon process involving the preparation beam (Ω_p, orange), the control beam (Ω_c, blue), and a microwave field (Ω_{MW}, grey). The detunings from the two intermediate states are $\Delta_e = \delta_r = 2\pi \times 100$ MHz. The preparation of a single atom in $|r'\rangle$ is ensured by the strong interaction between two atoms in $|r'\rangle$[70]. b. A probe field (orange, waist size $w_p = 4.5\ \mu$m) in combination with the control field ($w_c = 12.5\ \mu$m) couples atoms to the Rydberg state $|r\rangle$. Under conditions of EIT ($\Delta_e = \delta_r = 0$), high transmission through the atomic medium results in a large number of detected photons (left). On the other hand, if the Rydberg state $|r'\rangle$ is populated by an atom (right), then the strong interaction between $|r\rangle$ and $|r'\rangle$ removes the EIT condition, resulting in a significant reduction of transmitted photon number due to absorption by the ensemble. The interaction $V_{rr'}$ contains both dipolar-exchange (V_{ex}) and van-der-Waals components (V_{vdW}) (see SM).

In this work, we demonstrate high-fidelity preparation, manipulation and detection of a single-Rydberg-atom qubit (and not a collective state as in Ref.[97,98]) inside an atomic ensemble on the microsecond time scale. Starting with $N \sim 400$ trapped ultracold ^{87}Rb atoms, we prepare a qubit between the Rydberg states $|\uparrow\rangle \equiv |r'\rangle = |91P_{3/2}, m_j = 3/2\rangle$ and $|\downarrow\rangle \equiv |r\rangle = |92S_{1/2}, m_j = 1/2\rangle$, perform qubit rotations with a loss of contrast $\delta C \leq 2 \times 10^{-3}$ per 2π pulse, and read out the state optically. Harnessing the collective effect of Rydberg blockade[81], the state preparation and detection

are performed in $T_p = 3\,\mu$s and $T_d = 6\,\mu$s with fidelities of $F_p = 0.93 \pm 0.02$ and $F_d = 0.92 \pm 0.04$, respectively. The qubit coherence time of $\tau_c = (15 \pm 5)\,\mu$s, measured with a Ramsey sequence, is much longer than the π rotation time of 90 ns.

Our approach harnesses collective phenomena for speeding up both state preparation and detection. The preparation is accomplished by applying laser and microwave radiation to an ensemble of N atoms, such that any atom can be excited to the Rydberg state, yielding N times faster excitation of the first atom to the Rydberg state than for a single atom, while the preparation of a single excitation is ensured by the Rydberg blockade mechanism[99,74]. Similarly, the signal-to-noise ratio in optical detection is collectively enhanced by a factor $\sim N$: Depending on the state of the single-atom Rydberg qubit, the absorption of probe light by all of the N atoms in the ensemble is simultaneously switched on or off[90].

5.4 Experimental parameters

Our experimental setup is illustrated in Fig. 8.1a. A small ensemble with root-mean-square (rms) size of $\sqrt{\langle r^2 \rangle} \approx 6\,\mu$m containing typically $N \sim 400$ laser-cooled ^{87}Rb atoms is prepared inside a two-beam optical dipole trap with waist sizes $w_1 = 10\,\mu$m and $w_2 = 20\,\mu$m (see Appendix A for details). The trapped atoms are optically pumped into the hyperfine and magnetic sublevel $|g\rangle \equiv |5S_{1/2}, F = 2, m_F = 2\rangle$ that is coupled via a two-photon process involving the transitions $|g\rangle \leftrightarrow |e\rangle \equiv |5P_{3/2}, F = 3, m_F = 3\rangle$ (probe beam Ω_p) and $|e\rangle \leftrightarrow |r\rangle$ (control beam Ω_c) to the Rydberg state $|r\rangle \equiv |92S_{1/2}, m_j = 1/2\rangle$.

5.5 Detection results

To prepare a single atom in the Rydberg state $|r'\rangle$ inside the ensemble, the probe laser and microwave field are detuned by $\Delta_e/(2\pi) = \delta_r/(2\pi) = 100$ MHz from their respective transitions, and in com-

bination with the control field drive a three-photon transition $|g\rangle \leftrightarrow |e\rangle \leftrightarrow |r\rangle \leftrightarrow |r'\rangle$ (see Fig. 8.1a). By changing the powers of the two optical fields within $\sim$3 μs, while keeping the microwave field constant, a process similar to stimulated Raman adiabatic passage (STIRAP) is realized (see Appendix A for details). This process is chosen over direct excitation because it is less sensitive to laser noise and atom number fluctuations. The observed linewidth $\Gamma_3/(2\pi) = 0.6$ MHz of the three-photon transition is much smaller than the energy shift $|\Delta E|/h \gtrsim 10$ MHz at the rms distance $d_0 \equiv \sqrt{2\langle r^2\rangle} \approx 8$ μm between two atoms in their $|r'\rangle$ state in the ensemble (averaged over angles, see Appendix A). This ensures that excitations of two or more atoms to the Rydberg state are suppressed[99,74]. While the $|r'\rangle$ state has vanishing interactions along certain angular directions (see Appendix A), the admixture of the spherically symmetric $|r\rangle$ state with the microwave field during preparation may help increase the preparation fidelity.

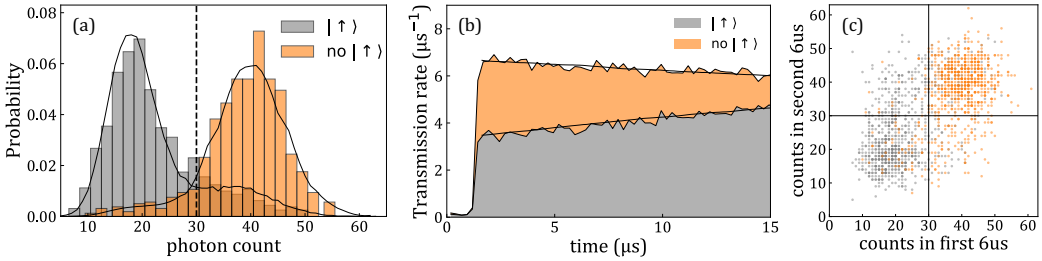


Figure 5.2: a. Histogram of the transmitted probe photon number for state detection performed in 6 μs. Grey and orange histograms correspond to the presence and absence of an atom in Rydberg state $|r'\rangle \equiv |\uparrow\rangle$, respectively. The solid lines in a, b indicate a theoretical model that for the presence (absence) of an atom in $|\uparrow\rangle$ assumes random sudden loss of the Rydberg atom in $|\uparrow\rangle$ (sudden decay of the slow-light polariton into a Rydberg state) at a rate $0.035\ \mu s^{-1}$ ($0.015\ \mu s^{-1}$). The dashed line indicates the detection threshold that gives us the highest fidelity of differentiating two distributions. The control Rabi frequency is $\Omega_c/(2\pi) = 25$ MHz, and the probabilities for collecting and detecting a transmitted probe photon are 0.90 and 0.47, respectively. (b) Time-resolved photon count rate during detection. (c) Correlation plot of number of detected-photon counts in two consecutive 6μs measurements in the same run of the experiment. Gray (orange) points represent transmission data when we prepare (do not prepare) the $|\uparrow\rangle$ state. Vertical and horizontal lines represent threshold counts for state discrimination.

Before discussing how we experimentally verify that only a single Rydberg atom has been prepared, we first describe the detection process. In the following, we associate the Rydberg state $|r'\rangle$ with an effective $|\uparrow\rangle$ state. When the two-photon transition is resonant with the intermediate state ($\Delta_e = 0$,

see Fig. 8.1a), the transmitted probe light serves for Rydberg state detection [90] under conditions of EIT [91,92]. If an atom in $|\uparrow\rangle$ is present, the excitation of a Rydberg polariton to the state $|r\rangle$ at a distance R requires an additional interaction energy that in the presence of both van der Waals and exchange interactions is approximately given by $V_{rr'} = C_6/R^6 \pm C_3/R^3$, where $C_6/h = 6310\ \mathrm{GHz}\,\mu\mathrm{m}^6$ and $C_3/h = 23.6\ \mathrm{GHz}\,\mu\mathrm{m}^3$ (see Appendix A). This interaction energy shifts the EIT resonance and results in a lower transmission of the probe beam for the state $|\uparrow\rangle$.

Fig. 5.2a shows the observed photon count histograms of the transmitted light in a 6-μs detection window with and without an atom in $|\uparrow\rangle$. Even in such a short time, the two photon count distributions can be clearly distinguished. The time-resolved average count rate (Fig. 5.2b) reveals that the transmission $T_{|\uparrow\rangle}$ for $|\uparrow\rangle$ increases with time, whereas the high transmission without an atom in $|\uparrow\rangle$ is almost constant, and decreases only slowly. The latter may be explained by a decay of the slow-light $|r\rangle$-polaritons to other Rydberg states, producing randomly a stationary atom in some Rydberg state, that then blocks the EIT transmission. The increase in the average transmission $T_{|\uparrow\rangle}$, on the other hand, can be explained by a light-induced loss process of the Rydberg atom in $|\uparrow\rangle$ during detection, which leads to a sudden increase in transmission at a random time. The observed signal reduction is primarily associated with the control light, and is too fast to be explained by photoionization [100,101] or the repulsive ac-Stark shift (see Appendix A for details). We hypothesize that a small residual electric field of a few 10 mV/cm mixes a $|92S\rangle$ component into the $|91P\rangle$ state, so that the control light can couple the $|\uparrow\rangle$ state, which contains a small component of $|92S\rangle$ in it, to the rapidly decaying $|e\rangle$ state, causing a sudden loss of the atom in $|\uparrow\rangle$.

Modelling the system as a removal of blockade at a random time yields excellent agreement with the photon count histograms observed at different detection times (see Appendix A). From this we infer a preparation fidelity for the state $|\uparrow\rangle$ (i.e., an atom in $|r'\rangle$) of $F_p = 0.93 \pm 0.02$ (see Appendix A for details). The detection fidelity (probability of correctly identifying the underlying state $|\uparrow\rangle$) after removing the state preparation error is then $F_d = 0.92 \pm 0.04$.

Fig. 5.2c demonstrates that we can perform repeated ('non-destructive') measurements on the system, where a second 6-μs measurement yields good agreement with the first measurement: The average conditional probability for the second measurement to have the same outcome as the first measurement is $p = 0.79 \pm 0.03$ (see Appendix A for details). The detection system can also be viewed as a single-atom transistor for light. We then achieve a gain of $G = 17 \pm 1$ in 6 μs, somewhat larger than the gain of $G = 10$ in 30 μs achieved in the Rydberg system of Ref.[95].

5.6 Rydberg qubit within a micro-ensemble

We implement a qubit in our system by defining the state with a single atom in $|r\rangle$ as the $|\downarrow\rangle$ state. Coherent rotations in the $\{|\uparrow\rangle, |\downarrow\rangle\}$ manifold are induced by applying the microwave field. After a qubit rotation, we detect the resulting state by turning on the coupling light slightly (1 μs) earlier than the probe light, such that the state $|r\rangle$ is quickly de-excited by the strong coupling laser to the unstable state $|e\rangle$, which decays by photon emission in 30 ns (see Fig. 8.1). Thus, as far as the detection process is concerned, the state $|\downarrow\rangle$ (atom in $|r\rangle$) is equivalent to having no Rydberg excitation at all, while the state $|\uparrow\rangle$ (atom in $|r'\rangle$) remains unaffected by the detection light, and leads to Rydberg blockade of the probe transmission. If the photon count is above or below a chosen detection threshold (see Fig. 5.2a), we identify the qubit state as $|\downarrow\rangle$ or $|\uparrow\rangle$, respectively.

Fig. 5.3 shows Rabi oscillations with the full sequence of state preparation, qubit rotation, and detection. The trap light is turned off during the sequence to avoid light shifts of the states. We use two microwave antennas with adjusted relative phase and amplitude to suppress the π polarization component of the microwave field that can couple atoms in $|\downarrow\rangle$ to the magnetic sublevel $m_j = 1/2$ in the $91P_{3/2}$ manifold, offset by 17 MHz in an applied magnetic field of 9 G. The remaining coupling to other magnetic sublevels limits the maximum Rabi frequency on the $|\uparrow\rangle \leftrightarrow |\downarrow\rangle$ transition to $\lesssim$ 5 MHz. The Rabi oscillations show no observable damping on the 6 μs timescale, corresponding to a

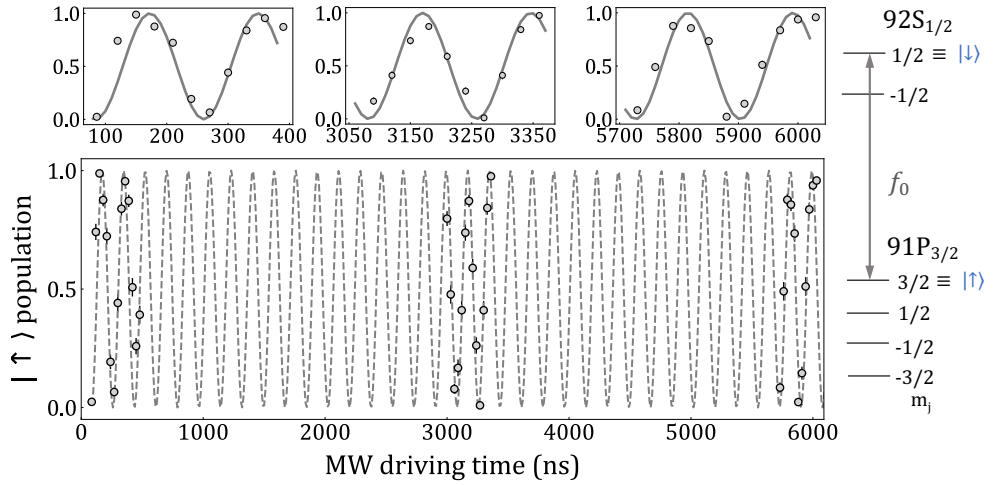


Figure 5.3: A microwave field at a frequency $f_0 = 4814.2$ MHz is applied to drive Rabi oscillations between $|\uparrow\rangle$ and $|\downarrow\rangle$ at an oscillation frequency $\Omega/(2\pi) = 5.3$ MHz. Each point is an average of ~ 150 repetitions. The error bars are the standard deviation of the mean. The fitted contrast loss per 2π pulse is $\delta C < 2 \times 10^{-3}$. The relevant energy level diagrams are shown on the right.

contrast loss per 2π pulse of $\delta C \leq 2 \times 10^{-3}$.

5.7 Probability that single Rydberg atom is prepared

The observed contrast of the Rabi oscillations can be used to determine the probability that two excitations in $|r'\rangle$ were simultaneously created in the ensemble. Due to the large interaction energy between two atoms in $|r'\rangle$ and $|r\rangle$, the Rabi oscillations with two excitations would very quickly wash out on a time scale $h/V_{rr'}(d_0) \sim 40$ ns. From the observed contrast of the Rabi oscillation we conclude that the probability for preparing two excitations is below 1%.

5.8 Qubit coherence time

We use a Ramsey measurement to characterize the coherence time of the Rydberg qubit embedded inside the atomic cloud. Two $\pi/2$ pulses are applied with a temporal separation τ between them, and

their relative phase is scanned to obtain a Ramsey fringe at given τ. Fig. A.2 displays the contrast of the Ramsey fringes as a function of Ramsey time τ. By fitting the contrast to a Gaussian decay function, we obtain the e^{-2} dephasing time as (15 ± 5) μs. Possible dephasing mechanisms include electric-field fluctuations acting on the highly polarizable Rydberg states, magnetic field fluctuations, and interactions between the Rydberg atom and the surrounding ground state atoms [102]. We also note that neither the Rabi flopping nor the Ramsey measurement depend on whether we have encoded the qubit in a single atom or collectively in a W-state [97]. However, previous measurements involving storage and retrieval of photons indicate that the collective state decoheres during preparation, such that the qubit is ultimately encoded in a single atom [103].

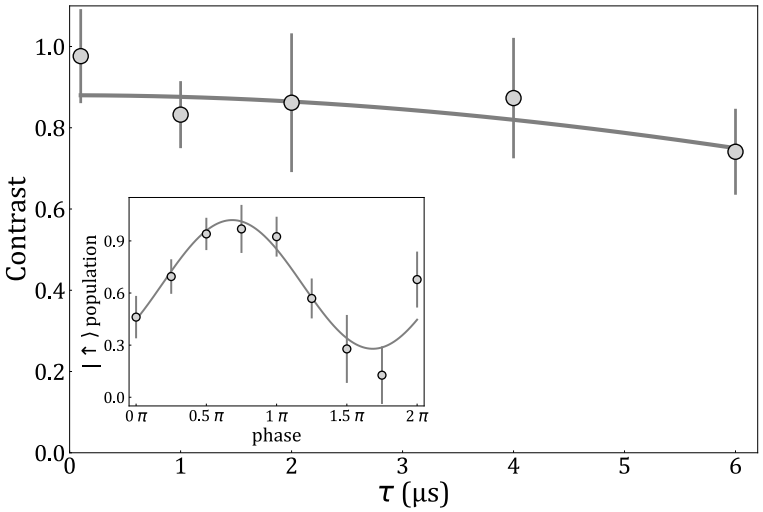


Figure 5.4: Ramsey measurements consisting of two $\pi/2$ pulses separated by a time τ. The phase of the second $\pi/2$ pulse is scanned to obtain a Ramsey fringe. The contrast of the Ramsey fringe is plotted as a function of τ. The solid curve is a fit to a Gaussian decay function $Ae^{-(\tau/T_2^*)^2}$, yielding a dephasing time $T_2^* = (15 \pm 5)$ μs and $A = 0.88 \pm 0.04$. Inset: Ramsey fringe at $\tau = 1000$ ns.

5.9 Conclusion and Outlook

In summary, by harnessing collective effects in a small atomic ensemble, we have demonstrated a method for the rapid preparation and detection of a Rydberg qubit. The preparation and detection fidelities demonstrated in this work can likely be further increased in the future. The preparation fidelity for a single excitation can be improved by modifying the preparation sequence (see Appendix A) or using smaller ensemble size, since such ensembles would provide even higher energy cost for multiple excitation. The size of the ensemble cannot, however, be made arbitrarily small, since at higher atomic densities, necessary to maintain the same optical depth $OD \sim 1$, Rydberg molecule formation [104] could lead to loss. Given our current average atomic density of $\langle n \rangle = 2\times10^{11}\,\mathrm{cm}^{-3}$, reducing the ensemble size by a factor of 2 should be possible, which would likely reduce the preparation error by more than an order of magnitude.

Our demonstrated detection fidelity, on the other hand, is limited by the loss of the Rydberg atom prepared in the $|r\rangle$ state. This loss is mainly caused by the control light in the detection stage, and thus could be mitigated by using two ensembles, one for hosting the qubit and the other for detection, located within a blockade radius from each other. Assuming a measurement time of $10\,\mu$s, this configuration could allow for a non-destructive, fast qubit readout with detection fidelity over 99%, a crucial tool necessary for implementing quantum error correction [85]. In addition, such a readout can also enable studies of quantum feedback [105], quantum Zeno effect [106], quantum jumps [107], and can act as a fast probe of Rydberg super-atom dynamics [108].

The detection scheme can be readily implemented in different Rydberg platforms [75,22,21], where a single atom would be replaced by a small ensemble, as demonstrated in Ref. [109]. Alternatively, one can place a small ensemble within the Rydberg blockade radius of each single atom for fast detection, or even within the blockade radius of several single atoms for fast parity measurements, and possibly even error correction. To suppress diffusion of the Rydberg atom between different ensembles due

to the exchange interaction during detection, it may be necessary to adjust the lattice constant of the array or the principal quantum numbers of the Rydberg states used.

6

Bose-Einstein condensation by polarization gradient laser cooling

6.1 Introduction

Quantum degenerate gases provide an attractive platform for testing fundamental physics[110,111] and simulating various quantum many-body systems[112,113]. In most experiments, highly efficient laser

cooling, Doppler cooling, followed by polarization gradient cooling (PGC) takes an atomic gas from room temperature to sub-mK temperatures [13,114]. At this point, the gas is trapped with a typical occupation per quantum state (phase space density, PSD) of $\sim 10^{-6}$, limited by detrimental light-induced processes such as photon reabsorption heating and atom loss. Subsequently, to reach the degeneracy, evaporative cooling [115] is applied. The latter is a robust method requiring only favorable atomic ground state collision properties, however, the process is slow and necessarily accompanied by a reduction in atom number.

Recently, alternative optical cooling techniques have been developed that can reach the quantum degenerate regime faster [116,117,118,119,44,120]. The main obstacle to overcome is light-induced collisional loss at higher atomic densities and within the Bose Einstein condensate (BEC) [121]. For Sr atoms, which feature a narrow optical transition, Florian Schreck and colleagues have made use of a strongly inhomogeneous trapping potential to spectrally decouple the emerging BEC from the cooling light [116], even demonstrating the first continuous creation of a BEC [117]. For alkali atoms, without a convenient narrow transition, Raman cooling can be employed to mimic a narrower transition using an additional laser field to adjust the effective transition linewidth [114,122,123]. This approach has enabled laser cooling to quantum degeneracy in Rb [119,44] and Cs [124], however, such techniques require a higher degree of experimental complexity in addition to the PGC already necessary. It has been the general consensus that optical cooling to Bose-Einstein condensation requires relatively sophisticated, finely-tuned techniques, and cannot be accomplished by PGC alone.

In this work, we observe the direct formation of a Bose-Einstein condensate of ^{87}Rb atoms using only PGC inside a corrugated potential. The cooling is applied to atoms trapped inside a perturbed optical tweezer, which is formed by intentionally misaligning the trapping light through a high-numerical-aperture microscope objective lens. A small fraction (up to $\sim 11\%$) of the atoms ($N \sim 2500$) forms a BEC, as revealed by a bimodal and anisotropic velocity distribution observed in time-of-flight (TOF) imaging. The BEC formation was first discovered accidentally using a machine

learning algorithm designed to maximize the atom number loaded into the misaligned microscopic trap. For traps created by laser beams well-aligned to the microscope objective, we do not observe a condensed component, but we consistently recover condensation in traps misaligned to the microscope. Furthermore, BECs can be generated controllably using a spatial light modulator (SLM) to imprint a speckle-like phase pattern, or by superposing two closely spaced traps. We believe that interference creates dimple structures in the trapping potential that lower the trap depth below the chemical potential of the system, thus facilitating local condensate formation [125,126,127,128].

6.2 Experimental setup and machine learning optimized trap loading

Experimental setup is shown in Fig. 8.1. The optical dipole trap is generated with a Gaussian laser beam ($\lambda = 808\,\text{nm}$) focused to various beam waists ($w_0 = 2 - 5\,\mu\text{m}$) through a microscope objective lens (Mitutoyo M Plan Apo NIR B 20X 378–867–5, numerical aperture $NA = 0.4$), with the trapping beam slightly tilted ($\sim 3^\circ$) away from normal incidence on the objective.

^{87}Rb atoms are loaded into the dipole trap from a magneto-optical trap (MOT). The experimental sequence consists of a 500-ms-long MOT cooling and loading stage, followed by a 40-ms-long MOT compression stage at increased magnetic field gradient, during which atoms are loaded into the dipole trap. The dipole trap depth is typically $U/h = 8\,\text{MHz}$ (i.e. $U/k_B = 400\,\mu\text{K}$), with measured radial and axial vibration frequencies of $\omega_r/(2\pi) = 18\,\text{kHz}$ and $\omega_z/(2\pi) = 0.8\,\text{kHz}$, respectively.

The various parameters (laser intensities and frequencies, bias magnetic fields along x, y, z, and magnetic field gradient) for the dipole trap loading during the MOT compression stage were optimized with an open-source, machine learning optimization package (M-LOOP)[48], which has been used previously for improving laser cooling to Bose-Einstein condensation [120]. In this work, we use the number of atoms loaded into the dipole trap as our cost function. We divide the 40-ms-long MOT compression stage into three time bins during which we allow M-LOOP to vary 27 parameters

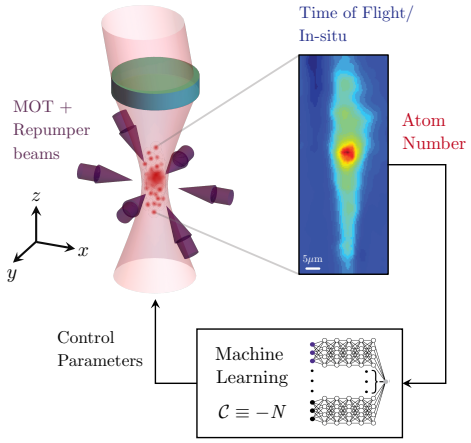


Figure 6.1: Schematic of the experimental setup for direct polarization gradient cooling to Bose-Einstein condensation in a corrugated optical potential. The optical dipole trap ($\lambda = 808$ nm) is slightly misaligned on a microscope objective lens with numerical aperture $\mathrm{NA} = 0.4$, resulting in small-scale corrugations of the trapping potential with waist $w_0 \approx 3.5\,\mu$m. To maximize the phase space density and reach condensation, machine learning is used to increase the atom number loaded into the trap by tuning the trap loading and cooling parameters (see text). A time-of-flight (TOF) absorption image (right) shows a bimodal momentum distribution. The high-density peak contains , at most, 11% of the atoms ($N = 2300$).

in total: the durations of the time bins, the beam powers and detunings of the MOT laser on the $|5S_{1/2}, F = 2\rangle \rightarrow |5P_{3/2}, F = 3\rangle$ transition, and of the repumper laser on the $|5S_{1/2}, F = 1\rangle \rightarrow |5P_{3/2}, F = 2\rangle$ transition, the magnetic fields B_x, B_y, B_z, and the gradient of the magnetic quadrupole field. The parameters during the different time bins are connected via linear ramps, except for the laser frequencies, which are jumped in < 1 ms (see Appendix B for details). Initial values of all parameters for the MOT compression stage are carried over from the previous MOT loading stage and were chosen by hand.

The optimized sequence obtained by the algorithm, presented in Appendix B, increased the number of loaded atoms by up to a factor of 5 compared to human optimization, while simultaneously decreasing the temperature by a factor of 2.5, overall improving the phase space density by two orders of magnitude. To increase the atomic density and reduce light-induced repulsion forces [129,130] and losses [121], the algorithm ramps down the intensity of the repumper laser by a factor of ~ 300, which

transfers most of the atoms into the $F = 1$ manifold, and reduces photon scattering. Additionally, the algorithm increases the MOT laser detuning from the $|5S_{1/2}, F = 2\rangle \rightarrow |5P_{3/2}, F = 3\rangle$ transition to -180 MHz during the final time bin to produce colder temperatures via blue-detuned PGC on the $|5S_{1/2}, F = 2\rangle \rightarrow |5P_{3/2}, F = 2\rangle$ transition [131]. The algorithm further increases the magnetic field gradient to ~ 25 G/cm to achieve higher atomic density during dipole trap loading, while the chosen bias magnetic field positions the atomic ensemble at the dipole trap location, maximizing the loading efficiency. All of these are known techniques from human optimization. The algorithm manages to load as many as $N = 2300$ atoms into a microscopic dipole trap with beam waist $w_0 = 3\,\mu$m, at a temperature of $T \approx 40\,\mu$K, well below the Doppler temperature of $140\,\mu$K, while the recoil temperature is 360 nK. Note that such temperatures and densities have been achieved with PGC alone [120], while lower temperatures (e.g. $10\,\mu$K) have been reported only at the expense of lower atomic density [127]. This large atom number is remarkable given that under other loading conditions, such traps can be made to load only a single atom [132].

6.3 BEC observation in a time of flight measurement

Following the M-LOOP-optimized trap loading, the atoms are held in the dipole trap for an additional $50 - 300$ ms to allow the ensemble to thermalize, with typical estimated two-body collision rates of $\Gamma_c \approx 2.2 \times 10^3$ s^{-1} at peak densities $n_0 \approx 5 \times 10^{13}$ cm^{-3} of the thermal cloud. [1] Absorption imaging *in-situ* shows a local density peak inside the dipole trap, which indicates a corrugation in the optical potential of the deformed trapping beam. The TOF measurement of the atomic-cloud expansion (Fig. 6.2a) reveals significantly different expansions of the high-density peak and of the thermal cloud. As shown in Fig. 6.2b, the thermal cloud expands isotropically in the radial and axial directions with

[1] During this $50 - 300$ ms long thermalization stage, unforced evaporative cooling occurs, where 10-30% of the atoms are lost while the temperature decreases by 10-20%. Despite this stage decreasing the phase space density by at most a factor of 2, this stage alone does not play a significant role for the BEC formation.

temperatures of $T_x = 2K_x/k_B = 36(2)\,\mu$K and $T_z = 2K_y/k_B = 42(2)\,\mu$K, while the dense peak expands anisotropically with much lower kinetic energies $2K_x^{(0)}/k_B = 1.4(2)\,\mu$K and $2K_z^{(0)}/k_B < 0.2\,\mu$K. In particular, the expansion in the axial (z) direction is too small to be resolved by the imaging system. This anisotropic expansion — well-below the expansion rate of the thermal gas — is a hallmark signature of BEC formation [15]. A bimodal fit reveals an observed condensate fraction of up to 11%.

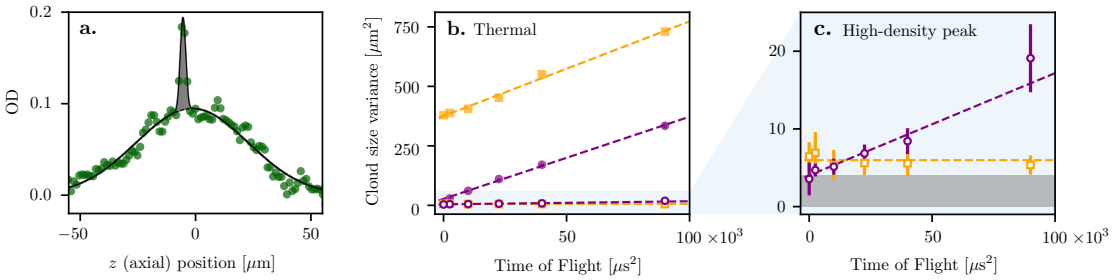


Figure 6.2: a. TOF distribution after 400 μs shows a high-density peak (gray shaded region) on top of the thermal cloud. **b.** Variances of the thermal cloud (filled symbols), and **c.** the high-density peak (empty symbols) as a function of the TOF. Purple and yellow markers correspond to expansion along the x (transverse) and z (axial) directions, respectively. The thermal cloud fits to temperatures of $T_x = 2K_x/k_B = 36(2)$ μK and $T_z = 2K_z/k_B = 42(2)$ μK along x and z, respectively, with $N = 2.7(1) \times 10^3$. The high-density peak expands anisotropically with much lower kinetic energies of expansion $2K_x^{(0)}/k_B = 1.4(2)\,\mu$K and $2K_z^{(0)}/k_B < 0.2\,\mu$K. The gray shaded region (below $4\,\mu$m^2) indicates the imaging resolution.

6.4 Dimple hypothesis

What is staggering about this observation is that after our machine learning optimized cooling, atoms inside of the large trap are at the phase space density of $\sim 10^{-3}$, three orders of magnitude away from what is known is needed to cross the phase space density for condensation. However, from the time-of-flight measurements presented in previous section, we know that BEC is formed inside of the trap, and the question is how is this possible. At this point, the micrometer size of the trap along with the slight misalignment of it on the microscope objective comes into play.

We hypothesize that interference in the aberrated trapping beam (from spurious reflections in the microscope objective) creates corrugations in the potential (local trap dimples), where the local

trap potential drops below the chemical potential (see Fig. 6.3a) such that a local condensate can form [125,126,127,128,133]. The stronger confinement of the local dimple relative to the macroscopic trap enhances the local phase space density of atoms inside the dimple. When the volume of the dimple is significantly smaller than that of the macroscopic trap, the phase space density PSD_d within the dimple increases exponentially with the depth of the dimple [128]:

$$\ln(\mathrm{PSD}_d/\mathrm{PSD}) = \frac{U_d/(k_B T)}{1 + (V_d/V)e^{U_d/(k_B T)}}. \tag{6.1}$$

Here, U_d is the additional trap depth provided by the dimple, and V, V_d are the volumes of the macroscopic and dimple traps, respectively. The expression is an approximation assuming box-shaped trapping potentials and $V_d/V \ll 1$. For smaller volume ratios V_d/V, a weaker dimple potential is sufficient to create a BEC. The largest possible increase in phase space density is $\mathrm{PSD}_d/\mathrm{PSD} \sim V/V_d$, obtained for a dimple depth of $U_d/(k_B T) \approx \ln(V/V_d)$. For our parameters, this implies that a volume ratio $V_d/V \lesssim 10^{-3}$ is needed, in combination with an additional dimple potential depth $U_d \approx 6.9 k_B T \approx h \times 5.5\,\mathrm{MHz}$.

The smallest characteristic structure size of the interference speckle pattern can be estimated as $\delta x_d \sim \lambda/(2 \times NA) \approx 1.2\lambda$, yielding a maximum volume ratio (and hence local PSD increase) of $V/V_d \sim 2\pi^2 w_0^4/\lambda^4 \approx 1.5 \times 10^3$, matching what is required to explain the BEC formation. For the thermal gas in V, the chemical potential calculated from its temperature and atom number is approximately $U_d \approx h \times 5.5\,\mathrm{MHz}$, satisfying the BEC formation condition.

6.5 Dimple hypothesis - experimental tests

6.5.1 BEC formation dependence on the trap waist and alignment

We investigated the dependence of BEC formation on the dipole trapping beam waist w_0 and on the misalignment angle between the incident beam and the optical axis of the microscope objective. We found that the trap size is critical: while we observe BEC formation in a dipole trap with $w_0 = 3.5\,\mu$m, no condensation was observed for waists $w_1 = 2.4\,\mu$m or $w_2 = 4.5\,\mu$m. For the smaller beam waist w_1, higher light-induced loss during the loading stage[134] into the tighter trap resulted in a smaller loaded atom number $N = 800$, and smaller phase space density PSD for the thermal cloud, which was too low to allow BEC formation. On the other hand, for the larger beam waist w_2, the dimple depth is likely too small to reach the chemical potential (Fig. 6.3a).

Once a proper dipole trap beam waist is chosen and the trap is misaligned, the formation of the BEC is reproducible and robust. We verified that BEC formation persists at various angles of misalignment, but the density peak can occur at different locations inside the trap; often, multiple high-density peaks exhibiting anisotropic expansion in TOF are observed (see Appendix B). In contrast, when the beam is aligned at normal incidence to the microscope objective, we observe only a thermal cloud, without density anomalies or bimodal TOF distributions. This observation confirms that the right misalignment of the beam, which comes with right amount of corrugation is needed in our trap to reach the degeneracy.

6.5.2 BEC formation on-demand using SLM

In order to test our dimple hypothesis further and also create BECs under more controlled conditions, we introduced an SLM in the optical path of the trapping beam. We were then able to observe on-demand BEC formation for trapping beams well-aligned to the optical axis of the microscope in two

different configurations of the SLM. First, we used the SLM to generate two traps of 2 μm waist and observed BEC formation when the trap separation was chosen to lie in the range $3.3 - 3.7\,\mu$m, creating interference between the traps. Second, we also observed BEC formation when we introduced a speckle-like pattern consisting of many diffraction orders generated by sine phase functions displayed on the SLM, superimposing three waves with small wavenumbers (and thus small trap spacing in the atom plane) and random phase offsets.

In both cases, we observed persistent BEC formation, but the condensate fractions were smaller than in the data presented in Figs. 8.1 and6.2. However, with the capabilities introduced by an SLM, we envision possibilities to engineer more complex optical potentials in which the BEC fraction can be improved via the generation of sub–diffraction–limited dimples [135,136]. A gallery of different BECs observed in various traps is shown in the Appendix B.

6.6 Loss of BEC atoms during time-of-flight

To further verify the BEC formation, we vary the classical phase space density (PSD) of the thermal cloud and measure the corresponding condensate fraction (see Fig. 6.3b). To change the phase space density in the trap, we use the same M-LOOP-optimized loading sequence and subsequently ramp up or down the dipole trap depth within 20 ms, and finally hold the atoms in the trap for an additional 20 ms before TOF imaging. It is evident that higher (lower) PSD yields larger (smaller) condensate fractions, as expected, since the hottest (thermal) atoms escape the trapping potential.

Notably, while the BEC persists in-trap over timescales of a few hundred milliseconds, we observe atom loss from the condensate during TOF measurements (see Fig. 6.3c). This atom loss during TOF is consistent with two-body elastic collisions between non-condensed atoms from the larger trap and condensate atoms (see Appendix B). In-trap, the atom number in the BEC remains constant because there is a dynamic equilibrium between scattering into and out of the condensate. During TOF, how-

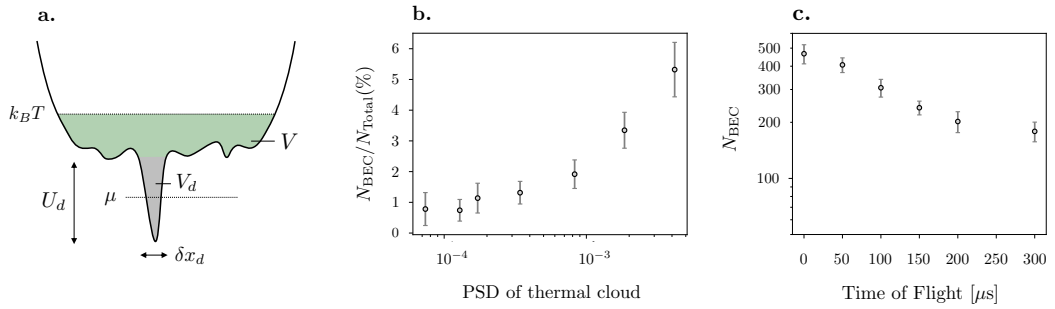


Figure 6.3: **a.** Corrugations in the optical potential enable BEC formation when the additional trap depth U_d drops below the chemical potential μ. Interference of the trapping beam generates diffraction-limited structures of size $\approx \lambda$, which can exponentially enhance the local PSD$_d$ in the dimple (gray shaded region) with respect to the classical PSD of the thermal cloud (blue shaded region). **b.** Fraction of atoms in the BEC peak as a function of PSD in the thermal cloud. The PSD is tuned by ramping up or down the trap power following M-LOOP-optimized dipole trap loading. The data was taken after a TOF of 100 µs for $N = 3700(200)$, resulting in up to 200 atoms in the BEC. **c.** Number of atoms in the condensate as a function of TOF delay shows fast loss as the cloud expands. In-trap, however, the condensate persists for hundreds of milliseconds.

ever, the thermal cloud disperses quickly, and loss of atoms from the condensate cannot be recovered via elastic collisions with the thermal atoms. At short TOF, the loss of the condensate may be further enhanced due to the presence of thermal atoms confined within the dimple potential. As the thermal cloud density decreases during TOF expansion, the loss from the condensate stops. A second possible explanation for condensate loss in TOF is three-body loss [130] (see Appendix B; note that two-body inelastic collisions should be negligible since the algorithm prepares the atoms in the $F = 1$ ground state.) However, the long BEC lifetime in-trap suggests that three-body loss is unlikely to be the dominant loss mechanism on the time scale shown in Fig. 6.3c.

6.7 Conclusion and outlook

In summary, we have, for the first time, observed the direct formation of a BEC using only regular optical molasses (PGC) laser cooling, overturning a long-held paradigm that PGC is insufficient for reaching quantum degeneracy. Given the similar properties among alkali atoms, we anticipate that this technique can be applied to other atomic species suffering from large light-induced losses. The

cooling is accomplished within a duration as short as 40 ms, which is an order of magnitude faster than that achieved in other works [120,118]. While the total cooling duration was kept fixed in this work, we envision possibilities of increasing the condensate fraction (or reducing the cooling duration) by varying the chosen cost function for the optimizer, to explore the known trade-off between atom number and temperature [120]. Additionally, the duration of MOT loading can be easily reduced by employing a 2D MOT, which would significantly improve the cycle time [137]. Combining this method with arrays of optical tweezers [19,18], it should be possible to create hundreds of small condensates simultaneously, and purify them by lowering the trap power. This may constitute, e.g., a promising starting point for atom interferometry [138,139] and other precision experiments with ultracold atoms.

7

Long range detection of a single Rydberg atom via hopping with Rydberg polaritons

7.1 Introduction

Interactions between atoms in high-lying energy states, also known as Rydberg states [22], have played a crucial role in recent discoveries and technological advancements. Manifesting in dipolar exchange [140]

or blockade[74] mechanisms, Rydberg interactions have enabled the generation of squeezed atomic states[29,141,142] for quantum metrology applications and the development of neutral atom quantum processors with high-fidelity gates[24,26,25], supporting demonstrations of encoded logical qubits[11]. In the realm of fundamental physics, Rydberg interactions have enabled quantum simulations of complex[27,5] quantum many-body phases, and mediated effective interactions between photons via Electromagnetically-induced transparency (EIT)[103,65,143].

The latter efforts have uncovered intriguing phenomena: for example, a photon can form a Rydberg polariton[64] and collide with a stationary Rydberg atom, resulting in either increased absorption[103] or a phase shift[65,144]. Such state-dependent effects have lead to demonstrations of single-photon transistors and photonic gates mediated by atomic ensembles[94,95,96]. It was further proposed[145] that precise control over the atom-polariton interaction parameters can be achieved by placing a single Rydberg excitation and an atomic ensemble hosting Rydberg polaritons in separate spatial modes and controlling the distance between them. However, such a scheme had yet to be experimentally realized.

Here, we demonstrate full control over the interaction between a stationary Rydberg atom prepared next to propagating Rydberg polaritons, showcasing three distinct regimes: blockade, coherent exchange, and incoherent (classical) hopping. We experimentally verify the expected behaviour in each regime, and we investigate their utility for fast, long-range and non-destructive detection of Rydberg atoms by observing, for the first time, coherent Rabi oscillations of a prepared Rydberg atom by non-local detection with a neighbouring ensemble. Our results suggest that reliable, high-fidelity detection applications should be explored predominantly in the blockade regime, in which the signal-to-noise ratio is not limited by the population of Rydberg atoms. Since our scheme is readily scalable, we expect our findings to support arrays of detector ensembles next to single atoms for next-generation neutral atom quantum processors, while enabling novel methods to build quantum photonic networks[145] and quantum random walks with inherent nonlinearity[146].

7.2 Experimental setup

Our experimental setup is illustrated in Fig. 7.1c. We load ^{87}Rb ensembles in an array of dipole traps ($\lambda = 808\,\text{nm}$, $w_0 = 4.9\,\mu\text{m}$) generated by a spatial light modulator (SLM). After loading, we dynamically compress the ensembles to reduce the axial cloud size and improve confinement with two sheets of blue-detuned beams ($\lambda = 770\,\text{nm}$, $w_0 = 4\,\mu\text{m} \times 32\,\mu\text{m}$), generated by a one-dimensional acousto-optic deflector (AOD). After these steps each dipole trap hosts an ensemble with ~ 200 atoms within $\sigma_x = 2\,\mu\text{m}, \sigma_y = 2.5\,\mu\text{m}, \sigma_z = 4\,\mu\text{m}$.

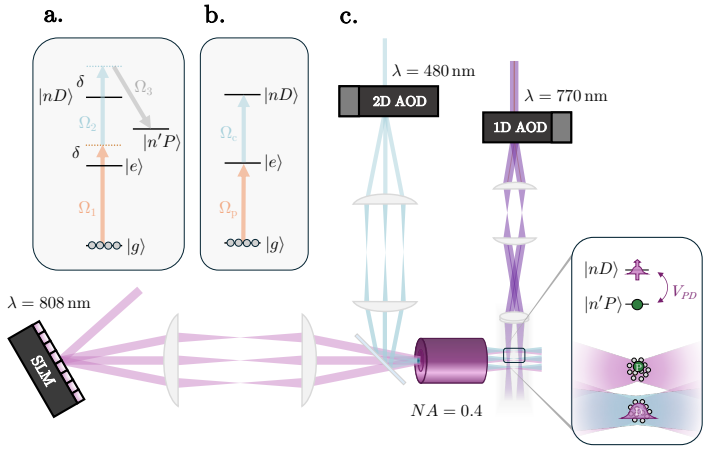


Figure 7.1: Preparation and detection scheme, and schematic of the apparatus: a. Three-photon scheme which prepares a single Rydberg atom in the state $|n'P\rangle = |75\text{P}_{3/2}, m_J = 3/2\rangle$ within the ensemble. The first and third legs of the three-photon transition ($780\,\text{nm}$ and microwave fields with Rabi frequencies Ω_1, Ω_3) are detuned by $\delta = +100\,\text{MHz}$ from resonance of their respective transitions, while the $480\,\text{nm}$ light with Rabi frequency Ω_2 is on-resonance with $|e\rangle = |5P_{3/2}, F = 3, m_F = 3\rangle \rightarrow |nD\rangle = |74\text{D}_{5/2}, m_J = 5/2\rangle$. **b.** Rydberg EIT scheme, in which both the probe and control fields (with Rabi frequencies Ω_p, Ω_c) are on-resonance with their respective transitions. **c.** Schematic of the setup illustrates the trap configuration, which creates small ensembles using $808\,\text{nm}$ SLM traps and $770\,\text{nm}$ AOD beams. A site-selective $480\,\text{nm}$ control field (blue) is controlled via a two-dimensional AOD and co-propagates with the SLM traps, while a global $780\,\text{nm}$ probe field (not depicted) is sent through the microscope objective in the opposite direction. (Zoom-in) Dipole-dipole interactions V_{PD} between a stationary Rydberg atom in $|n'P\rangle$ and travelling Rydberg polaritons in $|nD\rangle$ result in symmetric splitting of dressed states, in contrast to van der Waals interactions.

For our detection scheme, we perform absorption imaging of ensembles, with typical peak optical densities $\text{OD} \approx 2$ per ensemble, with a probe beam which is sent through a microscope ob-

jective (numerical aperture NA $= 0.4$). Fig. 7.1b illustrates the Rydberg EIT scheme: a weak 780 nm field ($\Omega_p/(2\pi) \approx 100 - 300$ kHz) probes the transition between the ground state $|g\rangle = |5S_{1/2}, F = 2, m_F = 2\rangle$ and excited state $|e\rangle = |5P_{3/2}, F = 3, m_F = 3\rangle$, while a strong 480 nm control field ($\Omega_c/(2\pi) = 5 - 20$ MHz) couples $|e\rangle$ to the Rydberg state $|nD\rangle = |74\mathrm{D}_{5/2}, m_J = 5/2\rangle$. If the probe and control fields satisfy the bare two-photon-resonance (while $\Omega_p \ll \Omega_c$), EIT conditions are fulfilled and a probe photon entering an ensemble couples to a travelling dark state polariton [64], resulting in high transmission. However, the presence of a stationary Rydberg atom in e.g. $|n'P\rangle$, shifts the states $|nD\rangle$ within the ensemble, thereby inhibiting dark state formation and leading to strong probe absorption. In this work, the probe rate is maximized while ensuring at most a single polariton is present in each ensemble, to avoid the effects associated with self-interactions [103,147].

In the experiments presented below, we load 2–5 atomic ensembles, and increase the magnetic field to 9 G in order to spectrally resolve the desired Rydberg m_J sublevel. One ensemble (the "preparation" ensemble) is used to prepare a single Rydberg atom in the state $|n'P\rangle = |75\mathrm{P}_{3/2}, m_J = 3/2\rangle$ via a three-photon transition and the Rydberg blockade mechanism [148] as illustrated in Fig. 7.1a. Although the position of the prepared Rydberg atom within the ensemble is stochastic, the width of its spatial distribution is an order of magnitude smaller than atom-polariton distances reported in this work. We employ a global probe beam counterpropagating against the control beam, and perform site-selective Rydberg preparation and detection with the control beam via a two-dimensional AOD. For the relevant distances studied in this work, we observe control beam switching times selectively illuminating ensembles of $< 10\,\mu$s, which is sufficiently small compared to the lifetimes of the Rydberg states. Thus, following the preparation of a single Rydberg atom in $|n'P\rangle$ inside a preparation ensemble, the control AOD is switched to address neighbouring ensemble(s) (the "detection" ensemble(s)) and couple them to $|nD\rangle$ Rydberg polaritons. Further information about our ensemble preparation process, Rydberg preparation and detection schemes, as well as more details about our apparatus, can be found in Appendix C.

7.3 Interaction model and regimes

The stationary Rydberg atom in $|n'P\rangle$ and the Rydberg polaritons coupled to $|nD\rangle$ interact via dipole-dipole interactions of the form $V_{PD}(r) = C_3/r^3$, where r is the atom-polariton distance and C_3 is the interaction coefficient. Simulations[53] indicate that the interactions between the two states chosen in this work are relatively isolated from other energy levels, thereby supporting interactions predominantly within this two-level manifold (see Appendix C for more information).

Depending on the distance between the stationary Rydberg atom and neighbouring Rydberg polaritons, three interaction regimes are expected: blockade, coherent exchange, and incoherent (classical) hopping. These regimes arise as a competition between polariton blockade and Rydberg exchange, both caused by the same native dipole-dipole interaction. The first regime occurs for short distances within the blockade radius $r < r_b$, which is the characteristic distance at which the dipolar coupling strength is equal to the EIT linewidth $V_{PD}(r_b) = \Gamma_{\text{EIT}}$[145,65,91]. The strong interactions in this regime prevents polariton formation within the neighbouring ensemble, resulting in strong absorption of probe photons.

As the atom-polariton distance increases, the second regime emerges, in which the dipolar interaction strength is not sufficiently large to induce blockade and polaritons will form. This regime occurs for intermediate distances $r_b < r < r_h$ where the hopping radius r_h is defined as the distance at which the interaction timescale equals the characteristic propagation timescale τ_g of a single polariton through the ensemble (i.e. group delay $\tau_g \propto \frac{OD}{\Omega_c^2}$) The hopping radius is related to the blockade radius as $r_h = \sqrt{OD_b} r_b$[145], where OD_b is the optical depth per blockade radius (in our case, $OD_b = OD$ since the ensemble is smaller than the blockade radius, and therefore $r_h > r_b$ throughout this work). In this regime, the dipolar interaction is faster than the group delay of Rydberg polaritons, which leads to coherent exchange of Rydberg excitations $|n'P\rangle \leftrightarrow |nD\rangle$ between the atom and polariton. In other words, initially-transparent Rydberg polaritons coupled $|nD\rangle$ within the ensemble evolves

into stationary $|n'P\rangle$ states which induce subsequent probe photon absorption.

Finally, at distances larger than the hopping radius $r > r_b$, incoherent hopping occurs, in which the interaction timescale is small compared to the group delay τ_g. In this case, upon the exit of the polariton from the cloud, projection measurement is performed, projecting polariton into $|n'P\rangle$ state with probability dependent on $V_{PD}(r)$ and τ_g. A classical rate equation can accurately capture the $|n'P\rangle$ probabilistic leakage into the polariton ensemble with rate $\propto \tau_g^2 \, V_{PD}^2(r)$ (see Appendix C).

7.4 Control over the Rydberg atom-polariton interaction regime

To our knowledge, Fig. 7.2 provides the first experimental observation of the transition between the different interaction regimes. The Rydberg interaction strength was varied by changing the distance between the preparation and detection ensembles (and thereby the atom-polariton separation). A control coupling of $\Omega_c/(2\pi) = 5.5$ MHz was chosen to allow for all three regimes to be accessible by our experiment. We measure the absorption of the detection ensemble and plot the contrast, defined as the ratio of detected missing photons (absorbed photons) to the number of detected photons in the absence of atoms (more information in Appendix C).

Within the blockade regime ($r < r_b$), the contrast in Fig. 7.2 is high and independent of the interaction strength, as polariton formation is blockaded due to strong dipolar interactions. Conversely, at intermediate interaction strengths ($r_b < r < r_b$), the contrast behaves non-monotonically which is indicative of coherent exchange, as $|n'P\rangle$ population hops between the preparation and detection ensemble. The minimum contrast observed within this region occurs at the distance at which, on average, a full flip-flop between $|n'P\rangle$ and $|nD\rangle$ can be completed in time equal to group delay time. At this distance, in a perfect system, polariton would exit the ensemble "unperturbed", as if it never interacted with the Rydberg atom, resulting in no contrast. We attribute the limited visibility of non-monotonic behavior to the lower OD value, positional dephasing and additional decay and decoherence mecha-

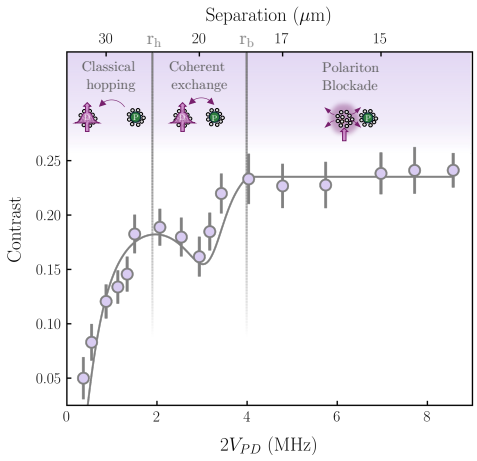


Figure 7.2: Full interaction space: Absorption through the detection ensemble hosting $|nD\rangle$ polaritons (left ensembles; shown above the plot) is plotted as a function of polariton interaction strength with a single Rydberg atom prepared in $|n'P\rangle$ within the preparation ensemble (right ensembles). The Rydberg interaction strength was varied by changing the distance between the preparation and detection ensembles. Our observations reveal three distinct regimes: blockade, coherent exchange, and incoherent hopping. Illustrations above the graph depict the behavior in each regime. The left and right vertical lines represent the interaction strengths at the hopping and blockade radius, respectively, for the control Rabi frequency of $\Omega_c/(2\pi) = 5.5\,\mathrm{MHz}$ chosen for this data. A phenomenological theory curve closely matches the observed data.

nisms in the Rydberg manifold. At larger distances ($r > r_b$), the contrast drops quadratically with the interaction strength, consistent with probabilistic (classical) hopping of the $|n'P\rangle$ population. The observed data matches well with our phenomenological theory curve (see Appendix C) as shown in Fig. 7.2), which captures all key features of our observations: the quadratic scaling in the classical hopping regime, the non-monotonic behaviour in the coherent exchange regime, and the flat contrast in the blockade regime.

We perform several additional experiments to qualitatively verify that hopping and blockade occur as expected. Since the blockade regime is a direct consequence of large interaction strengths and is frequently observed [148,144,143], we provide detailed evidence in the Appendix C that this effect occurs in the same way for spatially separated Rydberg atom and Rydberg polaritons. In the incoherent hopping regime, we present evidence for $|n'P\rangle$ state population transfer from preparation ensemble

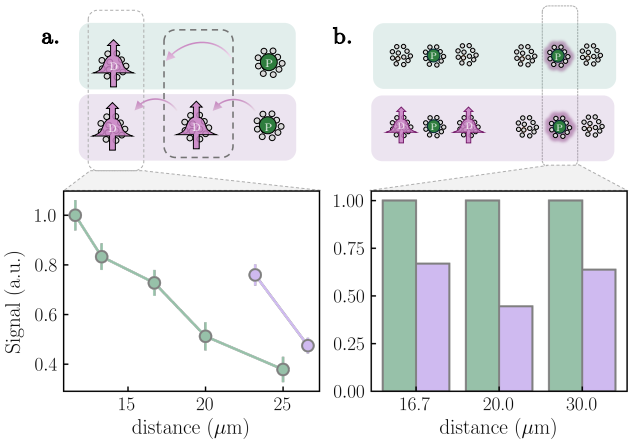


Figure 7.3: Evidence of dipolar hopping: a. Detection contrast in the leftmost detector (green markers) increases with the addition of an intermediate ensemble (purple markers), which mediates hopping between the Rydberg atom prepared in the rightmost ensemble and the leftmost detector. **b.** Initial $|n'P\rangle$ Rydberg population in the prepared middle ensemble (green) decreases following polariton propagation in the neighbouring detector ensembles (purple).

to detector ensemble through observations of increased absorption in the detection ensemble, as well as decreased absorption in the preparation ensemble. In Fig. 7.3a, we show that the contrast observed in the detection (leftmost) ensemble, following preparation of a single $|n'P\rangle$ excitation in the rightmost ensemble, increases when a "mediating" ensemble is present. The increase in signal (purple) compared to the same experiment performed without the mediator (green) indicates that the $|n'P\rangle$ state first hops to the mediating ensemble before hopping to the detection ensemble. Each process is $8\times$ faster compared to the hopping process between preparation and detection ensemble in absence of the mediating ensemble, resulting in increased probability of finding $|n'P\rangle$ in the detector ensemble. Next, we verify that the initial $|n'P\rangle$ population in the preparation ensemble has decreased due to hopping with neighbouring $|nD\rangle$ polaritons. With an array of three ensembles as shown in Fig. 7.3b, we prepare a single $|n'P\rangle$ state in the middle ensemble, and measure how this population changes by detecting that same ensemble via EIT. For various distances between preparation and detection ensembles, it is evident that the initial $|n'P\rangle$ population is reduced if $|nD\rangle$ polaritons travel through neighbouring ensembles (purple) compared to the case when they are not (green; more information

in Appendix C). These two experiments indicate that $|n'P\rangle$ population is lost from its initial host, preparation ensemble, and appearing in the detection ensemble, mediated by dipolar interactions.

7.5 Non-local Readout of a Rydberg qubit using Rydberg polaritons

After exploring the full range of interaction regimes in our system, we investigate the Rydberg EIT mechanism as a method for fast, non-destructive, and state-selective readout of a single Rydberg qubit using a neighbouring detector ensemble (i.e. "non-local" detection). Parameters for the detector were chosen by manual optimization, consisting of a higher control field ($\Omega_c/(2\pi) = 20\,\mathrm{MHz}$), an average optical density of ≈ 1.5, approximately 200 atoms per ensemble, and a qubit-detector separation of $20\,\mu$m (more details in Appendix C). At higher control fields, which are preferred as higher probe rates are possible, the blockade radius is smaller, and therefore it is impossible to operate our detector within the blockade regime, which would be ideal for detection (given our $w_0 = 4.9\,\mu$m dipole trap waist and control Rabi frequency). Instead, our optimal readout results shown in Fig. 7.4a for single-shot detection of a Rydberg qubit were achieved in the classical hopping regime. We achieved a single-shot preparation and detection fidelity of $47(5)\,\%$ for distinguishing between qubit states within $30\,\mu s$ of readout. Since the detection scheme leads to minimal atom loss within the ensemble, repeated preparation and readout sequences are possible. By performing this process with 20 repetitions of $10\,\mu s$ detection, we achieved a fidelity of $79(4)\,\%$ as shown in Fig. 7.4b. Given that our preparation method is not ideal (previous work has demonstrated $\sim 90\,\%$ fidelity [148]), the actual detection fidelity for a single shot is slightly higher, suggesting that our current repeated measurement fidelity may exceed $90\,\%$.

Using our repeated readout scheme, we demonstrate a non-local, state-selective detection of a single Rydberg qubit using a neighbouring ensemble. We apply a global $5.214\,\mathrm{GHz}$ microwave field, following selective preparation of $|n'P\rangle$ Rydberg atom just in the qubit ensemble. The microwave field

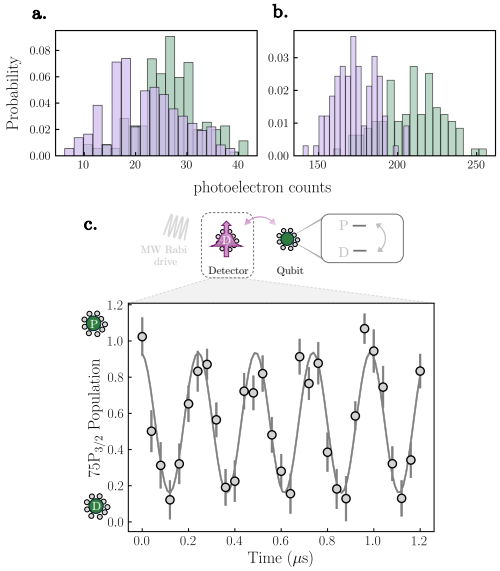


Figure 7.4: Applications of Rydberg EIT as a non-local detector: a. Single-shot historgam for 30 μs of readout. **b.** With repeated preparation and detection with 20 repetitions of $10\,\mu s$ detection, we achieve a fidelity of $79(4)\,\%$. **c.** State-selective non-local detection of a Rydberg qubit, following global microwave drive, shows long-lived coherent Rabi oscillations.

couples the $|n'P\rangle$ and $|nD\rangle$ states of the qubit ensemble, inducing Rabi oscillations between them at a frequency of $\Omega_{\mathrm{MW}}/(2\pi) = 4.04(4)\,\mathrm{MHz}$. Meanwhile, the microwave field has no effect on the detector ensemble, as all atoms are in the ground state at that time. After a variable microwave application time, we detect the transmission through the detector ensemble positioned at distance 20 μm from the qubit as shown in Fig. 7.4c, demonstrating that our detection method is state-selective, which has not been demonstrated previously in the non-local configuration.

For optimal single-shot detection of a single Rydberg atom, the atom must be placed as close as possible to the detector ensemble to remain within the blockade regime, while maintaining high control field Rabi frequencies to allow for high probe rates. In our system, this was not possible, however, we anticipate that this limitation could be addressed with the use of tightly-focused single-atom tweezers and a separate set of detector ensemble traps. This choice would additionally allow a number of other improvements expected to further enhance the signal. With these improvements, we estimate

that detection fidelities of over 99 % are possible within tens of microseconds. The detection SNR can be further improved by placing several detector ensembles within the blockade radius of the single Rydberg atom. Such detector multiplexing is not useful in the coherent exchange regime, as the total population (and thus, the total detection contrast) is conserved. Further details on optimal parameters for single-shot readout, along with data on multiplexed detection, are provided in Appendix C.

7.6 Conclusion and outlook

In summary, we investigated the full dipolar interaction regimes between a stationary Rydberg atom and travelling Rydberg polaritons, in which the interaction strength is varied via the inter-ensemble separation. We observed three distinct regimes - blockade, coherent exchange, and incoherent hopping, qualitatively verifying the expected behavior of our system for each of them. We further explore the use of this state-selective scheme for fast, non-destructive readout of single Rydberg atom, in which we demonstrate non-local detection of Rabi oscillation of a Rydberg atom via detector ensemble separated by 20 μm. Although the readout fidelity achieved in this work is not high enough to be readily used, we outline a pathway to improve it to 99 % level. With improved readout fidelity, interfacing arrays of ensemble detectors with single atom arrays has the potential to significantly enhance neutral atom quantum processors, as it may lead to orders-of-magnitude faster readout than current state-of-the-art methods, efficient mid-circuit readout via the inherent non-destructive nature of Rydberg EIT, and full compatibility with continuous array operation at a constant high magnetic field, as well as with existing architectures for neutral atom quantum processors [11,33,34,35]. Future studies may also utilize our work as a convenient infrastructure for quantum photonic networks, supporting quantum photonic gates and switches [94,95,96]; or for studies of quantum walks with inherent nonlinearity (in a similar fashion to those demonstrated in [146]), where one or many Rydberg excitations can hop within an array of ensembles.

8

High Magnetic Field Loading and Imaging of Single Atom Arrays

8.1 Introduction

Arrays of single neutral atoms excited to high-lying Rydberg states have emerged as a powerful platform for quantum technologies, enabling applications in simulation [27,5], computation [24,25,26], preci-

sion metrology[29,141,142], and sensing[149]. Such systems have demonstrated remarkable scalability, routinely featuring hundreds, and recently, thousands[30,35], of individually trapped atoms. Even at these large scales, precise control is maintained over quantum states and Rydberg interactions, resulting in high-fidelity single-qubit and two-qubit gate operations[24,25,26]. This high level of control, combined with a re-configurable architecture[31], has facilitated recent demonstrations of encoded logical qubits – a key milestone towards error-corrected logical qubits and fault-tolerant computation[11]. These developments highlight the neutral atom platform as a strong contender for quantum computer, and expanding the control of these systems remains an important goal.

Due to the hyperfine structure of commonly-used atomic species (Rb, Yb, Sr), large magnetic fields (on the order of 10-100 G) are often required for high-fidelity gate operations [150,26,34,151]. For alkaline-earth atoms with a convenient narrow-linewidth transition, single-atom loading and imaging in a magnetic field has been demonstrated[34,152]. However, for alkali atoms without such a transition, zero magnetic field is required for these processes, in particular, polarization gradient cooling (PGC), which imposes a direct limitation on the speed of the neutral atom processor since magnetic field switching for any mid-circuit measurement is necessary. This switching process usually takes $\approx 1 - 10$ ms, several orders of magnitude longer than typical qubit manipulations, thus rendering multiple mid-circuit readouts lengthy and inconvenient. Additionally, the requirement for zero-field loading and imaging prevents systems based on alkali atoms from operating in a fully continuous mode via an optical-lattice conveyor belt, a technique recently demonstrated for ^{171}Yb[34], ^{88}Sr[35]. Hence, the requirement for zero magnetic field loading and imaging directly limits the duty cycle of the alkali-atom quantum processor.

Alternative approaches to PGC for imaging and loading of single alkali atoms have been developed, including Raman (sideband) cooling[153,154], Λ-enhanced gray molasses[155,156], and EIT cooling[157], however, these experiments were performed either at low magnetic fields or required long imaging durations. Non-destructive imaging has been achieved in high magnetic fields at the cost of

significantly deeper traps [158,159], which hinders scalability of tweezer arrays. Consequently, no comprehensive solution has been demonstrated thus far to support the essential operations of loading and imaging of single alkali-atom arrays in high magnetic fields.

In this work, we demonstrate non-destructive, high-fidelity imaging of single atoms in a high magnetic field at trap depths commonly used in alkali tweezer arrays. Our technique is based on a combination of fluorescence imaging, responsible for single-atom detection, and EIT cooling on the D2 line [67,160], enabling the preservation of atoms during detection, with which we achieve $99.6(3)\,\%$ readout fidelity in 70 ms with $98.2(3)\,\%$ atom survival probability. With the same magnetic field and combination of laser beams, we show that single atoms can be prepared in an array of tweezers with a stochastic loading probability of $48(3)\,\%$, which can be enhanced to $68(2)\,\%$ by adjusting the laser detunings. In fact, our results are achieved despite the modest parameters of our microscope objective lens, where with typical objectives used in state-of-the-art atom array experiments, an order-of-magnitude speedup is readily expected. Importantly, our scheme works in 2D, cooling atoms in both the axial and radial directions, and as such it is compatible with either the constant array architecture [161] or the zoned architecture [11], making it applicable to a wide variety of experimental systems and is an important step towards continuously-operating alkali-atom arrays for quantum information applications.

8.2 Experimental setup

Our experimental setup is shown in Fig. 8.1a. An array of 10 optical tweezers ($\lambda = 808\,\text{nm}$) is generated with a spatial light modulator (SLM) focused to beam waists of $w_0 \simeq 1.6\,\mu\text{m}$ through a microscope objective lens (NA $= 0.4$) with measured radial and axial vibration frequencies of $\omega_r/(2\pi) = 45\,\text{kHz}$ and $\omega_z/(2\pi) = 4\,\text{kHz}$ and AC Stark shift of 23 MHz (see details in Appendix D). After initial magneto-optical-trap (MOT) cooling, loading, and compression stage optimized with

machine learning[48], as reported previously [162], an ensemble of ^{87}Rb atoms is loaded into each tweezer. The magnetic gradient is then switched off, while the bias field along the x direction is increased to 2.3 G for subsequent parity projection into single atoms and fluorescence imaging.

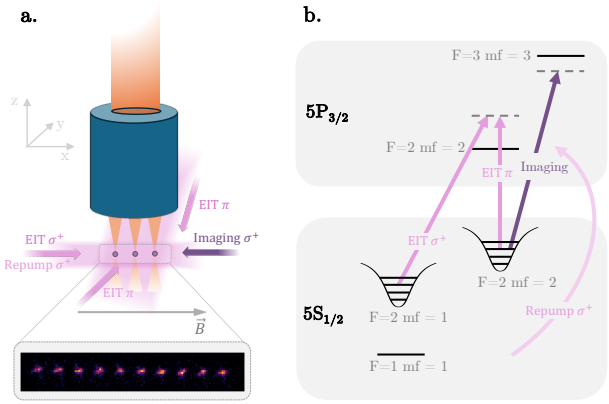


Figure 8.1: Experimental setup and relevant energy levels: a. Schematic of our experimental setup, showing 10 traps generated by an SLM focused through a microscope objective. The bias magnetic field is set to 2.3 G along the x-axis. The tweezers are illuminated with σ^+ polarized control beam used for EIT cooling, with a counterpropagating σ^+ polarized fluorescence (imaging) beam. The π polarized EIT probe light propagates in parallel with the microscope objective, entering the chamber in the $y-z$ plane at a 37° angle relative to the z-direction. A secondary π beam is aligned along the y-direction. The repump light is generated as an EOM sideband on the EIT σ^+ control beam. **b.** Energy level diagram showing the states involved in EIT cooling and the transition used for imaging.

Both operations (imaging and loading) are performed with the same beam configuration: a σ^+ polarized EIT control beam used for cooling (propagating along the magnetic field i.e. x-axis), a counterpropagating σ^+ polarized fluorescence imaging beam and π polarized EIT probe beam, aligned in the $y-z$ plane at a 37° angle relative to the z axis. An additional π beam is aligned along the y-axis, as it was found to improve our results, however, it is not strictly necessary (see Appendix D).

In Fig. 8.1b, the relevant Zeeman sublevels used for imaging and cooling are shown. The fluorescence imaging beam is -67 MHz detuned from the $|5S_{1/2}, F=2\rangle \rightarrow |5P_{3/2}, F=3\rangle$ transition, the EIT control beam is $+36$ MHz detuned from the $|5S_{1/2}, F=2\rangle \rightarrow |5P_{3/2}, F=2\rangle$ transition, and the EIT probe light frequency is tuned to compensate the Zeeman splitting in the ground

state and satisfy the EIT condition[46]. A polarized repump beam addresses the $|5S_{1/2}, F = 1\rangle \rightarrow |5P_{3/2}, F = 2\rangle$ transition, generated as a sideband on the σ^+ control beam via a phase electro-optic modulator (EOM). For more details on experimental parameters, including Rabi frequencies, and calculation showing that we work far outside Lamb-Dicke regime see Appendix D.

8.3 Results

Fig. 8.2a shows histograms of our imaging in high magnetic field for each of the 10 traps, from which we extract an average fidelity of $99.6(3)\,\%$ to distinguish a single atom from the background. During 70 ms of imaging, we detect on average $84(7)$ photoelectron counts per atom, consistent with our estimated imaging beam scattering rate (see Appendix D) combined with our estimated total collection and detection efficiency ($\approx 1\,\%$), which is predominantly limited by our microscope objective NA $= 0.4$ (collection of $3.3\,\%$) and $\sim 40\,\%$ transmission loss for our imaging wavelength of 780 nm from the same objective.

In Fig. 8.2b, we show preparation of single atoms in optical tweezers in high magnetic field, for each of the 10 traps. The histograms in purple display the photoelectron counts detected during 70 ms of imaging in high magnetic field, performed immediately after tweezers are loaded from the MOT and the magnetic field is stabilized at 2.3 G. The histograms in green show the photoelectron counts collected from the subsequent image. These measurements indicate that the initial traps are loaded with multiple atoms, but after one application of imaging, the following images display bimodal distributions – characteristic of stochastic loading of single atoms, with an average loading probability of $48(3)\,\%$, consistent with typical loading probabilities during PGC ([17,132]). Fig. 8.2c shows that the characteristic time to prepare single atoms using this imaging technique is much shorter than the imaging duration required for high-fidelity readout. We measure the characteristic collisional timescale to be 1.63 ± 0.07 ms, with single atoms prepared reliably within 10 ms.

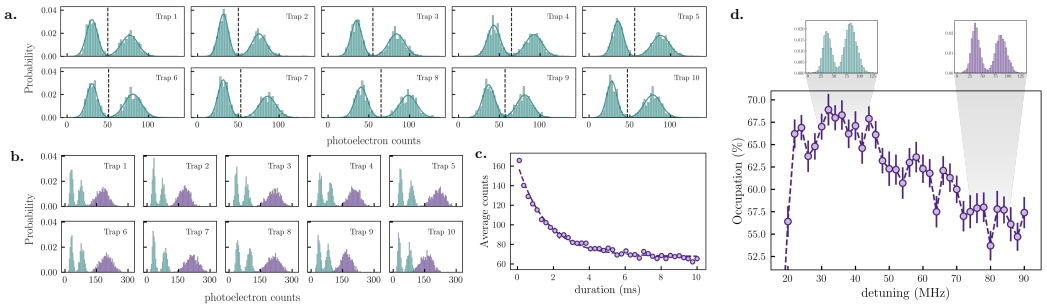


Figure 8.2: Imaging and loading in a high magnetic field: a. Histograms of high B-field imaging obtained in 70 ms for 10 different traps. **b.** Histograms of two consecutive high B-field images. The first image (purple histogram) is taken after ensembles of atoms are loaded into tweezers and magnetic field is increased to 2.3 G. The second image (green histogram) is taken immediately after the first image. A bimodal distribution of the second image confirms that this imaging method can be used to prepare single atoms in high magnetic fields with probability $48(3)\,\%$. **c.** Counts collected from EIT imaging as a function of preparation duration saturates once a single atom has been prepared in a tweezer via light-assisted collisions from EIT imaging beams. The fit reveals characteristic collision times of 1.63 ± 0.07 ms, with single atoms reliably prepared within 10 ms. **d.** Single-atom preparation probability as a function of imaging beam detuning from Stark-shifted $|5S_{1/2}, F = 2\rangle \rightarrow |5P_{3/2}, F = 3\rangle$ transition. We observe $\approx 68(2)\%$ loading probability for detunings $\lesssim 2U = 42$ MHz, as expected[45].

For our scheme, cooling beams are blue-detuned on the $|5S_{1/2}, F = 2\rangle \rightarrow |5P_{3/2}, F = 2\rangle$ transition, which enables possibilities for enhanced loading via blue-detuned light-assisted collisions[45]. In Fig. 8.2d, we show enhanced single-atom loading probabilities of up to $\approx 68(2)\,\%$ by adjusting the detuning of fluorescence imaging beam from red to blue on the $|5S_{1/2}, F = 2\rangle \rightarrow |5P_{3/2}, F = 3\rangle$ transition, observing enhancement for detunings $\lesssim 2U = 42$ MHz relative to the Stark-shifted line, as expected [45]. Moreover, the enhanced loading was achieved in an order of magnitude faster time than previous demonstrations on the D1 line[45], with the characteristic single-atom preparation timescale now observed within just $2 - 10$ ms. While Λ-enhanced grey molasses cooling has been previously demonstrated on the D2 line[163], to our knowledge, our work presents the first observation of enhanced loading of single atoms on the D2 line, which does not require the use of additional D1 lasers. A detailed investigation into fundamental limitations in deterministic loading is left for future work.

For imaging to be effective in the continuous assembly of an atomic storage array in a high magnetic field, it is essential to demonstrate that the imaging technique leads to low atom loss. In Fig. 8.3a,

we measure the rate of atom loss by taking nine successive images. The purple markers show the atom loss probability after each image, while gray markers indicate the baseline atom loss (observed by merely holding atoms in tweezers for the same duration without applying any cooling and imaging light), which indicates that the in-trap atom lifetime is the main contribution to loss. After correcting for the trap lifetime, we find that the atom loss per image is $1.8(3)\,\%$.

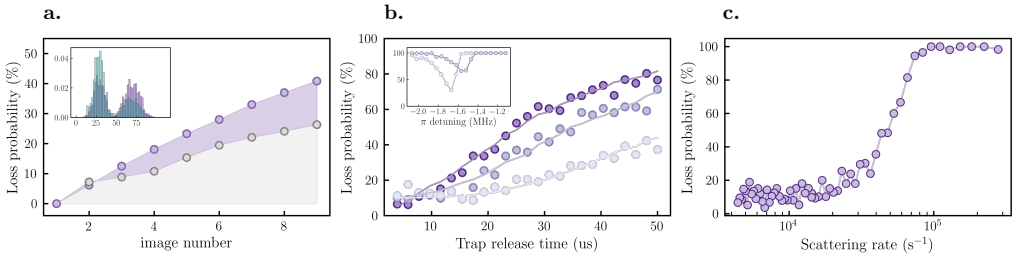


Figure 8.3: Imaging-induced atom loss and heating: a. Probability of atom loss as a function of number of consecutive 70 ms images. The purple markers show total atom loss, while the gray markers indicate in-trap atom loss in the absence of cooling and imaging beams, indicating that the in-trap atom lifetime is the main contribution to loss. The inset displays a histogram for the first (purple) and ninth (green) images of an atom in the same trap. **b.** Release and recapture measurements obtained for 3 cases: after PGC (dark purple), EIT imaging (purple), and EIT cooling (no imaging; light purple). Fitted data reveal temperatures of $T = 37^{+15}_{-8}\,\mu$K after PGC, $T = 16^{+3}_{-3}\,\mu$K after EIT imaging, and $T = 9^{+2}_{-2}\,\mu$K after EIT cooling, which indicates that the addition of a fluorescence imaging beam increases temperatures compared to EIT cooling alone. The inset displays atom loss probability as a function of probe EIT detuning and it shows the shift in optimal EIT probe beam frequency when EIT is performed with fluorescence imaging due to the AC Stark shift from the imaging beam. **c.** Atom loss probability as a function of imaging beam scattering rate, which shows a sudden increase when the scattering rate matches the radial trapping frequency. This suggests that the imaging duration is limited by the radiation pressure force from the imaging beam, which can be reduced by increasing the radial trapping frequency.

Next, we investigate the effects of our imaging, while identifying potential areas for improvement. To determine if our imaging technique, which involves fluorescence and EIT cooling, is heating atoms, we perform standard release and recapture measurements [50] for three cases: (1) atoms cooled using PGC, in zero magnetic field, (2) atoms cooled using EIT cooling in a high magnetic field, and (3) atoms after one round of imaging (i.e. EIT cooling + single fluorescence imaging beam) at high magnetic field. As shown in Fig. 8.3b, a temperature of $T = 16^{+3}_{-3}\,\mu$K is achieved after applying one imaging cycle, which is significantly colder than that achieved via PGC ($T = 37^{+15}_{-8}\,\mu$K) and slightly hotter than the EIT cooling temperature (no imaging beam) of $T = 9^{+2}_{-2}\,\mu$K (see Appendix D). This

indicates that the heating rate generated by the fluorescence imaging beam is not fully compensated by our EIT cooling, suggesting that cooling between successive imaging sessions could prevent atoms from being heated out of the traps. We note that to cool atoms effectively in the presence of the imaging beam, the probe beam frequency is redshifted by 130 ± 10 kHz compared to cooling in the absence of imaging (inset in Fig. 8.3b), which is consistent with the AC Stark shift generated by our detuned imaging beam (see Appendix D).

To investigate the speed limitation of our imaging technique, we scan the detuning of the fluorescence beam, as shown in Fig. 8.3c, which effectively changes the scattering rate (see Appendix D). We observe a sharp increase in atom loss for scattering rates above 4×10^5 s^{-1}, which is consistent with the radial trapping frequency. Further experiments show that increasing the trap depth (thereby the trapping frequency) enables higher scattering rates for a given atom loss probability. This implies that the main limitation to the scattering rate is the momentum kick exerted by fluorescence photons on the atoms. If multiple imaging photons are absorbed before the atom complete a full oscillation in the radial direction, it will be pushed out of the trap in the direction of the imaging beam. Our observations indicate that increasing the trapping frequency with tighter tweezers generated via a higher–NA objective would allow for higher scattering rates without losing atoms, thereby enabling faster imaging. Additionally, we anticipate that retroreflecting the imaging beam (and potentially the EIT control beam) should also help reduce atom loss.

Finally, to verify that our loading and imaging technique works in 2D, we block the π light along the y direction and find that the technique is also effective in two dimensions (see Appendix D for the data and details of the measurement). This measurement demonstrates that our imaging technique is compatible with continuous loading techniques via a conveyor belt, which require atom arrays to be configured in a zoned architecture.

8.4 Conclusion and outlook

In summary, we show that a combination of fluorescence imaging with EIT cooling on the D2 line enables single-atom preparation and non-destructive, high-fidelity imaging in high magnetic fields. We achieve $99.6(3)$ % readout fidelity in 70 ms of imaging with $98.2(3)$ % survival probability and single-atom preparation from an ensemble within 10 ms with $48(3)$ % stochastic loading. We demonstrate that enhanced loading is possible on the D2 line, achieving up to $68(2)$ % probability to prepare a single atom in an order of magnitude faster time compared to previously demonstrated enhanced D1 loading schemes[45]. Furthermore, we show that our loading and imaging technique can operate in two dimensions, which renders our method compatible with re-loading of atom arrays[33,34,35] and zoned architectures for neutral atom quantum processors[11]. Although our experiments are performed in a relatively small bias field of 2.3 G due to technical limitations, there is no inherent reason why this technique cannot be extended to the higher magnetic fields necessary for high-fidelity quantum gates[160].

We believe our results can be significantly improved with modest technical upgrades, in particular, an objective with a higher NA. Objectives typically used in atom-array experiments with NA $= 0.65$ would result in a fivefold increase in overall collection efficiency. Tighter tweezers ($\omega_0 \lesssim 1\,\mu$m) generated by this objective would enable a fourfold increase in trapping frequency (and correspondingly in the scattering rate) for the same trap power. Consequently, we anticipate at least an order of magnitude reduction in imaging duration, which would also decrease imaging destructiveness by the same factor. Tighter tweezers would result in higher collision rates and fewer atoms initially loaded into the traps, thereby reducing the single-atom preparation time as well. Switching EIT cooling from the D2 line to the D1 line, which has been used to achieve $\sim 90\%$ single-atom loading probability via blue-detuned light-assisted collisions in Λ-enhanced gray molasses[45], could further improve single-atom loading probability.

Our scheme is simple, applicable to a wide variety of atom arrays with various atomic species or architectures and is robust compared to other optical cooling schemes in magnetic fields (i.e., Raman sideband cooling[164]). Therefore, by implementing our method, atom arrays should be completely compatible with a constant high magnetic field, which will introduce a speedup in their operation time and is a prerequisite for their continuous operation for quantum information processing applications.

9

Conclusion and Outlook

9.1 Summary

In summary, this thesis presents two readout tools developed to enhance the performance of the neutral atom platform. The first tool is a fast, non-destructive qubit readout intended for mid-circuit measurements. This method achieves a three-orders-of-magnitude improvement in speed over conventional fluorescence readout, reducing the readout time to tens of microseconds. It utilizes tweezers

filled with ensembles of atoms to collectively readout a single Rydberg qubit via Electromagnetically Induced Transparency. We tested this approach with the Rydberg qubit placed both inside and adjacent to the ensemble detector and our study shows that detection works in both cases, with higher fidelity achieved when qubit is placed inside the ensemble. We also find that the underlying physics mechanism behind detection differs in these cases, driven by the competition between Rydberg blockade and Rydberg exchange interaction mediated by the same dipole-dipole interaction. While this method proves to be fast and non-destructive, further work is needed to improve readout fidelity, and our simulations suggest that this can be accomplished by creating a setup hosting tweezers of ensemble atoms and tweezers of single atoms. The second tool developed is a method for single atom loading and high-fidelity imaging in high magnetic fields, crucial for enabling the neutral atom platform to operate in a fully continuous manner. Combined with continuous loading techniques, this method has the potential to reduce the experimental cycle time of the neutral atom platform by several orders of magnitude. The method was successfully demonstrated in two dimensions, making it compatible with zoned architectures of neutral atom quantum computers and easily implementable in other experimental setups. Additionally, we explored the use of machine learning in our experiment, a technique that is gradually becoming more adopted in neutral atom setups. Incorporating this tool led to the accidental discovery of Bose-Einstein Condensate (BEC) formed using only polarization gradient cooling (PGC), challenging the long-held belief that PGC alone is insufficient to achieve BEC.

9.2 Outlook

This setup can be further developed towards our long-term vision of creating an efficient neutral atom quantum computing platform. Achieving this vision requires incorporating systems capable of fast mid-circuit qubit readout and a setup optimized for fast cycle times. In our envisioned system, fast mid-circuit qubit readout would be done by integrating both single atom arrays and micro-ensemble

arrays, which would function as ancilla detectors. To achieve fast cycle times, we can leverage the multi-component structure of our vacuum chamber, which includes a glass cell and a main chamber to perform continuous loading[33,34,35]. When combined with our developed technique for single atom loading and imaging in high magnetic fields, it would enable fully continuous operation of the system. Once such a system is built, it would open up opportunities to efficiently explore a wide range of analog and digital computation problems.

9.2.1 Array of micro-ensembles next to an array of single atoms for fast mid-circuit readout

As discussed in the chapter 7, and in more detail in its appendix, achieving 99 % readout fidelity in tens of microseconds requires using a larger micro-ensemble to readout a single Rydberg atom placed inside a smaller tweezer trap. Additionally, for this level of fidelity, single atom trap needs to be delivered into the micro-ensemble, enabling readout inside the ensemble, as illustrated in Figure 9.1.

To accomplish this, we must create a setup where single atoms and large atom number ensembles can coexist. Based on our experience with ensembles in the first part of this thesis and single atoms in the latter part, we now understand how to achieve this integration. The main challenge is that generating a single atom within a tweezer, which initially loads multiple atoms, requires shining fluorescence light to perform light-assisted collisions[132]. This process results in a single atom in very tight traps, while the larger traps used for ensembles, are left with no atoms. Hence, in order to have single atoms and large atom number ensembles coexist, the fluorescence light needs to be selectively applied only to single atoms. By implementing a zoned architecture[11], where ensemble traps are held in the readout zone and single atoms are delivered from either the storage or entangling zone to the ensembles only for the readout, this issue can be alleviated. Then, the fluorescence beam can only be used to illuminate the storage zone for single atom preparation, leaving the readout zone untouched.

An additional advantage of creating a hybrid setup containing both ensemble and single atom

tweezers is that ensemble tweezers can be used to prepare single atoms in a faster way and with larger loading probability than typical 50 % single-atom loading. This could be achieved by first preparing single Rydberg atom within the ensemble in several microsecond time as done in Chapters 5 and 7. Next, as Rydberg atoms are generally anti-trapped by optical dipole traps trapping ground state atoms [165], ground state atoms can be moved away from the Rydberg atom within ten microseconds with a tweezer formed by an AOD. This can be followed by de-excitation of the Rydberg atom into the ground state and turning on another set of narrow-waist tweezers to hold this single de-excited atom. This approach would enable the selective creation of single atoms from tweezers initially loaded with multiple atoms, with the loading efficiency equaling the combined fidelity of preparing a single Rydberg atom within the ensemble and its de-excitation. This fidelity could reach up to 95 % and be achieved within just a few tens of microseconds. Illustration of this idea is presented in Figure 9.1.

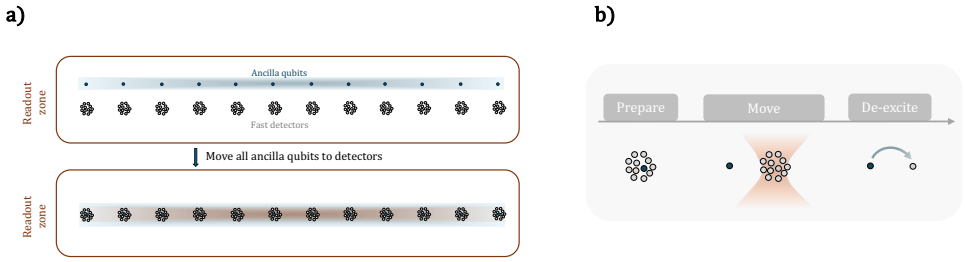


Figure 9.1: Vision of a hybrid setup containing arrays of single atoms and ensembles a. Ensemble atoms can coexist with single atom arrays by implementing a zoned architecture. Ensemble atoms are held in the readout zone, while single atoms are prepared in the storage zone, by selectively illuminating them with fluorescence beams without affecting the ensembles in the readout zone. Single atoms can then be delivered to the ensemble atoms for readout. **b.** Illustration of the idea of using ensemble atoms in combination with Rydberg preparation method developed in this thesis to prepare single atom inside the tweezer in shorter amount of time and potentially higher single-atom loading probability.

9.2.2 Fast cycle time setup

To create an efficient quantum computing platform, we need to decrease the main source of long cycle times which is the single atom loading and resorting into fully filled arrays of tweezers. The solution to

this problem can be accomplished by operating neutral atom platforms in a fully continuous way by combining loading and single atom imaging in high magnetic fields, as we demonstrated in chapter 8, with continuous loading technique via conveyor belt as demonstrated recently in [33,34,35].

An essential component for implementing a continuous loading scheme is a two-part chamber design with independent laser and magnetic field control in each section. One part of the chamber would maintain a constant magnetic field gradient necessary for creating a Magneto-Optical Trap (MOT) and initially loading the conveyor belt. The second part of the chamber, science chamber, would maintain a constant magnetic field without a gradient, which is necessary for quantum computation. Atoms would be transported from the MOT chamber to the science chamber, where computation would happen, via a lattice conveyor belt.

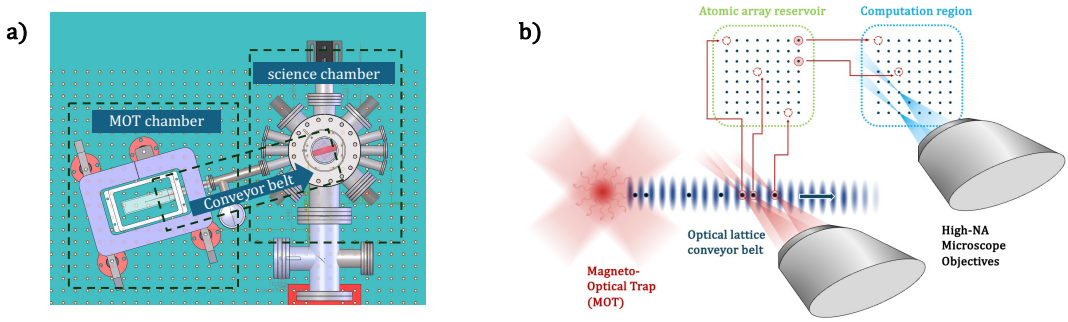


Figure 9.2: Vision of continuous loading in our setup a. Current design of our vacuum chamber, where glass cell would be used as a chamber continuously producing 3D MOT, while the steel-chamber would be used as a science chamber for quantum computation. **b.** Illustration of continuous loading, where atoms are transported from the MOT to the science chamber via a conveyor belt. In our setup, another lattice intersects with this conveyor belt. Atoms are extracted from this lattice using moving tweezers and placed inside the atomic array reservoir, forming a storage zone.

During the upgrade of our experiment, when we opened the vacuum chamber, we added a glass cell to the main chamber. Initially, this addition aimed to resolve issues in generating the MOT as described in section 2.2. However, even if the MOT worked without this component, we anticipated that adding a glass cell would anyways be beneficial in reducing cycle times for these experiments. Consequently, our current chamber design naturally accommodates the implementation of continuous

loading, as illustrated in Figure 9.2a.

To perform continuous loading in our chamber, we planned the following steps. First, the MOT chamber, glass cell in our case, will maintain a constant magnetic gradient field to continuously produce a 3D MOT. Atoms from the center of the glass cell would be transported to the science chamber, located 36 cm away, using a lattice beam with a waist of approximately $300 - 400\,\mu$m. This beam has a sufficiently large Rayleigh range to cover the distance between the chambers. The lattice would span approximately $600 - 800\,\mu$m of the microscope's field of view, which is significant given that typical fields of view for large numerical aperture microscopes are about 1 mm. To optimize for the microscope field of view, the large lattice would need to be tilted to avoid covering the entire field of view. We would intersect this large lattice with a smaller lattice (waist $20 - 30\,\mu$m) sent through one of the ports in the $x - y$ plane of the science chamber, falling within the microscope's field of view. This way, atoms will first be transported from the MOT chamber to the small lattice using the large conveyor belt. The small lattice will then deliver atoms to the microscope's field of view, where they can be extracted from the lattice into the storage area using AOD tweezers, as illustrated in Figure 9.2b.

A

Supplement for chapter 5

A.1 Experimental setup

^{87}Rb atoms are collected in a three-dimensional magneto-optical trap (MOT) and loaded into a crossed optical dipole trap created with two orthogonal far-detuned laser beams at wavelengths 852 nm (propagating along z) and 1064 nm (propagating along y) with waist sizes 10 μm and 20 μm, respectively, providing individual trap depths of typically $U_{852}/h = 2$ MHz and $U_{1064}/h = 20$ MHz. The

trap vibration frequencies are $\omega_x/(2\pi) = 5.7$ kHz, $\omega_y/(2\pi) = 3.0$ kHz and $\omega_z/(2\pi) = 4.8$ kHz. The probe propagates in the *xy* plane at an angle of 16° to the *y* axis. The cloud is cooled to $80\mu K$ using polarization gradient cooling, resulting in root-mean-squared (RMS) sizes of $x_0 = 2.4\,\mu$m, $y_0 = 4.6\,\mu$m, $z_0 = 2.9\,\mu$m for the ensemble. The rms distance between two atoms in the ensemble is then $d_0 = \sqrt{2(x_0^2 + y_0^2 + z_0^2)} = 8.4\,\mu$m. The total absorption on the $|5S_{1/2}, F = 2, m_F = 2\rangle \rightarrow |5P_{3/2}, F = 3, m_F = 3\rangle$ transition corresponds to $N_0 = 440$ atoms if we assume that the atomic cross section is reduced by various broadening mechanisms by a factor of 2 from its maximum value $\sigma_0 = 3\lambda_0^2/(2\pi)$, where $\lambda_0 = 780$ nm is the wavelength of the probe transition. We apply a magnetic field of 9 G along the direction of propagation of the probe beam to define the quantization axis and split the magnetic sublevels of the Rydberg states. The optical dipole traps are turned off during state preparation, rotation, and detection to prevent broadening of the transition due to inhomogeneous light shifts of the ground and Rydberg states.

A.2 Preparation of an atom in the Rydberg state

The preparation of the atom in the Rydberg state $|\uparrow\rangle \equiv |91P_{3/2}, m_j = 3/2\rangle$ is performed with a three-photon STIRAP-like process as described in the main text. The detuned microwave field mixes a small component of $|r\rangle$ into $|r'\rangle$, and the ramping of the two optical fields allows an adiabatic passage towards the target dressed state. To optimize the state initialization stage, we fix the frequencies of the probe and control laser beams, and scan the microwave frequency. Fig. A.1a displays the transmission of probe light during the detection stage as a function of the microwave frequency used for state preparation. We choose $f_p = 4916.1$ MHz that maximizes the preparation probability.

The Rydberg blockade effect is essential for limiting the Rydberg excitation to one atom inside the ensemble. Since the blockade radius is proportional to $\Omega_c^{-1/3}$, the probability to have more than one excitation inside the ensemble will increase if the control Rabi frequency Ω_c is too high. We optimize

Ω_c by monitoring the transmission of the probe light during the detection stage (Fig. A.1b), and choose the value $\Omega_c = 2\pi \times 2.4$ MHz that corresponds to the onset of saturation. In the future, we can further improve the preparation fidelity by a modified preparation scheme, where we ramp down the microwave power at the end of the preparation process, to avoid a small possibility of projecting the state onto $|r\rangle$ due to the sudden turn-off.

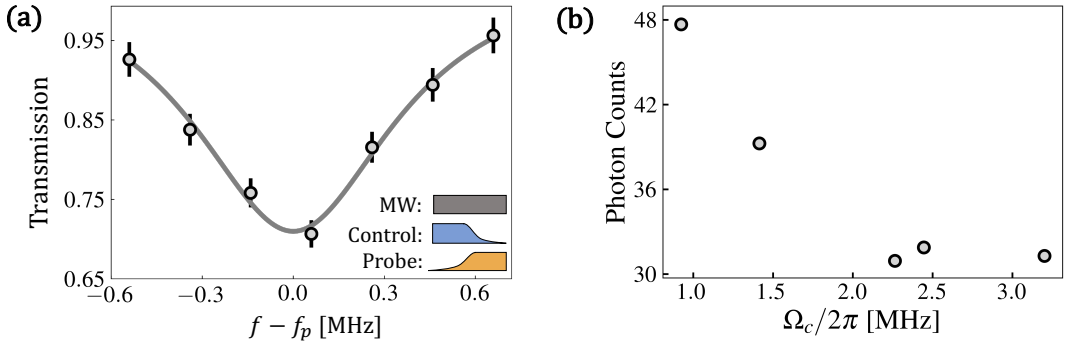


Figure A.1: Optimization of Rydberg Preparation : (a) Spectrum of the 3-photon resonance absorption to the $|\uparrow\rangle$ state vs. microwave frequency relative to $f_p = 4916.1$ MHz. Atoms are prepared in the Rydberg state $|\uparrow\rangle$ by means of a three-photon STIRAP-like process. (b) Photon counts integrated over a 10 μs window in detection stage as a function of Ω_c, the coupling of the $|e\rangle \rightarrow |\downarrow\rangle$ transition during the preparation stage. For small Ω_c, the low coupling rate leads to a small population in the Rydberg state. As Ω_c increases, the average preparation to $|\uparrow\rangle$ increases as well. Once the whole ensemble is blockaded photon counts reduce by 34%. To avoid multiple excitations, We choose to work with $\Omega_c = 2\pi \times 2.4$ MHz, the value of which corresponds to the beginning of the saturated transmission level.

A.3 Loss of the Rydberg atom and creation of Rydberg impurity during detection

As shown in Fig. 2(b) in the main text, the rising slope of the transmission during detection suggests a non-zero loss rate for the $|r'\rangle$ atom inside the ensemble. To obtain insight into the loss mechanism, we compare three different experimental sequences: (1) keeping both the probe and control light beams on for $\sim$ 30 μs (green curve in Fig. S2), (2) turning on the control light 20 μs earlier than the probe light (purple curve), and (3) turning both control and probe light on at the same time, but 20 μs later

than in case (1) (tan curve).

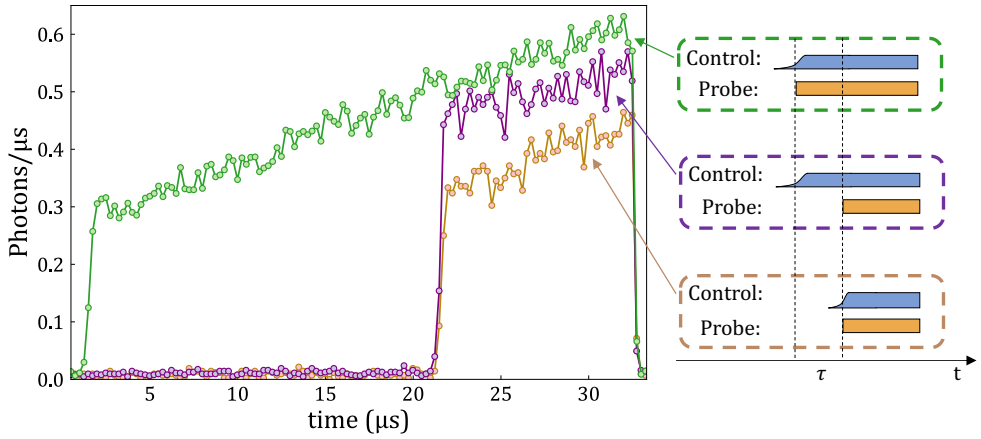


Figure A.2: Three different experiment sequences, as illustrated by the schematic figures on the right, are used to investigate the mechanisms for the loss of $|r'\rangle$ during the detection stage. Green points represent the data where both control and probe light are turned on for 35 μs, purple points represent the data when control light was on for the entire 35 μs and probe light is turned on only for the last 15us. Tan points represent the data when both control and probe light are turned on only for the last 15 μs. From the photon rate level of each sequence we can conclude that control light has the most effect in increasing the loss of the $|r'\rangle$ state, and hence the transmission over time.

For sequences (1) and (3), the photon transmission levels at the time when the probe is turned on are approximately the same. This excludes the possibility that the loss of $|r'\rangle$ is due to the expansion of the gas or to other environment noise during the detection stage. On the other hand, there is a significant difference between the data for sequences (2) and (3). The larger loss for situation (2) indicates that the control light beam induces loss of $|r'\rangle$, possibly due to coupling of the Rydberg state to the unstable $5P_{3/2}$ state, as explained in the main text. However, there is some remaining difference between the transmission for sequences (1) and (2), which suggests a smaller additional loss during detection that requires both the control and the probe light to be applied. The extra loss mechanism may be related to the autoionization process that can occur when the Rydberg polariton with Rydberg excitation component in $|r\rangle$ collides with the Rydberg atom in $|r'\rangle$ [166,167,168,169].

We have verified that photoionization rate from the control beam is too small. According to

Ref. [100], the expected photoionization rate under our conditions is $\Gamma_{pi} \approx 340\ \mathrm{s}^{-1}$, two orders of magnitude smaller that the observed rate constant $\Gamma_{tr} = 3.5 \times 10^4\ \mathrm{s}^{-1}$ for the transmission curve. Furthermore, the repulsive ponderomotive potential of the control beam is too small by three orders of magnitude to explain the increase in transmission with time. On the other hand, a dc electric field of 20-40 mV/cm could provide enough admixture of the 92S Rydberg state to the 91P state so that the state can be coupled with the control laser to $5P_{3/2}$, from where it decays to the ground state.

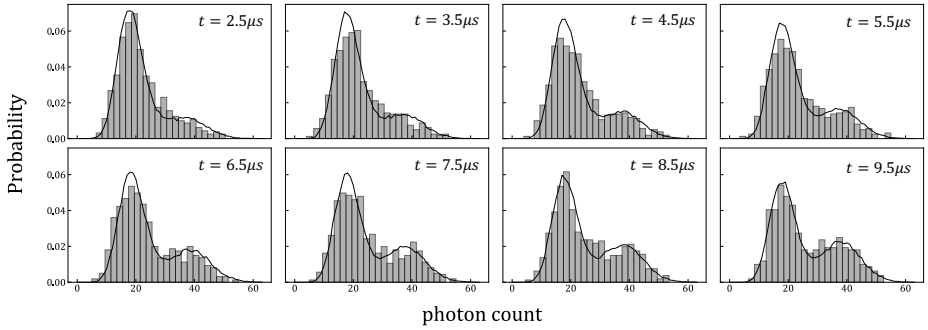


Figure A.3: Measured distributions at varying start times of probing window with an integration time of 6 μs. These distributions are fit using our theoretical model to obtain loss rate and preparation fidelity. The inferred preparation fidelity is $F_p = 0.93 \pm 0.02$

We model the loss of the Rydberg atom in $|r'\rangle$ during detection as a sudden change in the transmission. We assume that this occurs randomly with constant probability. We then use this model to predict the expected histogram of probe photon counts at various detection times and compare it to the experimental data (Fig. A.3). Our model has four free parameters: the photon rates in the presence and absence of an atom in $|r'\rangle$, respectively, the loss rate for the state $|r'\rangle$, and the fidelity of initially preparing the atom in $|r'\rangle$. We fit the experimental data for various detection times, as shown in Fig. A.3, and find a loss rate constant of $\Gamma_{tr} = 0.035\ \mu\mathrm{s}^{-1}$, and a preparation fidelity of $F_p = 0.93 \pm 0.02$. The model also captures the average rise in transmission that we observe, as shown in Fig. 2(b) of the main text.

We use a similar model to fit the photon histogram for no atom initially prepared in the Rydberg state, where we assume that a Rydberg impurity is created at random times due to the decay of the Rydberg polariton during detection. This process manifests itself as a sudden increase in probe transmission. We fit the histogram and the average transmission to find a Rydberg impurity creation rate of 0.015 μs^{-1}.

The creation of the Rydberg impurity, combined with the self-blockade effect, limits the maximum probe photon rate. While a higher photon rate is preferred for faster detection, the fidelity eventually reduces as the probe photon rate increases. Fig. S4 plots the detection fidelity at various photon rates. We choose a photon rate of 8 μs^{-1} for the measurements shown in the main text.

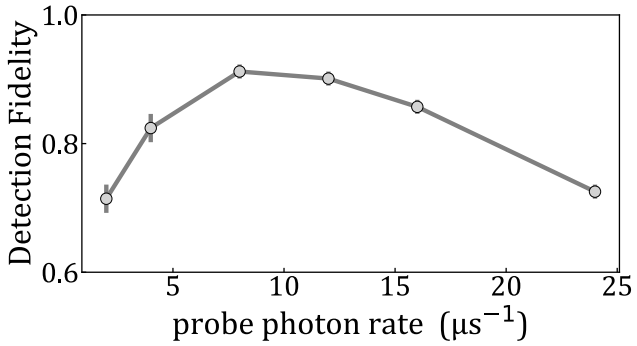


Figure A.4: Fidelity of detection as a function of the detected probe photon count rate with optimized readout time for each data point (between 3 μs and 8 μs). The data have been corrected for the preparation fidelity.

A.4 Repeated (non-destructive) detection

In the main text we provided our readout fidelity of $F_d = 0.92 \pm 0.04$ in a 6 μs readout window, and for 30 counts as a detection threshold. If we perform subsequently a second measurement in 6 μs with the same threshold, we find for this window a detection fidelity of 0.81 ± 0.04 ($\approx F_d^2$). Fig. 2c of the main text shows the correlations between the two measurements; the results are summarized in Table I. This correlation between consecutive measurements is a signature of quantum nondemolition

measurements (QND) ([170], [171]), and under ideal conditions we would not expect the measurement to induce any change in the state. The average conditional probability that the second measurement yields the same result as the first measurement is 0.79 ± 0.03.

Measurement	Prepare $\|\uparrow\rangle$		No $\|\uparrow\rangle$ preparation	
	Detect $\|\uparrow\rangle$	No $\|\uparrow\rangle$ detection	Detect $\|\uparrow\rangle$	No $\|\uparrow\rangle$ detection
first	0.92	0.08	0.10	0.90
second	0.76	0.24	0.19	0.81

Table A.1: Results for repeated (non-destructive) measurement. $|\uparrow\rangle$ preparation and detection refer to the preparation of an atom in the Rydberg state $|91P_{3/2}, m_j = 1/2\rangle = |r'\rangle$. Both the first and second measurements last for 6 μs. The error (standard deviation) for each element in the table is 0.04.

A.5 Measurements of Rabi oscillations

We use specific magnetic sublevels $|r'\rangle = |91P_{3/2}, m_J = 3/2\rangle$ and $|r\rangle = |92S_{1/2}, m_J = 1/2\rangle$ to define our qubit. However, there is also the possibility of off-resonant coupling to other magnetic sublevels, especially at high Rabi frequency. We apply a magnetic field of 9 G to lift the Zeeman degeneracy, which results in a Zeeman splitting between neighboring magnetic sublevels of $\sim$ 17 MHz for the $|91P_{3/2}\rangle$ manifold, and $\sim$ 25 MHz for the $|92S_{1/2}\rangle$ manifold. To reduce the coupling to other transitions by the the microwave field, we use two radio frequency antennas whose relative amplitude and phase are tuned to suppress the π-polarized transition $|92S_{1/2}, m_J = 1/2\rangle \leftrightarrow |91P_{3/2}, m_J = 1/2\rangle$. We observe a suppression by a factor of 10 compared to a single antenna. In the future, a third microwave antenna can be added to also eliminate the σ^- transition.

The normalized population of $|r'\rangle$ shown in the Rabi oscillation measurements (Fig. 3 in the main text) is corrected by the preparation infidelity $(1 - F_p)$ and the detection infidelity $(1 - F_d)$. The measured probability $\tilde{p}(r')$ of detecting $|r'\rangle$ is related to the actual probability $p(r')$ by the following relation: $\tilde{p}(r') = F_p[(1 - F_d) + (2F_d - 1)p(r')]$, which is used to remove the preparation and readout error. Moreover, during the 2-hour measurements of the Rabi oscillations, there were drifts

in alignments, which affected the averaged transmitted probe photon number. To account for such long-time drift, we added two extra reference measurements: one without microwave driving field, and another one without preparation stage. These two measurements allow us to monitor any slow drift of F_p and F_d, and re-scale the observed state probabilities.

A.6 Rydberg blockade

Preparation blockade: During our preparation stage, we couple atoms to the $|r'\rangle$ state. A pair of atoms in this state will experience an anisotropic van der Waals interaction $V_{r'r'} = C_6(\theta)/|R|^6$, where R is the distance between the pair of atoms and θ is the angle the between the pair of atoms and the quantization axis (Fig. A.5a). From this interaction we can estimate the effective blockade radius $V_{r'r'}(r_B(\theta)) = \hbar\Gamma_3/2$ where Γ_3 is the full width half maximum of our 3-photon resonance, $\Gamma_3 = 2\pi \times 0.6$ MHz. We estimate a blockade radius of about 12 μm along the quantization direction ($\theta = 0$). The resulting blockade volume has an ellipsoid shape with an aspect ratio of 1.6, as shown on Fig. A.5b. The average blockade radius of the ellipsoid is $r_B = 15\,\mu$m.

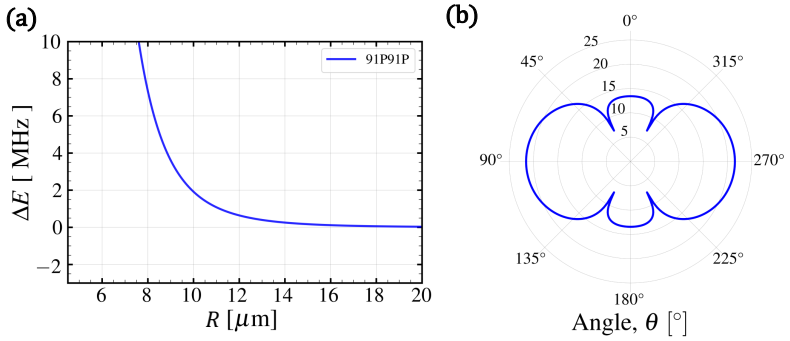


Figure A.5: Rydberg blockade during preparation: (a) Interaction energy ΔE between two atoms in state $|r'\rangle$ as a function of separation R at $\theta = 0$ calculated from exact diagonalization of the interaction Hamiltonian. The fitted van der Waals interaction coefficient is $C_6\,(\theta = 0) = 2\pi \times 1.94$ THz $\cdot\ \mu$m^6, which results in a blockade radius of $r_B\,(\theta = 0) = 12\ \mu$m. (b) $r_B\,(\theta)$ vs. θ. Due to the anisotropy of the atomic wave-functions involved, the resulting interaction resembles an ellipsoid with aspect ratio of 1.6, with the semi-major axis at $90 from our quantization axis. This curve was obtained by perturbatively calculating $C_6(\theta)$.

Detection blockade: During the detection stage, we couple our ground state atoms to the $|r\rangle$ state. Since r and r' have different parity they are dominated at large distances by dipole-dipole interactions ($\sim R^{-3}$), while at small distances are dominated by van der Waals interactions ($\sim R^{-6}$). The dipole-dipole interaction induces the formation of symmetric and anti-symmetric molecular states ($|\pm\rangle = |rr'\rangle \pm |r'r\rangle / \sqrt{2}$). The blockade radius during the detection stage is defined as $V_{\pm}(r_{B\pm}) = \hbar\Gamma_{EIT}/2$, with Γ_{EIT} being the EIT linewidth. The estimated blockade radius for each branch are $r_{B+} = 12.7\,\mu$m and $r_{B-} = 6.2\,\mu$m respectively. The estimated blockaded radius is therefore the average radius from both branches $r_B = 9.4\,\mu$m.

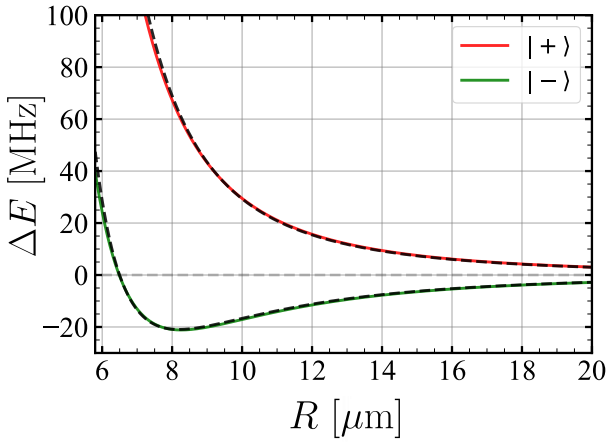


Figure A.6: Rydberg blockade for $|rr'\rangle$ during detection: (a) $|rr'\rangle$ pair state interaction energy ΔE vs. separation R at $\theta = 0$ calculated from exact diagonalization of the interaction Hamiltonian. The dipole-dipole interaction induces the formation of symmetric (red) and anti-symmetric (green) states $|\pm\rangle = (|rr'\rangle \pm |r'r\rangle)/\sqrt{2}$. Black dashed lines correspond to the fitted model $A/R^6 \pm B/R^3$, where the fit gives $A = C_6/h = 6310$ GHz $\cdot\,\mu$m^6 and $B = C_3/h = 23.6$ GHz $\cdot\,\mu$m^3.

B

Supplement for chapter 6

B.1 Gallery of observed BECs

Formation of BEC is observed in various trap configurations, as shown in Fig. B.1.The second absorption image shows a cloud with $N_{\mathrm{BEC}}/N_{\mathrm{Total}} = 11\%$, which is the largest condensate fraction observed in this work. Note that all figures in chapter 6 and here show different datasets taken over the span of several months.

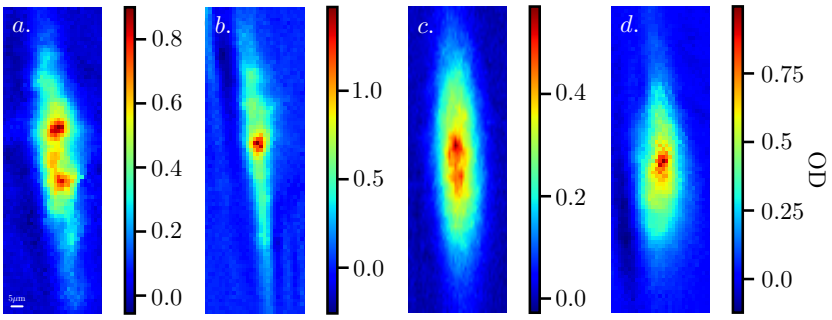


Figure B.1: Gallery of BECs. BEC formation is observed in a: **a.** Misaligned dipole trap with Gaussian beam waist $w_0 = 3.5\,\mu$m (no SLM) after $50\,\mu$s TOF. **b.** Misaligned dipole trap shown in-situ with the trapping beam slightly clipped on the SLM aperture[a]. **c.** Well-aligned dipole trap with a speckle-like phase pattern imprinted on the trapping light using an SLM (see main text for details) after $100\,\mu$s TOF. **d.** Well-aligned trapping potential generated by interfering two traps with waist $\omega_0 = 2\,\mu$m separated by $3.5\,\mu$m after $20\,\mu$s TOF[b].

[a] The trapping light consists of a Gaussian beam with $1/e^2$ diameter $2\omega_0 = 12.5$ mm incident on an SLM with aperture size $12.8\,\text{mm} \times 15.9\,\text{mm}$. Without accounting for effects of clipping the beam, the Gaussian trap waist at the atom plane is $\omega_0 = 2.5\,\mu$m. SLM model number: Hamamatsu x13138-02.

[b] The two traps are generated by the SLM in which the difference between blazing angles of the phase pattern maps onto the desired separation on the atom plane.

B.2 Machine Learning Optimization

To maximize the number of atoms loaded into the dipole trap, we use the neural network learner included in the M-LOOP package, which works well for a large number of variables in parameter spaces with many local minima. The neural network learner is comprised of three randomly initialized neural networks, each with 5 hidden layers of 64 neurons. These neural networks, in conjunction with a differential evolution algorithm, learn to map the input parameters to the output cost as summarized in previous works[48,172,120].

We choose 27 input parameters for our optimization sequence, consisting of MOT and repumper laser intensities and frequencies, bias magnetic fields along x, y, z, and magnetic field gradient. The laser intensities and bias magnetic fields are split into three time intervals, and they are linearly ramped between the chosen values as determined by the algorithm (15 parameters). Due to technical constraints on the laser detunings, the frequencies are jumped discretely without ramping; therefore, we

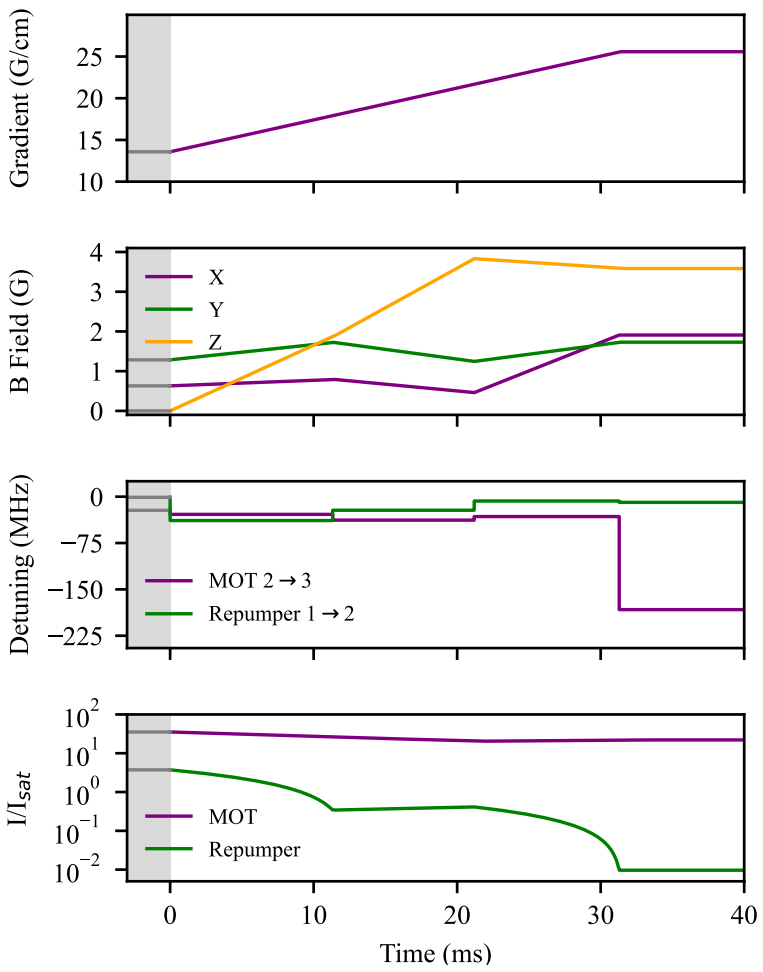


Figure B.2: Optimized control parameters determined by M-LOOP. The initial values shown in the gray shaded region were set by hand (carried over from the prior MOT loading sequence), whereas the colored lines show the values chosen by M-LOOP during the MOT compression sequence. The 27 parameters were allowed to vary independently to minimize the cost function $\mathcal{C} \equiv -N$, where N is the fitted atom number. Parameters were ramped linearly over three fixed time steps (excluding the detunings). The intensities shown are the sums over all MOT (repumper) beams, where we use $I_{sat} = 1.67$ mW/cm^2 (Clebsch-gordan for stretch transition).

include an extra parameter for each laser detuning at the beginning of the sequence (8 parameters). The detunings are defined with respect to the $|5S_{1/2}, F = 2\rangle \rightarrow |5P_{3/2}, F = 3\rangle$ transition for the MOT laser, and the $|5S_{1/2}, F = 1\rangle \rightarrow |5P_{3/2}, F = 2\rangle$ transition for the repumper laser. We include only a single parameter across the sequence for the quadrupole gradient coil (since the relaxation time of Eddy currents is expected to be comparable to the sequence length), which decreases the complexity of the input parameter space (1 parameter). Finally, we allow the length of each time bin to vary (3 parameters) such that the total duration of the sequence is fixed (40 ms). See Fig. B.2 for the optimized control parameters.

The M-LOOP package allows the outputs of the learner to be constrained for sparse parameter spaces (or spaces where the signal-to-noise ratio is too low to reliably compute the cost), through the use of a trust region. This feature prevents any parameter from changing by more than a specified fractional amount from the current best value during each new prediction. We choose a trust region of 0.2. Implementation of this feature played a critical role in fast convergence of the algorithm to the optimal parameter, due to the narrow range of parameters that ensures a reasonable number of atoms remain in the trap at the end of the sequence.

For our cost function $\mathcal{C}$, we choose to maximize the number of atoms loaded in the dipole trap, which is obtained from absorption images of the optical depth. Specifically, we choose $\mathcal{C} \equiv -N$, where N is the fitted atom number. We assume a single run of the experiment successfully loads atoms if the fit parameters of the atom cloud are realistic (i.e. the vertical RMS size is within $15 - 40\,\mu$m, the horizontal RMS size is $< 8\,\mu$m); otherwise, we assume the fit has failed and we set the cost function to zero to penalize the run. The atom number as a function of run number is shown in Fig. B.3 for a typical optimization routine.

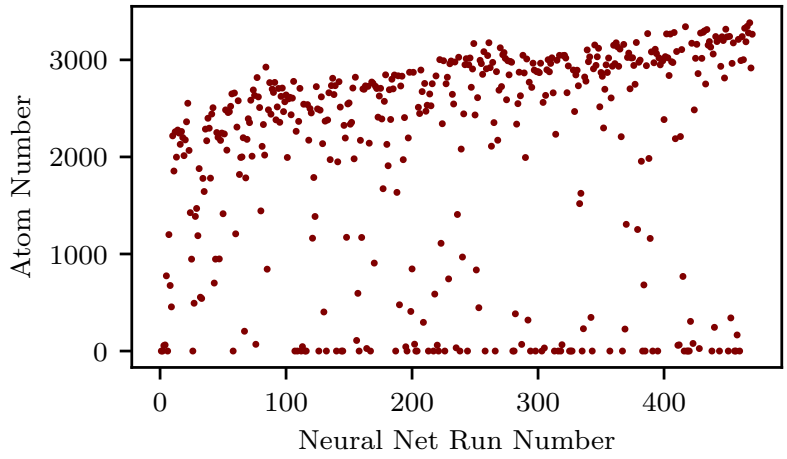


Figure B.3: The atom number increases with run number of the neural network learner, implying that the algorithm is learning the parameters that maximize the atom number (or minimize the cost). The atom number is set to zero when the fitted parameters of the atom cloud are unrealistic.

B.3 Definition of classical phase space density

The classical phase space density of the thermal cloud is given by:

$$\mathrm{PSD} = \frac{1}{3} N_{\mathrm{total}} \frac{\hbar^3 \omega_r^2 \omega_z}{(k_B T)^3} \tag{B.1}$$

where N_{total} is the total number of atoms in the dipole trap, T is the fitted temperature of the thermal cloud obtained from TOF imaging, and ω_r and ω_z are the radial and axial vibration frequencies, respectively. The factor of $1/3$ accounts for the three Zeeman sublevels of the $F = 1$ ground state manifold.

B.4 Hyperfine states of atoms

The optimized algorithm prepares the atoms predominantly in the $F = 1$ hyperfine manifold by its choice of laser powers and detunings. During the final time-bin, the ratio of scattering rates from the MOT laser with respect to the repumper laser (and hence the population ratio in $F = 1$ with respect to $F = 2$ of the ground state manifold) is calculated as:

$$\begin{aligned}\frac{P(F=1)}{P(F=2)} &= \frac{I_{\mathrm{MOT}}}{I_{\mathrm{Repump}}}\left(\frac{\Delta_{\mathrm{Repump}}}{\Delta_{\mathrm{MOT}}}\right)^2 \\ &= \frac{22}{9.7\times10^{-3}}\left(\frac{-9\,\mathrm{MHz}}{84\,\mathrm{MHz}}\right)^2 \\ &= 27, \end{aligned} \tag{B.2}$$

which confirms that $\sim 97\%$ of the atoms are in the $F = 1$ hyperfine manifold of the ground state at the end of the optimized cooling sequence.

B.5 Dipole trap extinction measurements

To ensure that the BEC is fully released during TOF, we checked the extinction of the dipole trap power when monitored on a photodiode. In sequence, the extinction is estimated to be $> 1.7\times10^3$, limited by the resolution of the oscilloscope used to measure the photodiode voltage. For a typical trap depth of $\sim 8\,\mathrm{MHz}$, this suggests a residual trap depth of $< 4.7\,\mathrm{kHz}$ during TOF, or $< 0.2\,\mu\mathrm{K}$, which is insufficient to confine the BEC along the radial direction.

B.6 Three-body loss in TOF

The observed condensate expansion energies and atom number imply that the condensate is in the Thomas-Fermi (TF) regime, where the release energy per particle ε_r is dominated by the interaction energy, such that $\varepsilon_r = 2\mu/7$, where μ is the chemical potential [173]. Our measurements yield $\mu/h = 98(14)$ kHz. From this we can obtain the peak density in the TF regime, $n_{TF} = \mu/g$, as well as the geometric mean of the local trap frequencies $\bar{\omega}$, using $\mu = \hbar\bar{\omega}\left(15Na/\bar{a}\right)^{2/5}$, where $\bar{a} = \sqrt{\hbar/(m\bar{\omega})}$, $N = 250$ is the atom number in the condensate, $a = 5$ nm the scattering length, and $g = 4\pi\hbar^2 a/m$. We obtain $n_{TF} = 1.4(4) \times 10^{16}\text{cm}^{-3}$ for the peak condensate density and $\bar{\omega}/(2\pi) = 21(6)$ kHz for the local trap frequency.

To verify the three-body loss hypothesis, we use the measured condensate release energy per particle $\varepsilon_r/h = 28$ kHz to calculate the chemical potential $\mu = (7/2)\varepsilon_r$ and atomic density [173]. Under the Thomas-Fermi approximation, we have for the peak density $n_{TF} = \mu/g$, where $g = 4\pi\hbar^2 a/m$, with $a = 100a_0$ being the ^{87}Rb scattering length, a_0 the Bohr radius, and m the atomic mass. We find $n_{\text{TF}} = 1.4 \times 10^{16}\,\text{cm}^{-3}$, corresponding to a three-body loss rate $\Gamma_3 = K_3\, n_{\text{TF}}^2 = 8(3) \times 10^3\,\text{s}^{-1}$. Here, we have used the loss coefficient $K_3 = 4(2) \times 10^{-29}\,\text{cm}^6\text{s}^{-1}$ for distinguishable atoms, assuming that condensates are formed in all three magnetic sublevels of the $F = 1$ manifold. The calculated loss rate is consistent with the observed loss rate $\Gamma_{\text{obs}} = 4.3(3) \times 10^3\,\text{s}^{-1}$ for the condensate during TOF. However, as discussed in the main text, the persistence of the condensate and thermal cloud in-trap for hundreds of milliseconds suggests we are overestimating the density in the condensate, and the most likely explanation for the loss of condensate atoms during TOF, as shown in Fig. 6.3c, are elastic two-body collisions. For the thermal cloud, the estimated two-body collision rate is $\Gamma_{2,\text{th}} = 2.2 \times 10^3\,\text{s}^{-1}$. From the condensate fraction and volume ratio V_d/V, we can estimate the condensate density $n_{\text{BEC}} \approx 8 \times 10^{15}\,\text{cm}^{-1}$ and therefore an effective two-body rate between thermal and BEC atoms of $\approx 28 \times 10^3\,\text{s}^{-1}$ at zero TOF, which drops to $\approx 0.5 \times 10^3\,\text{s}^{-1}$ at 100 μs

TOF. This is roughly consistent with the TOF–averaged loss rate Γ_{obs}.

B.7 Atom number fitting procedure

To obtain the atom number from our absorption images, we restrict (by eye) the vertical (or horizontal) axis to an interval containing the high-density peak(s) within the cigar-shaped cloud. By integrating along the other axis, the bimodal distribution is clearly visible in the resulting one-dimensional profile. For images that appear to contain only one BEC, we fit the resulting data to the sum of two Gaussian distributions, which describes a high-density component on top of a broad thermal component. The atom numbers within each component are then determined using the fit parameters (specifically, the optical depths and the RMS sizes). The residuals between the raw data and the bimodal fits give an estimate for the errorbars on the estimated atom number in the BEC.

For images that appear to contain multiple BECs, we fit the broad thermal component to a single Gaussian distribution, which is then subtracted from the data. The residuals depicting the high-density peaks are assumed to be BEC atoms, whose spatial extent is distinguished (by eye) from the remaining density fluctuations of the broad thermal background. These residuals are then integrated to give the number of atoms in the BEC. The main source of systematic errors is dominated by the finite offset of these residuals, which depends on the Gaussian fit to the thermal cloud. We assume the noise in this choice of offset is given by the RMS noise (standard deviation) on the background thermal distribution.

C

Supplement for chapter 7

C.1 Experimental Setup

Our machine-learning-enhanced ensemble loading procedure is previously described in ref. [162], which enables loading of (up to) a factor of 5 higher in atom number and 2.5 lower in temperature compared to manual optimization. The trapping light ($\lambda = 808$ nm) generated by the SLM (Hamamatsu x13138-02) is focused through our commercial microscope objective (Mitutoyo M Plan Apo NIR B

20X 378–867–5, NA $= 0.4$) to a $1/e^2$ beam waist of $w_0 = 4.9\,\mu$m.

After loading, each trap contains ≈ 1500 atoms, however, the longitudinal size of the ensemble (RMS size $\sigma_z = 32\,\mu$m) is much larger than typical Rydberg blockade radius. Therefore, we compress the ensembles axially with two sheets of blue-detuned beams ($\lambda = 770\,$nm) generated with a one-dimensional AOD (DTSX-400-800.850). This compression is performed over 80 ms by stepping the AOD RF frequencies generated by a DDS (AD9959), starting from a separation of $135\,\mu$m (which is sufficiently large to prevent effects on initial trap loading) and ending at $15\,\mu$m. After holding atoms in-trap for 20 ms, we find that each trap contains ≈ 200 atoms with $\sigma_x = 2\,\mu$m, $\sigma_y = 2.5\,\mu$m, $\sigma_z = 4\,\mu$m, which is determined through absorption imaging (Hamamamtsu ORCA-Quest C15550-20UP). The choice of a large trap waist and subsequent compression is motivated by the goal to maximize the number of atoms within the blockade radius to improve collective Rydberg EIT imaging.

Note that we find it is preferable to keep the traps on throughout the remainder of the sequence – namely, during the Rydberg preparation and detection process. Our trap depth ($\approx 1\,$MHz) is sufficiently small such that effects of Rydberg line-broadening or anti-trapping of the Rydberg state are less detrimental compared to diffusion of ground-state atoms when traps are turned off.

After ensemble compression, we increase the magnetic field to 9 G along the propagation axis of the tweezer light, which defines the quantization axis for the remainder of the sequence. We optically pump the atoms in 4 ms with σ^+ polarized light on $F = 2 \rightarrow F' = 2$ to the dark state $|g\rangle = |5S_{1/2}, F = 2, m_F = 2\rangle$, while repumping with unpolarized light on $F = 1 \rightarrow F' = 2$ (both optical pumping and repump lasers address the D2 line).

C.2 Three-photon preparation

We choose to work with $n = 75$, which is sufficiently large for Rydberg blockade during state preparation and detection, without significantly increasing the self-blockade effect of Rydberg polaritons [103].

To prepare a single Rydberg excitation within an ensemble, we use a global 780 nm beam, a 5.214 GHz microwave (MW) source, and a 480 nm site-selective addressing beam ($w_0 = 2.3\,\mu$m), which is used to selectively illuminate either preparation or detection ensemble. Since the 480 nm light is on-resonance, we blue-detune both the 780 nm and MW frequencies by $\delta = 100$ MHz to avoid populating the intermediate states.

Our preparation scheme and parameters used in this experiment are similar to those described in [148]. We prepare a single Rydberg atom in the state $|75\mathrm{P}_{3/2}, m_J = 3/2\rangle$ with $C_6 = 45\,\mathrm{GHz}\,\mu\mathrm{m}^6$, and we observe a power-broadened three-photon linewidth of $\gamma_{3\mathrm{ph}}/(2\pi) \approx 500$ kHz, corresponding to a blockade radius of $\left(C_6/\gamma_{3\mathrm{ph}}\right)^{1/6} = 6.7\,\mu$m, which is sufficient to block the preparation of multiple Rydberg excitations. All three legs of the three-photon transition are turned on simultaneously, and we observe saturation of Rydberg population with a characteristic timescale of $\approx 3\,\mu$s in the overdamped regime. We do not observe collective oscillations consistent with the preparation of a $|W\rangle$ state, which we attribute to fast dephasing of the $|W\rangle$ state (a few hundred nanoseconds has been experimentally observed [56]). Therefore, we prepare a statistical ensemble consisting of a single Rydberg excitation randomly distributed within the cloud with an upper-bounded-fidelity of $N/N+1$, where N is the number of atoms [57].

C.3 Site-selective preparation and detection using AOD on the control field

As written in the main text, site-selective preparation and detection are performed using a 480nm AOD on the σ^+ polarized control beam, which co-propagates with the trapping light (see Fig. 1c of the main text). The remaining fields used for preparation and detection are global beams. For EIT detection, the resonant σ^+ polarized 780 nm probe beam ($w_0 = 1$ mm) counter-propagates along the tweezer axis. For three-photon preparation, the linearly polarized 780 nm beam ($w_0 = 1$ mm)

propagates along the transverse axis of traps. The microwave (MW) field used for preparation and Rabi driving is an unpolarized field generated by a stub-terminated SMA cable [174].

To selectively prepare a Rydberg atom in one ensemble and perform subsequent readout using a neighbouring ensemble, we switch the 480 nm AOD frequency mid-sequence, which takes $8\,\mu$s due to our choice of a large beam at the AOD ($w_0 = 2.6$ mm). For all experiments presented in this work, the light is turned off before AOD switching with the use of an additional AOM to prevent ensembles from being illuminated by control light while AOD frequency is being stabilized. In our sequence, we perform state preparation, switch the AOD frequency, and wait $10\,\mu$s before EIT detection. The control beam detuning in the atom plane has spatial dependence of $344\,\text{kHz}/10\,\mu\text{m}$. Given that our three-photon preparation linewidth ($\gamma_{3\text{ph}}/(2\pi) \approx 500\,\text{kHz}$) is significantly smaller than our EIT detection linewidth (on the order of $\Omega_c/(2\pi) = 5 - 20\,\text{MHz}$ throughout this work), we tune the control beam on-resonance for the preparation of a single ensemble. For the distances investigated in this work (up to $40\,\mu$m), the finite two-photon EIT detuning is small compared to the linewidth, and we experimentally verify that this does not have a significant effect on our results.

C.4 Choice of Rydberg states: $D - P$ vs. $S - P$

Typical Rydberg atom array experiments choose a principal quantum number n and tweezer spacing such that the system operates in the van-der-Waals regime, where the Rydberg blockade is dominated by coupling to one isolated Rydberg state. However, within small mesoscopic ensembles, the mean-free-path of atoms can be on the order of $\sim 1\,\mu$m for densities of $\sim 10^{12}\,\text{cm}^{-3}$ [162], in which resonant dipole-dipole interactions between many pair states can lead to complicated energy landscapes. Colloquially known as the "spaghetti" regime, isolating a pair of Rydberg states to engineer clean dipolar interactions is challenging in atomic ensembles and requires careful choice of Rydberg states and external electric/magnetic bias fields [175,176]. For example, interactions between Rydberg polaritons at

short distances can lead to finite populations in other degenerate Zeeman sublevels, thus leading to a reduction in EIT transmission over the course of probing [147].

As a result, we choose to work with Rydberg polaritons in the state $|74\mathrm{D}_{5/2}, m_J = 5/2\rangle$ with $C_6 \approx -1600\,\mathrm{GHz}\,\mu\mathrm{m}^6$, while ensuring the probe rate is sufficiently low to avoid exciting more than one polariton in the cloud at a given time to prevent self-blockade [103]. Additionally, the prepared Rydberg state $|75\mathrm{P}_{3/2}, m_J = 3/2\rangle$ strongly interacts with polaritons, where $C_3 = 11.15\,\mathrm{GHz}\,\mu\mathrm{m}^3$ for $\theta = 90°$, corresponding to a large blockade radius of $\left(2C_3/\gamma_{\mathrm{EIT}}\right)^{1/3} = 10.4\,\mu\mathrm{m}$ for typical $\Omega_c/(2\pi) = 20\,\mathrm{MHz}$ used in this work. Despite the anisotropy of D states, $D-P$ interactions generally show much cleaner dipolar splitting and larger interaction strengths in comparison to $S-P$ interactions, particularly for the distances reported in this work. An example showcasing the purity of exchange interactions for $D-P$ states in comparison to $S-P$ states (calculated with the "pairinteraction" software [53]) is shown in Fig. C.1.

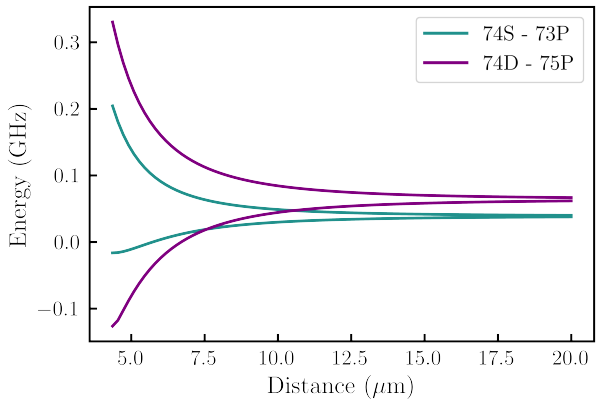


Figure C.1: DP vs SP: An example showcasing the purity of exchange interactions for $D-P$ states in comparison to $S-P$ states (calculated with the "pairinteraction" software [53]). The states are chosen so that both the D and S states share the same Rydberg n level, while the P states in each case are selected to maximize interaction strength, reflecting the selection criteria that would be used in experimental settings.

C.5 Full interaction space experiment

As described in the main text, the full interaction space measurements shown in Fig. 2 were obtained by varying the separation between the preparation and detection ensembles for a fixed control Rabi frequency of $\Omega_c/(2\pi) = 5.5\,\mathrm{MHz}$. As the distance between the two ensembles was varied, the 480 nm AOD frequencies were adjusted to ensure proper illumination of each ensemble during site-selective preparation and detection. The probe rate was optimized to achieve the highest photon rate while minimizing self-blockade effects, which resulted in $\Omega_p/(2\pi) \approx 130\,\mathrm{kHz}$.

To improve the SNR, each data point was averaged 75 times, obtained by performing 80 repetitions (per MOT loading cycle) consisting of $3\,\mu$s state preparation in one ensemble, $10\,\mu$s switching of the control AOD frequency, followed by $10\,\mu$s detection in the neighbouring ensemble. Despite the long lifetime of the prepared Rydberg state ($225\,\mu$s), we find that waiting $100\,\mu$s between each repetition is sufficient since the Rydberg states are anti-trapped by ground state atoms trap light.

In Fig. 2 of the main text, we plot the contrast, which is defined as the reduction in normalized transmission through the detection ensemble, as a function of the inter-ensemble dipolar interaction strength. This contrast is upper-bounded by the height of the EIT resonance, which is ≈ 0.4 of the normalized probe field transmission.

C.6 Evidence of Rydberg blockade

To demonstrate that the blockade regime can be achieved with two mesoscopic ensembles, we performed the experiment shown in Fig. C.2. We loaded two ensembles at a separation of $11.7\,\mu$m, prepared a Rydberg atom in the left ensemble, and performed detection of both ensembles with a global, linearly polarized 480 nm beam which propagates along the transverse axis of traps. At this distance, the dipolar interaction strength is $14.8\,\mathrm{MHz}$[53]. When detection is performed with $\Omega_c/(2\pi) = 23\,\mathrm{MHz}$ ($r_b = 9.9\,\mu$m), the right ensemble is outside the blockade radius of the prepared Rydberg

atom (in the left ensemble) and the observed detection contrast is much smaller in the right ensemble compared to the left, as expected (shown in green). On the contrary, when $\Omega_c/(2\pi) = 8\,\mathrm{MHz}$ ($r_b = 14.1\,\mu\mathrm{m}$), we find that the observed contrast in left ensemble doesn't change while the contrast in the right ensemble increases to a level similar to the one of the left ensemble (as shown in purple). Since the left ensemble is blockaded, as Rydberg atom is prepared at that site, and the right ensemble detects a similar signal, meaning that the signal is independent of distance, this indicates the involvement of the blockade effect at the right ensemble.

These measurements were taken with multiple repetitions per MOT loading cycle (as described in the previous section), and the probe rate was similarly maximized for each control Rabi frequency.

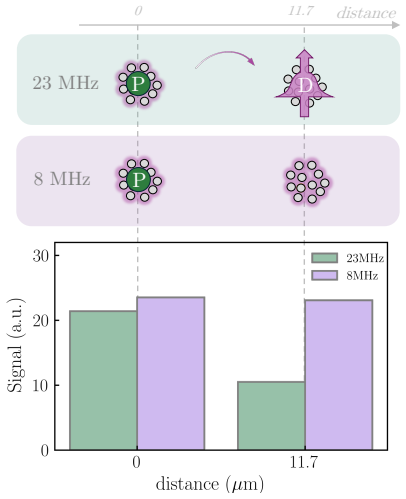


Figure C.2: Rydberg blockade evidence: The bar graphs show the observed signal in each ensemble following preparation of a Rydberg atom in the left ensemble. Following preparation, simultaneous readout of both ensembles is performed for two control Rabi detection parameters $\Omega_c/(2\pi) = 8\,\mathrm{MHz}$ (purple bars) and $\Omega_c/(2\pi) = 23\,\mathrm{MHz}$ (green bars). When the distance between ensembles is smaller than the blockade radius (purple panel; $\Omega_c/(2\pi) = 8\,\mathrm{MHz}$), the observed signal is the same in both ensembles. Since the Rydberg atom is only prepared in the left ensemble, in which it is detected via blockade effect, achieving a similar contrast signal in both ensembles indicates the involvement of the blockade effect at the right ensemble as well.

C.7 Evidence of dipolar hopping: experimental details

To confirm that the prepared Rydberg excitation has hopped into a neighbouring ensemble (as shown in Fig. 3b), the experimental sequence consisted of the following: (1) a Rydberg excitation was prepared in the middle ensemble in 3 μs of time, (2) the 480 nm AOD frequency was switched to address the outer neighbouring ensembles within 10 μs, (3) EIT detection light illuminated neighbouring ensembles for 10 μs, thereby exciting Rydberg polaritons, (4) the 480 nm AOD frequency was switched back to address the middle ensemble within 10 μs, and finally, (5) the Rydberg population in the middle ensemble was measured via EIT detection in 10 μs and plotted in the bar graph. In other words, the bar graph shows the Rydberg population in the middle ensemble at the end of the sequence, depending on whether the control light is turned on in step 3 (purple) or not (green), thus serving as a differential measurement of whether the generation of polaritons in neighbouring ensembles affects the stationary Rydberg population in the middle ensemble. Evidently, the population in the middle ensemble drops in the presence of Rydberg polaritons (purple; which is normalized to the green reference measurement). As a sanity check, we perform the same experiment without loading neighbouring ensembles, in which case we do not observe suppression in signal when control light is turned on in step 3, and we conclude that our observation cannot be explained by e.g. crosstalk due to finite size effects of our site-selective control beams. This confirms that the observed loss of Rydberg population in Fig. 3b is due to interactions of the prepared Rydberg atom with neighbouring Rydberg polaritons, which leads to dipolar hopping. As before, these measurements were taken with multiple repetitions per MOT loading cycle (as described previously). Note that for the data presented in Fig. 3a, the signal represents detection contrast normalized to the maximum contrast observed for this dataset (at 13.3 μm).

C.8 Parameters affecting detection fidelity

The parameter space of this detector is quite complex. Next, we analyse the effect of each parameter on the performance of the detector and propose changes necessary to achieve a readout fidelity of 99.3% in future implementations. The most important parameters affecting the detector, as described below, include probe photon collection efficiency, optical density (OD), control Rabi frequency, Rydberg n level, and the distance between the detector and the prepared Rydberg atom.

Probe photon collection efficiency: one simple upgrade that would enhance the detector's performance is the use of a microscope objective with better transmission at our probe wavelength of 780 nm. Our current objective transmits $62\,\%$ of our probe photons, however, objectives with $\approx 90\,\%$ transmission are readily available, which would increase our detected photon rate by $\approx\ 50\,\%$, thereby enhancing the SNR by $\approx 22\,\%$.

Optical depth: we empirically determined that the optimal OD for this detector lies within the range of $0.9 - 1.7$ due to the competition between two factors: the probe rate, and maximum signal contrast due to probe photon absorption of the ensemble. The number of photons detected scales with the incident probe rate, however, due to self-blockade effect [103], the maximum probe rate scales inversely with OD (proberate $= \Omega_c/\mathrm{OD}$). However, a higher OD increases the maximum signal contrast $\mathrm{C} = (1 - e^{-\mathrm{OD}})$, which we define as the maximum normalized probe photon absorption. Considering both factors, the overall detection SNR scales as $\sqrt{\text{proberate}} \times \mathrm{C}$, which is maximized for OD in the range of $0.9 - 1.7$.

Control Rabi frequency: since the probe rate scales as Ω_c/OD, higher control Rabi frequencies are preferable. However, increasing the control Rabi frequency also reduces the blockade radius, given by $\left(2C_3/\gamma_{\mathrm{EIT}}\right)^{1/3}$. We empirically find that a control Rabi frequency on the order of 20 MHz is optimal for balancing these effects.

Rydberg n level: the aforementioned two factors influence our choice of Rydberg level as well. At

lower n, higher probe rates are permitted due to smaller self-blockade interactions [103]. On the other hand, better detector performance is achieved in the blockade regime, which necessitates a larger blockade radius. Therefore, the optimal n is the smallest n for which the interaction strength at the inter-ensemble distance is on the order of the control Rabi frequency. Therefore, this parameter should be determined once the distance between the detector and qubit ensembles is selected.

Considering these constraints, we hypothesize that the optimal detector configuration involves placing a large detector ensemble adjacent to a tightly-focused tweezer which confines a single-atom qubit. Assuming a $5\,\mu$m beam waist for the detector ensemble and a $\sim 1\,\mu$m waist for the qubit, separations of $\approx 7-8\,\mu$m can be achieved. With $\Omega_c/(2\pi) = 20$ MHz, the blockade regime can still be achieved for relatively low n (e.g. $54\mathrm{D}_{5/2}$) at this distance. By implementing only these changes – lower n level, closer detector-qubit distance, and improved microscope objective transmission – we expect to achieve $\approx 78\,\%$ detection fidelity in this setup. We estimate this by scaling both the signal and noise by the appropriate factor proportional to the expected probe rate enhancement from these changes.

To push the fidelity further, we envision moving the single-atom tweezer inside the detector prior to the state preparation and detection process. By preparing the qubit atom in a different hyperfine state (e.g. F = 1), we can prepare the qubit atom in a Rydberg state (and subsequently detect it) without disturbing nearby detector atoms. This approach allows a large detector ensemble to be operated within the blockade regime. Therefore, if the detector trap radius is doubled (and assuming the number of atoms increases fourfold), the signal would increase fourfold, and the SNR would double. With these improvements, we estimate that a fidelity of $\sim 99\%$ can be achieved. In a dual-species setup, with the right choice of Rydberg levels for each species, one can predominately have van der Waals interactions instead of exchange interactions, which can further minimize hopping and improve detection fidelity.

C.9 Microwave Rabi oscillation: experimental details

The microwave (MW) field used for preparation and MW Rabi oscillations is a global field at $\nu = 5.214\,\mathrm{GHz}$ during preparation, which is $+100\,\mathrm{MHz}$ detuned from the $|74\mathrm{D}_{5/2}, m_J = 5/2\rangle \rightarrow |75\mathrm{P}_{3/2}, m_J = 3/2\rangle$ transition. During Rabi driving, the microwave field is on-resonance at $\nu = 5.114\,\mathrm{GHz}$.

We perform "non-local" microwave Rabi oscillations consisting of the following: we prepare a single Rydberg atom in the qubit ensemble in $3\,\mu$s, switch the $480\,\mathrm{nm}$ AOD frequency while applying the resonant MW field for a variable duration, and perform readout of the detector ensemble. To achieve fast switching of the high-frequency MW field, we mix a $100\,\mathrm{MHz}$ source with a high-frequency source set to $5.214\,\mathrm{GHz}$. The difference frequency is on-resonance with the microwave transition, which can be quickly turned off using low-frequency electronics on the $100\,\mathrm{MHz}$ source. For the data in Fig. 4c, multiple repetitions per sequence, as described previously, was used.

The MW field used in this work was not polarized. Our simulations suggest that this is the primary reason we did not achieve full contrast in the Rabi oscillations shown in Fig. 4c, which is consistent with imperfect population transfer to the $|74\mathrm{D}_{5/2}, m_J = 5/2\rangle$ state. Nevertheless, coherent Rabi oscillations persist for durations $> 13\,\mu$s, as shown in Fig. C.3b.

C.10 Rydberg coherence time

To ensure that the prepared Rydberg within the ensemble has a sufficiently long coherence time to interact with the neighbouring Rydberg polariton, we measured the coherence time while driving the $|75\mathrm{P}_{3/2}, m_J = 3/2\rangle \leftrightarrow |74\mathrm{D}_{5/2}, m_J = 5/2\rangle$ transition. This was done using a Ramsey sequence, with two resonant $\pi/2$ pulses and a variable delay time in-between. The data, shown in Fig. C.3a, reveals a coherence time of $12(3)\,\mu$s, which is sufficient to allow coherent oscillations between the stationary Rydberg atom with neighbouring Rydberg polaritons within a duration of the group de-

lay (shorter than $1\,\mu$s). The "non-local" MW Rabi oscillation experiment, as described previously, confirms that the coherence time exceeds $10\,\mu$s.

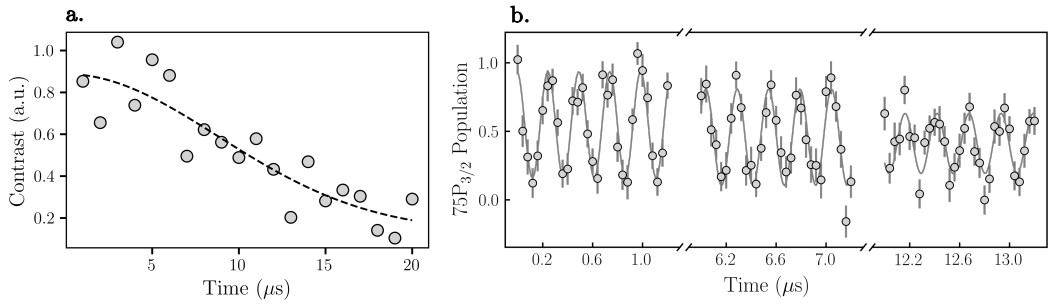


Figure C.3: Coherence time and long Rabi oscillations: a. Contrast observed in a Ramsey sequence with microwave driving of the $|75\mathrm{P}_{3/2}, m_J = 3/2\rangle \leftrightarrow |74\mathrm{D}_{5/2}, m_J = 5/2\rangle$ transition. From the fitted curve, we extract a coherence time of $T_2^* = 12(3)\,\mu$s. **b.** "Non-local" Rabi oscillation experiment shows that the prepared Rydberg atom can be driven coherently using a microwave field for longer than $12\,\mu$s.

C.11 Multiple Rydberg detectors experiment

One unique feature of this detector compared to free-space and cavity-based fluorescence imaging methods is that multiple detectors can be employed to read out a single qubit. In the blockade regime, it is expected that each detector would observe the same signal, thus enhancing the imaging SNR by a factor $\sqrt{N}$, where N is the number of detectors.

Even though we were unable to reach the blockade regime in our system for optimal readout, we demonstrate this technique as a proof-of-principle. We prepare multiple detector ensembles equidistant from the qubit ensemble, as shown in Fig. C.4, and we observe that the SNR per ensemble drops with the addition of more detectors. In other words, the total detection SNR summed over all detectors remains constant. These observations further support the occurrence of Rydberg excitation hopping from the qubit to ensemble detectors at distances of $r = 19\,\mu$m, which lies in the classical hopping regime for the control Rabi frequency $\Omega_c/(2\pi) = 20$ MHz used in this measurement.

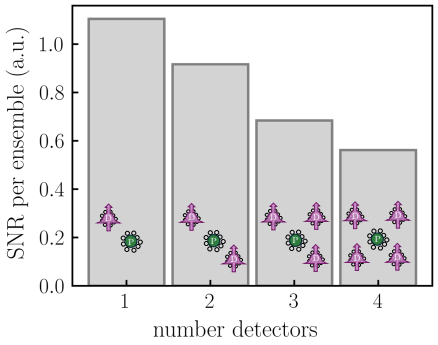


Figure C.4: Multiple Rydberg detectors experiment: Multiple ensemble detectors (purple) are prepared at a distance of $19\,\mu$m from the qubit ensemble (green). The bar graph displays the detection SNR per ensemble as a function of the number of detectors, which decreases with the addition of more detectors. However, after summing over all detectors, the total detection SNR remains constant (not shown in the figure). This observation supports the occurrence of hopping at these distances.

C.12 Our phenomenological theory

In this section, we describe the phenomenological theory used to derive the fitted curve shown in Fig. 2 of the main text. Our model is based on the competition between polariton blockade and spin-exchange interactions, both caused by the same dipole-dipole interaction. The contrast, i.e. normalized amount of absorbed photons, in the theory is described by the equation $C = p_{\text{block}} \cdot C_{\text{block}} + (1 - p_{\text{block}}) \cdot C_{\text{hop}}$, where C_{block} is the contrast expected from blockade of polariton formation given the polariton-Rydberg atom interaction strength and the EIT linewidth, C_{hop} is the contrast signal expected from hopping, and p_{block} is the probability that a polariton will be blocked. The probability p_{block} is further defined as $p_{\text{block}} = \frac{V_{PD}(r)}{\Gamma_{EIT}}$, where for distances $\frac{V_{PD}(r)}{\Gamma_{EIT}} > 1$, p_{block} is set to 1.

The blockade contrast, C_{block}, is defined as the constant contrast, due to blockade of polariton formation, which is a free parameter in the theory curve, found to be approximately 0.23. This value coincides with the saturated contrast observed in Fig. 2 of the main text for large control Rabi values.

The hopping contrast, C_{hop} is a bit more complicated and it is defined in the following way. We assume that the polariton is present inside the cloud over a duration given by the group delay $\tau_d =$

$\gamma\frac{\mathrm{OD}}{\Omega_c^2}$, during which the polariton and Rydberg atom interact with $V_{PD}(r) = C_3/r^3$. When the polariton exits the ensemble, the Rydberg atom and the polariton are described by the entangled state $\Psi_{\text{polariton, atom}} = \alpha\,|DP\rangle + \beta\,|PD\rangle$. The polariton can then exit the ensemble as a transmitted photon, which is then detected by the camera with a probability of α^2, projecting the detector ensemble into a state with no Rydberg excitations for the next incident photon. Alternatively, the polariton can be projected into the P state with a probability of β^2, which causes the next incident photon to be blocked. Thus, our theory assumes that until the P state has hopped into the detector ensemble, the contrast in that ensemble is zero (i.e. photons are transmitted). Once the P state has hopped, the contrast in that ensemble will be a constant, given by the blockade level contrast, as the local P state will block subsequent photons from entering. The probability that the P state is projected into the polariton cloud is given by $\beta^2 = \frac{1-\cos(2\pi\cdot 2V_{PD}\tau_d)}{2}$. We also assume that the hopping between the polariton and the Rydberg atom is imperfect and that the contrast decays with rate Γ_d. This is expressed as $\beta^2 = \frac{1-e^{-\Gamma_d\tau_d}\cos(2\pi\cdot 2V_{PD}\tau_d)}{2}$. By combining the above probability with the probe rate, we calculate the duration it takes for the P state to hop within the EIT detection duration of $10\,\mu$s used in this measurement. The hopping contrast, C_{hop}, is then equal to the fraction of time the P state was present in the detector ensemble. We note here that we also took into account that the Rydberg fraction of the polariton is not unity, by multiplying the fraction with the probability above.

Using this model, we fit the data with free parameters that ultimately match the experimentally estimated values. The probe rate is fitted to be $\sim 0.94\,\mathrm{ph}/\mu\mathrm{s}$ (experimental value $\sim 0.7\,\mathrm{ph}/\mu\mathrm{s}$). The control Rabi frequency is fitted to be $\Omega_c/(2\pi) = 4.98\,\mathrm{MHz}$ (experimental value $\Omega_c/(2\pi) = 5.5\,\mathrm{MHz}$), and the optical depth (OD) is fitted to be $\mathrm{OD} = 1.54$ (experimentally observed peak OD is approximately 2, with an average OD of approximately 1.35).

D

Supplement for chapter 8

D.1 Experimental Setup

An array of optical tweezers is generated with a spatial light modulator (SLM; Hamamatsu x13138-02) focused through a microscope objective lens (Mitutoyo M Plan Apo NIR B 20X 378–867–5, NA = 0.4). The experimental sequence consists of a 100-ms-long magneto-optical-trap (MOT) cooling and loading stage, followed by a 40-ms-long MOT compression stage, during which an ensemble of ^{87}Rb

atoms is loaded into each tweezer. The magnetic gradient is then switched off, and the bias field along the x direction is increased to 2.3 G. All measurements in this work are performed in this constant magnetic field.

The σ^+ polarized EIT control beam used for cooling is addressing $|5S_{1/2}, F = 2, m_F = 1\rangle \rightarrow |5P_{3/2}, F = 2, m_F = 2\rangle$ transition with measured Rabi frequency of $\Omega_c/(2\pi) = 7.5$ MHz. For a single-photon detuning of $\Delta/(2\pi) = 36$ MHz (relative to trap-shifted line) used for cooling, the estimated AC Stark shift of the control light is given by $\delta_{\mathrm{AC}}/(2\pi) = \Omega_c^2/4\Delta = 390$ kHz. The expected Fano linewidth $\gamma_{2\mathrm{ph}}/(2\pi) = 2\delta_{\mathrm{AC}}(\Gamma/\Delta) = 130$ kHz is similar to the observed linewidth of ≈ 150 kHz, which is larger than the trapping frequencies ($\omega_r/(2\pi) = 45$ kHz and $\omega_z/(2\pi) = 4$ kHz), indicating that we are operating well outside the Lamb-Dicke regime.

The π polarized EIT probe beam addresses $|5S_{1/2}, F = 2, m_F = 2\rangle \rightarrow |5P_{3/2}, F = 2, m_F = 2\rangle$ transition. The probe beam aligned in the $y - z$ plane has measured Rabi frequency of $\Omega_p/(2\pi) = 0.52$ MHz, while the probe light aligned along the y direction has $\Omega_p/(2\pi) = 0.79$ MHz.

The fluorescence imaging beam is σ^+ polarized and -67 MHz detuned (relative to trap-shifted line) from $|5S_{1/2}, F = 2, m_F = 2\rangle \rightarrow |5P_{3/2}, F = 3, m_F = 3\rangle$ transition. We estimate the scattering rate of this beam from the laser power and beam waist sent to the experiment to be $\sim 1.0 \times 10^5$ s^{-1}, consistent with 130 ± 10 kHz AC Stark shift observed in inset of Fig. 3b of the main text. A polarized repump beam addresses the $|5S_{1/2}, F = 1\rangle \rightarrow |5P_{3/2}, F = 2\rangle$, generated as a sideband on the σ^+ control beam via a phase electro-optic modulator (EOM; iXblue NIR-MPX800-LN-05-00-P-P-FA-FA).

D.2 Monte Carlo temperature fit details

We extract the temperature of the single atoms through a release and recapture method, fitted using Monte-Carlo simulations [50]. After imaging and verifying the distribution of single atoms in the array,

traps are switched off, allowing the atoms to diffuse. The traps are switched back on after the release time, and the probability of losing an atom during that time is recorded. Each data point was repeated 40 times, with an average number of 5 atoms.

A Monte-Carlo simulation takes into account gravity and the trap parameters and calculates an expected loss probability curve as a function of release time for different temperatures between 0 and $200\,\mu$K, with a $1\,\mu$K resolution. Trap parameters assumed in the simulation (as extrapolated from measurement at lower powers) are wavelength ($\lambda = 808\,$nm), radial trapping frequency ($\omega_r/(2\pi) = 45\,$kHz) , axial trapping frequency ($\omega_z/(2\pi) = 4\,$kHz), trap depth ($U = 0.91\,$mK) and trap waist size ($w_0 = 1.6\,\mu$m). The final atomic distribution is sampled 10000 times per release time for each temperature, determining a loss event when the trap depth at the final position is smaller than the atom kinetic energy. A weighted least square value between the measured and simulated loss probability curves is used to determine the most likely temperature in experiment.

The statistical error in the temperature is calculated by taking into account the variance in the measured data (each data point is averaged 40 times) and attempting to fit 100 times. The systematic error is calculated by assuming $\sim 10\,\%$ variance in trap parameters. Fitting appears to be most sensitive to variations in the trap waist. For the fitting of the temperatures after cooling or after imaging while cooling, the systematic error dominates. For the temperature of atoms directly after PGC, a combination of systematic and statistical errors determines the total error.

D.3 2D High B field imaging

To verify that our loading and imaging technique is compatible with zoned architectures, it is important to demonstrate its effectiveness in 2D. For the following measurements, we block the π probe light propagating along the *y* direction, ensuring that the 2D imaging involves only the *x* and *z* (axial) directions (see Fig. 1a of the main text). Since the axial direction is much more weakly confined, we

find it is much more important to cool with the probe beam along the z direction compared to y, as atoms can escape more easily from recoil heating along the axial direction. Histograms from 200 ms of imaging are shown in Fig. D.1. Without 3D cooling, it is necessary to adjust imaging parameters to minimize atom loss, primarily by reducing the imaging power by a factor of 2. As a result, readout becomes significantly slower and of lower fidelity ($89(1)$ %). However, as described in the main text, with modest technical improvements (namely, a better microscope objective lens), the imaging duration can be substantially shortened to reduce atom loss, and fidelities at the 99 % level are anticipated. This demonstrates that our imaging technique functions in two dimensions, making it compatible with zoned architectures and prospects for continuous reloading via optical conveyor belts[33,34,35].

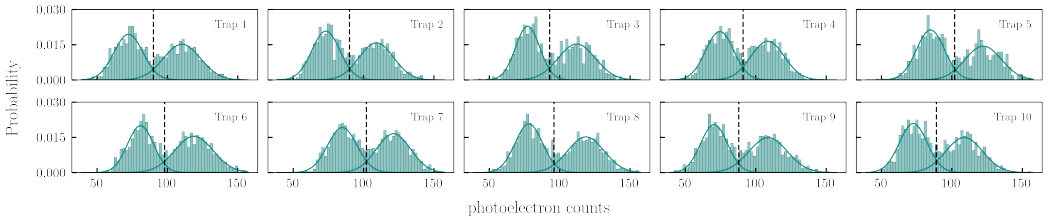


Figure D.1: High B field imaging in 2D: Histogram distribution of high B-field imaging performed in 2D. The data, collected over 200 ms for 10 different traps, shows an average fidelity of $89(1)$ % in distinguishing a single atom from the background. Both the speed and readout fidelity can be significantly improved with the use of a higher-performance microscope objective lens.

D.4 Imaging dependence on trap depth

We investigate the dependence of atom loss on the tweezer depth. Our results in Fig. D.2 indicate that deeper traps should help retain atoms, with $1.8(3)$ % loss achieved at typical trap depths used in alkali-atom-array experiments. The data was obtained by varying the trap depth while keeping the parameters for cooling and imaging (such as laser detunings and powers) fixed, which were previously optimized for an AC Stark shift of 23 MHz (i.e. trap depth of 18.2 MHz). We note that EIT imaging could be improved at lower trap depths by optimizing parameters for the corresponding trap depth.

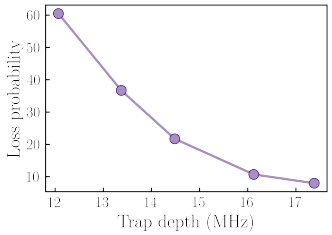


Figure D.2: Imaging dependence on trap depth: Data showing atom loss probability during a single imaging application as a function of trap depth. The results indicate that our imaging technique is effective for trap depths commonly used in atom array experiments, and that deeper traps can further enhance atom retention.

References

[1] Richard P. Feynman. Simulating physics with computers. *International Journal of Theoretical Physics*, 21(6):467–488, Jun 1982.

[2] Waseem S. Bakr, Jonathon I. Gillen, Amy Peng, Simon Folling, and Markus Greiner. A quantum gas microscope for detecting single atoms in a hubbard-regime optical lattice. *Nature*, 462:74–77, 2009.

[3] Rajibul Islam, Ruichao Ma, Philipp M. Preiss, M. Eric Tai, Alexander Lukin, Matthew Rispoli, and Markus Greiner. Measuring entanglement entropy in a quantum many-body system. *Nature*, 528:77–83, 2015.

[4] Anton Mazurenko, Christie S. Chiu, Geoffrey Ji, Maxwell F. Parsons, Márton Kanász-Nagy, Richard Schmidt, Fabian Grusdt, Eugene Demler, Daniel Greif, and Markus Greiner. A cold-atom fermi-hubbard antiferromagnet. *Nature*, 545:462–466, 2017.

[5] G. Semeghini, H. Levine, A. Keesling, S. Ebadi, T. T. Wang, D. Bluvstein, R. Verresen, H. Pichler, M. Kalinowski, R. Samajdar, A. Omran, S. Sachdev, A. Vishwanath, M. Greiner, V. Vuletić, and M. D. Lukin. Probing topological spin liquids on a programmable quantum simulator. *Science*, 374:1242–1247, 2021.

[6] Peter W. Shor. Polynomial-time algorithms for prime factorization and discrete logarithms on a quantum computer. *SIAM Journal on Computing*, 26(5):1484–1509, 1997.

[7] Javier Argüello-Luengo, Alejandro González-Tudela, Tao Shi, Peter Zoller, and J. Ignacio Cirac. Analogue quantum chemistry simulation. *Nature*, 574(7777):215–218, Oct 2019.

[8] Nick S. Blunt, Joan Camps, Ophelia Crawford, Izsák Róbert, Sebastian Leontica, Arjun Mirani, Alexandra E. Moylett, Sam A. Scivier, Christoph Sünderhauf, Patrick Schopf, Jacob M. Taylor, and Nicole Holzmann. Perspective on the current state-of-the-art of quantum computing for drug discovery applications. *Journal of Chemical Theory and Computation*, 18(12):7001–7023, Dec 2022.

[9] Frank Arute, Kunal Arya, Ryan Babbush, Dave Bacon, Joseph C. Bardin, Rami Barends, Rupak Biswas, Sergio Boixo, Fernando G. S. L. Brandao, David A. Buell, Brian Burkett,

Yu Chen, Zijun Chen, Ben Chiaro, Roberto Collins, William Courtney, Andrew Dunsworth, Edward Farhi, Brooks Foxen, Austin Fowler, Craig Gidney, Marissa Giustina, Rob Graff, Keith Guerin, Steve Habegger, Matthew P. Harrigan, Michael J. Hartmann, Alan Ho, Markus Hoffmann, Trent Huang, Travis S. Humble, Sergei V. Isakov, Evan Jeffrey, Zhang Jiang, Dvir Kafri, Kostyantyn Kechedzhi, Julian Kelly, Paul V. Klimov, Sergey Knysh, Alexander Korotkov, Fedor Kostritsa, David Landhuis, Mike Lindmark, Erik Lucero, Dmitry Lyakh, Salvatore Mandrà†, Jarrod R. McClean, Matthew McEwen, Anthony Megrant, Xiao Mi, Kristel Michielsen, Masoud Mohseni, Josh Mutus, Ofer Naaman, Matthew Neeley, Charles Neill, Murphy Yuezhen Niu, Eric Ostby, Andre Petukhov, John C. Platt, Chris Quintana, Eleanor G. Rieffel, Pedram Roushan, Nicholas C. Rubin, Daniel Sank, Kevin J. Satzinger, Vadim Smelyanskiy, Kevin J. Sung, Matthew D. Trevithick, Amit Vainsencher, Benjamin Villalonga, Theodore White, Z. Jamie Yao, Ping Yeh, Adam Zalcman, Hartmut Neven, and John M. Martinis. Quantum supremacy using a programmable superconducting processor. *Nature*, 574(7779):505–510, Oct 2019.

[10] J. Zhang, G. Pagano, P. W. Hess, A. Kyprianidis, P. Becker, H. Kaplan, A. V. Gorshkov, Z.-X. Gong, and C. Monroe. Observation of a many-body dynamical phase transition with a 53-qubit quantum simulator. *Nature*, 551(7682):601–604, Nov 2017.

[11] Dolev Bluvstein, Simon J. Evered, Alexandra A. Geim, Sophie H. Li, Hengyun Zhou, Tom Manovitz, Sepehr Ebadi, Madelyn Cain, Marcin Kalinowski, Dominik Hangleiter, J. Pablo Bonilla Ataides, Nishad Maskara, Iris Cong, Xun Gao, Pedro Sales Rodriguez, Thomas Karolyshyn, Giulia Semeghini, Michael J. Gullans, Markus Greiner, Vladan Vuletić, and Mikhail D. Lukin. Logical quantum processor based on reconfigurable atom arrays. *Nature*, 626(7997):58 – 65, 2024.

[12] Yurii B. Ovchinnikov Rudolf Grimm, Matthias Weidemüller. Optical dipole traps for neutral atoms. *Advances In Atomic, Molecular, and Optical Physics*, 42:95–170, 2000.

[13] J. Dalibard and C. Cohen-Tannoudji. Laser cooling below the Doppler limit by polarization gradients: simple theoretical models. *J. Opt. Soc. Am. B*, 6(11):2023–2045, Nov 1989.

[14] K. B. Davis, M. O. Mewes, M. R. Andrews, N. J. van Druten, D. S. Durfee, D. M. Kurn, and W. Ketterle. Bose-einstein condensation in a gas of sodium atoms. *Phys. Rev. Lett.*, 75:3969–3973, Nov 1995.

[15] M. H. Anderson, J. R. Ensher, M. R. Matthews, C. E. Wieman, and E. A. Cornell. Observation of bose-einstein condensation in a dilute atomic vapor. *Science*, 269(5221):198–201, Jul 1995.

[16] Andrew D. Ludlow, Martin M. Boyd, Jun Ye, E. Peik, and P. O. Schmidt. Optical atomic clocks. *Rev. Mod. Phys.*, 87:637–701, Jun 2015.

[17] Nicolas Schlosser, Georges Reymond, Igor Protsenko, and Philippe Grangier. Sub-poissonian loading of single atoms in a microscopic dipole trap. *Nature*, 411(6841):1024–1027, Jun 2001.

[18] Daniel Barredo, Sylvain De Léséleuc, Vincent Lienhard, Thierry Lahaye, and Antoine Browaeys. An atom-by-atom assembler of defect-free arbitrary two-dimensional atomic arrays. *Science*, 354(6315):1021–1023, 2016.

[19] Manuel Endres, Hannes Bernien, Alexander Keesling, Harry Levine, Eric R Anschuetz, Alexandre Krajenbrink, Crystal Senko, Vladan Vuletic, Markus Greiner, and Mikhail D Lukin. Atom-by-atom assembly of defect-free one-dimensional cold atom arrays. *Science*, 354(6315):1024–1027, 2016.

[20] Hyosub Kim, Woojun Lee, Han-gyeol Lee, Hanlae Jo, Yunheung Song, and Jaewook Ahn. In situ single-atom array synthesis using dynamic holographic optical tweezers. *Nature communications*, 7(1):1–8, 2016.

[21] Daniel Barredo, Vincent Lienhard, Sylvain De Leseleuc, Thierry Lahaye, and Antoine Browaeys. Synthetic three-dimensional atomic structures assembled atom by atom. *Nature*, 561(7721):79–82, 2018.

[22] Antoine Browaeys and Thierry Lahaye. Many-body physics with individually controlled rydberg atoms. *Nature Physics*, pages 1–11, 2020.

[23] M. Saffman, T. G. Walker, and K. Mølmer. Quantum information with rydberg atoms. *Rev. Mod. Phys.*, 82:2313–2363, Aug 2010.

[24] Simon J. Evered, Dolev Bluvstein, Marcin Kalinowski, Sepehr Ebadi, Tom Manovitz, Hengyun Zhou, Sophie H. Li, Alexandra A. Geim, Tout T. Wang, Nishad Maskara, Harry Levine, Giulia Semeghini, Markus Greiner, Vladan Vuletić, and Mikhail D. Lukin. High-fidelity parallel entangling gates on a neutral-atom quantum computer. *Nature*, 622(7982):268–272, 2023.

[25] Pascal Scholl, Adam L. Shaw, Richard Bing-Shiun Tsai, Ran Finkelstein, Joonhee Choi, and Manuel Endres. Erasure conversion in a high-fidelity rydberg quantum simulator. *Nature*, 622(7982):273–278, Oct 2023.

[26] Shuo Ma, Genyue Liu, Pai Peng, Bichen Zhang, Sven Jandura, Jahan Claes, Alex P. Burgers, Guido Pupillo, Shruti Puri, and Jeff D. Thompson. High-fidelity gates and mid-circuit erasure conversion in an atomic qubit. *Nature*, 622(7982):279 – 284, 2023.

[27] Sepehr Ebadi, Tout T. Wang, Harry Levine, Alexander Keesling, Giulia Semeghini, Ahmed Omran, Dolev Bluvstein, Rhine Samajdar, Hannes Pichler, Wen Wei Ho, Soonwon Choi, Subir Sachdev, Markus Greiner, Vladan Vuletić, and Mikhail D. Lukin. Quantum phases of matter on a 256-atom programmable quantum simulator. *Nature*, 595(7866):227–232, 2021.

[28] Daniel Ohl de Mello, Dominik Schäffner, Jan Werkmann, Tilman Preuschoff, Lars Kohfahl, Malte Schlosser, and Gerhard Birkl. Defect-free assembly of 2d clusters of more than 100 single-atom quantum systems. *Phys. Rev. Lett.*, 122(20):203601, 2019.

[29] Guillaume Bornet, Gabriel Emperauger, Cheng Chen, Bingtian Ye, Maxwell Block, Marcus Bintz, Jamie A. Boyd, Daniel Barredo, Tommaso Comparin, Fabio Mezzacapo, Tommaso Roscilde, Thierry Lahaye, Norman Y. Yao, and Antoine Browaeys. Scalable spin squeezing in a dipolar rydberg atom array. *Nature*, 621(7980):728–733, 2023.

[30] Elie Bataille Kon H. Leung Xudong Lv Manuel Endres Hannah J. Manetsch, Gyohei Nomura. A tweezer array with 6100 highly coherent atomic qubits, 2024.

[31] Dolev Bluvstein, Harry Levine, Giulia Semeghini, Tout T Wang, Sepehr Ebadi, Marcin Kalinowski, Alexander Keesling, Nishad Maskara, Hannes Pichler, Markus Greiner, Vladan Vuletic, and Mikhail D. Lukin. A quantum processor based on coherent transport of entangled atom arrays. *Nature*, 604:451–456, 2022.

[32] Han-Sen Zhong, Hui Wang, Yu-Hao Deng, Ming-Cheng Chen, Li-Chao Peng, Yi-Han Luo, Jian Qin, Dian Wu, Xing Ding, Yi Hu, Peng Hu, Xiao-Yan Yang, Wei-Jun Zhang, Hao Li, Yuxuan Li, Xiao Jiang, Lin Gan, Guangwen Yang, Lixing You, Zhen Wang, Li Li, Nai-Le Liu, Chao-Yang Lu, and Jian-Wei Pan. Quantum computational advantage using photons. *Science*, 370(6523):1460–1463, Dec 2020.

[33] Alex J. Matthies, Jonathan M. Mortlock, Lewis A. McArd, Adarsh P. Raghuram, Andrew D. Innes, Philip D. Gregory, Sarah L. Bromley, and Simon L. Cornish. Long-distance optical-conveyor-belt transport of ultracold ^{133}Cs and ^{87}Rb atoms. *Phys. Rev. A*, 109:023321, Feb 2024.

[34] M. A. Norcia, H. Kim, W. B. Cairncross, M. Stone, A. Ryou, M. Jaffe, M. O. Brown, K. Barnes, P. Battaglino, A. Brown, K. Cassella, C. A. Chen, R. Coxe, D. Crow, J. Epstein, C. Griger, E. Halperin, F. Hummel, A. M. W. Jones, J. M. Kindem, J. King, K. Kotru, J. Lauigan, M. Li, M. Lu, E. Megidish, J. Marjanovic, M. McDonald, T. Mittiga, J. A. Muniz, S. Narayanaswami, C. Nishiguchi, T. Paule, K. A. Pawlak, L. S. Peng, K. L. Pudenz, A. Smull, D. Stack, M. Urbanek, R. J. M. van de Veerdonk, Z. Vendeiro, L. Wadleigh, T. Wilkason, T. Y. Wu, X. Xie, E. Zalys-Geller, X. Zhang, and B. J. Bloom. Iterative assembly of ^{171}yb atom arrays in cavity-enhanced optical lattices, 2024.

[35] Renhao Tao Hendrik Timme Stepan Snigirev Immanuel Bloch Johannes Zeiher Flavien Gyger, Maximilian Ammenwerth. Continuous operation of large-scale atom arrays in optical lattices, 2024.

[36] Yue Wu, Shimon Kolkowitz, Shruti Puri, and Jeff D. Thompson. Erasure conversion for fault-tolerant quantum computing in alkaline earth rydberg atom arrays. *Nature Communications*, 13(1):4657, Aug 2022.

[37] Thibault Peyronel. Quantum nonlinear optics using cold atomic ensembles. 2013.

[38] Zachary Vendeiro. Raman cooling to high phase space density. 2021.

[39] T. Q. O. Birnbaum, K. Group. Ultra-high vacuum chambers. 2005.

[40] M.D. Lukin. Modern atomic and optical physics ii lecture notes. 2016.

[41] Vasiliy Makhalov, Kirill Martiyanov, Tatiana Barmashova, and Andrey Turlapov. Precision measurement of a trapping potential for an ultracold gas. *Physics Letters A*, 379(4):327–332, Feb 2015.

[42] F. Nogrette, H. Labuhn, S. Ravets, D. Barredo, L. Béguin, A. Vernier, T. Lahaye, and A. Browaeys. Single-atom trapping in holographic 2d arrays of microtraps with arbitrary geometries. *Phys. Rev. X*, 4:021034, May 2014.

[43] Daniel A. Steck. Rubidium 87 d line data, 2001.

[44] Alban Urvoy, Zachary Vendeiro, Joshua Ramette, Albert Adiyatullin, and Vladan Vuletić. Direct laser cooling to Bose-Einstein condensation in a dipole trap. *Phys. Rev. Lett.*, 122(20):203202, 2019.

[45] M. O. Brown, T. Thiele, C. Kiehl, T.-W. Hsu, and C. A. Regal. Gray-molasses optical-tweezer loading: Controlling collisions for scaling atom-array assembly. *Phys. Rev. X*, 9:011057, Mar 2019.

[46] Chang Hoong Chow, Boon Long Ng, Vindhiya Prakash, and Christian Kurtsiefer. Fano resonance in excitation spectroscopy and cooling of an optically trapped single atom. *Phys. Rev. Res.*, 6:023154, May 2024.

[47] Kerman Andrew J. Raman sideband cooling and cold atomic collisions in optical lattices. 2002.

[48] P. B. Wigley, P. J. Everitt, A. van den Hengel, J. W. Bastian, M. A. Sooriyabandara, G. D. McDonald, K. S. Hardman, C. D. Quinlivan, P. Manju, C. C. N. Kuhn, I. R. Petersen, A. N. Luiten, J. J. Hope, N. P. Robins, and M. R. Hush. Fast machine-learning online optimization of ultra-cold-atom experiments. *Scientific Reports*, 6(1):25890, May 2016.

[49] Paul D. Lett, Richard N. Watts, Christoph I. Westbrook, William D. Phillips, Phillip L. Gould, and Harold J. Metcalf. Observation of atoms laser cooled below the doppler limit. *Phys. Rev. Lett.*, 61:169–172, Jul 1988.

[50] C. Tuchendler, A. M. Lance, A. Browaeys, Y. R. P. Sortais, and P. Grangier. Energy distribution and cooling of a single atom in an optical tweezer. *Phys. Rev. A*, 78:033425, Sep 2008.

[51] Erik W. Streed, Andreas Jechow, Benjamin G. Norton, and David Kielpinski. Absorption imaging of a single atom. *Nature Communications*, 3(1):933, Jul 2012.

[52] Adams C.S. Weatherill K.J. Šibalić N., Pritchard J.D. Arc: An open-source library for calculating properties of alkali rydberg atoms. *Computer Physics Communications*, 220:319–331, 2017.

[53] Sebastian Weber, Christoph Tresp, Henri Menke, Alban Urvoy, Ofer Firstenberg, Hans Peter Büchler, and Sebastian Hofferberth. Tutorial: Calculation of Rydberg interaction potentials. *J. Phys. B: At. Mol. Opt. Phys.*, 50(13):133001, 2017.

[54] R. W. P. Drever, J. L. Hall, F. V. Kowalski, J. Hough, G. M. Ford, A. J. Munley, and H. Ward. Laser phase and frequency stabilization using an optical resonator. *Applied Physics B*, 31:97–105, 1983.

[55] C. Klempt, T. van Zoest, T. Henninger, O. Topic, E. Rasel, W. Ertmer, and J. Arlt. Ultraviolet light-induced atom desorption for large rubidium and potassium magneto-optical traps. *Phys. Rev. A*, 73:013410, Jan 2006.

[56] D. Maxwell, D. J. Szwer, D. Paredes-Barato, H. Busche, J. D. Pritchard, A. Gauguet, K. J. Weatherill, M. P. A. Jones, and C. S. Adams. Storage and control of optical photons using rydberg polaritons. *Phys. Rev. Lett.*, 110:103001, Mar 2013.

[57] Jens Honer, R. Löw, Hendrik Weimer, Tilman Pfau, and Hans Peter Büchler. Artificial atoms can do more than atoms: Deterministic single photon subtraction from arbitrary light fields. *Phys. Rev. Lett.*, 107:093601, Aug 2011.

[58] Tony Y. Abi-Salloum. Electromagnetically induced transparency and autler-townes splitting: Two similar but distinct phenomena in two categories of three-level atomic systems. *Phys. Rev. A*, 81:053836, May 2010.

[59] Petr M. Anisimov, Jonathan P. Dowling, and Barry C. Sanders. Objectively discerning autler-townes splitting from electromagnetically induced transparency. *Phys. Rev. Lett.*, 107:163604, Oct 2011.

[60] Anindya Rastogi, Erhan Saglamyurek, Taras Hrushevskyi, Scott Hubele, and Lindsay J. LeBlanc. Discerning quantum memories based on electromagnetically-induced-transparency and autler-townes-splitting protocols. *Phys. Rev. A*, 100:012314, Jul 2019.

[61] Christoph Tresp. Rydberg polaritons and rydberg superatoms-novel tools for quantum nonlinear optics. 2017.

[62] Aditya Vignesh Venkatramani. Quantum nonlinear optics: controlling few-photon interactions. 2020.

[63] Qiyu Liang. Strongly interacting photons via rydberg-rydberg interactions. 2017.

[64] M. Fleischhauer and M. D. Lukin. Dark-state polaritons in electromagnetically induced transparency. *Phys. Rev. Lett.*, 84:5094–5097, May 2000.

[65] Jeff D. Thompson, Travis L. Nicholson, Qi-Yu Liang, Sergio H. Cantu, Aditya V. Venkatramani, Soonwon Choi, Ilya A. Fedorov, Daniel Viscor, Thomas Pohl, Mikhail D. Lukin, and Vladan Vuletić. Symmetry-protected collisions between strongly interacting photons. *Nature*, 542(7640):206–209, Feb 2017.

[66] Stetson Roof, Kasie Kemp, Mark Havey, I. M. Sokolov, and D. V. Kupriyanov. Microscopic lensing by a dense, cold atomic sample. *Optics Letters*, 40(7):1137–1140, Apr 2015.

[67] Giovanna Morigi, Jürgen Eschner, and Christoph H. Keitel. Ground state laser cooling using electromagnetically induced transparency. *Phys. Rev. Lett.*, 85:4458–4461, Nov 2000.

[68] C. F. Roos, D. Leibfried, A. Mundt, F. Schmidt-Kaler, J. Eschner, and R. Blatt. Experimental demonstration of ground state laser cooling with electromagnetically induced transparency. *Phys. Rev. Lett.*, 85:5547–5550, Dec 2000.

[69] Regina Lechner, Christine Maier, Cornelius Hempel, Petar Jurcevic, Ben P. Lanyon, Thomas Monz, Michael Brownnutt, Rainer Blatt, and Christian F. Roos. Electromagnetically-induced-transparency ground-state cooling of long ion strings. *Phys. Rev. A*, 93:053401, May 2016.

[70] Mikhail D Lukin, Michael Fleischhauer, Robin Cote, LM Duan, Dieter Jaksch, J Ignacio Cirac, and Peter Zoller. Dipole blockade and quantum information processing in mesoscopic atomic ensembles. *Phys. Rev. Lett.*, 87(3):037901, 2001.

[71] M Saffman. Quantum computing with atomic qubits and rydberg interactions: progress and challenges. *Journal of Physics B: Atomic, Molecular and Optical Physics*, 49(20):202001, 2016.

[72] M Morgado and S Whitlock. Quantum simulation and computing with rydberg-interacting qubits. *AVS Quantum Science*, 3(2):023501, 2021.

[73] Aishwarya Kumar, Tsung-Yao Wu, Felipe Giraldo, and David S Weiss. Sorting ultracold atoms in a three-dimensional optical lattice in a realization of maxwell's demon. *Nature*, 561(7721):83–87, 2018.

[74] Hannes Bernien, Sylvain Schwartz, Alexander Keesling, Harry Levine, Ahmed Omran, Hannes Pichler, Soonwon Choi, Alexander S Zibrov, Manuel Endres, Markus Greiner, et al. Probing many-body dynamics on a 51-atom quantum simulator. *Nature*, 551(7682):579–584, 2017.

[75] Alexander Keesling, Ahmed Omran, Harry Levine, Hannes Bernien, Hannes Pichler, Soonwon Choi, Rhine Samajdar, Sylvain Schwartz, Pietro Silvi, Subir Sachdev, et al. Quantum kibble–zurek mechanism and critical dynamics on a programmable rydberg simulator. *Nature*, 568(7751):207–211, 2019.

[76] Sepehr Ebadi, Tout T. Wang, Harry Levine, Alexander Keesling, Giulia Semeghini, Ahmed Omran, Dolev Bluvstein, Rhine Samajdar, Hannes Pichler, Wen Wei Ho, Soonwon Choi, Subir Sachdev, Markus Greiner, Vladan Vuletic, and Mikhail D. Lukin. Quantum phases of matter on a 256-atom programmable quantum simulator, 2020.

[77] Pascal Scholl, Michael Schuler, Hannah J. Williams, Alexander A. Eberharter, Daniel Barredo, Kai-Niklas Schymik, Vincent Lienhard, Louis-Paul Henry, Thomas C. Lang, Thierry Lahaye, Andreas M. Läuchli, and Antoine Browaeys. Programmable quantum simulation of 2d antiferromagnets with hundreds of rydberg atoms, 2020.

[78] L Isenhower, E Urban, XL Zhang, AT Gill, T Henage, Todd A Johnson, TG Walker, and M Saffman. Demonstration of a neutral atom controlled-not quantum gate. *Phys. Rev. Lett.*, 104(1):010503, 2010.

[79] TM Graham, M Kwon, B Grinkemeyer, Z Marra, X Jiang, MT Lichtman, Y Sun, M Ebert, and M Saffman. Rydberg-mediated entanglement in a two-dimensional neutral atom qubit array. *Phys. Rev. Lett.*, 123(23):230501, 2019.

[80] Harry Levine, Alexander Keesling, Giulia Semeghini, Ahmed Omran, Tout T Wang, Sepehr Ebadi, Hannes Bernien, Markus Greiner, Vladan Vuletić, Hannes Pichler, et al. Parallel implementation of high-fidelity multiqubit gates with neutral atoms. *Phys. Rev. Lett.*, 123(17):170503, 2019.

[81] D Jaksch, JI Cirac, P Zoller, SL Rolston, R Côté, and MD Lukin. Fast quantum gates for neutral atoms. *Phys. Rev. Lett.*, 85(10):2208, 2000.

[82] Harry Levine, Alexander Keesling, Ahmed Omran, Hannes Bernien, Sylvain Schwartz, Alexander S Zibrov, Manuel Endres, Markus Greiner, Vladan Vuletić, and Mikhail D Lukin. High-fidelity control and entanglement of rydberg-atom qubits. *Phys. Rev. Lett.*, 121(12):123603, 2018.

[83] Ivaylo S Madjarov, Jacob P Covey, Adam L Shaw, Joonhee Choi, Anant Kale, Alexandre Cooper, Hannes Pichler, Vladimir Schkolnik, Jason R Williams, and Manuel Endres. High-fidelity control, detection, and entanglement of alkaline-earth rydberg atoms. *Nature Physics*, 2020.

[84] Ahmed Omran, Harry Levine, Alexander Keesling, Giulia Semeghini, Tout T Wang, Sepehr Ebadi, Hannes Bernien, Alexander S Zibrov, Hannes Pichler, Soonwon Choi, et al. Generation and manipulation of schrödinger cat states in rydberg atom arrays. *Science*, 365(6453):570–574, 2019.

[85] Simon J Devitt, William J Munro, and Kae Nemoto. Quantum error correction for beginners. *Reports on Progress in Physics*, 76(7):076001, 2013.

[86] Thomas F Gallagher. *Rydberg atoms*, volume 3. Cambridge University Press, 2005.

[87] Alpha Gaëtan, Yevhen Miroshnychenko, Tatjana Wilk, Amodsen Chotia, Matthieu Viteau, Daniel Comparat, Pierre Pillet, Antoine Browaeys, and Philippe Grangier. Observation of collective excitation of two individual atoms in the rydberg blockade regime. *Nature Physics*, 5(2):115–118, 2009.

[88] A. Fuhrmanek, Y. R. P. Sortais, P. Grangier, and A. Browaeys. Measurement of the atom number distribution in an optical tweezer using single-photon counting. *Phys. Rev. A*, 82:023623, Aug 2010.

[89] Andrea Bergschneider, Vincent M. Klinkhamer, Jan Hendrik Becher, Ralf Klemt, Gerhard Zürn, Philipp M. Preiss, and Selim Jochim. Spin-resolved single-atom imaging of ^{6}Li in free space. *Phys. Rev. A*, 97:063613, Jun 2018.

[90] G Günter, M Robert-de Saint-Vincent, H Schempp, CS Hofmann, S Whitlock, and M Weidemüller. Interaction enhanced imaging of individual rydberg atoms in dense gases. *Phys. Rev. Lett.*, 108(1):013002, 2012.

[91] Michael Fleischhauer, Atac Imamoglu, and Jonathan P Marangos. Electromagnetically induced transparency: Optics in coherent media. *Reviews of modern physics*, 77(2):633, 2005.

[92] AK Mohapatra, TR Jackson, and CS Adams. Coherent optical detection of highly excited rydberg states using electromagnetically induced transparency. *Phys. Rev. Lett.*, 98(11):113003, 2007.

[93] G Günter, H Schempp, M Robert-de Saint-Vincent, V Gavryusev, S Helmrich, CS Hofmann, S Whitlock, and M Weidemüller. Observing the dynamics of dipole-mediated energy transport by interaction-enhanced imaging. *Science*, 342(6161):954–956, 2013.

[94] Simon Baur, Daniel Tiarks, Gerhard Rempe, and Stephan Dürr. Single-photon switch based on rydberg blockade. *Phys. Rev. Lett.*, 112(7):073901, 2014.

[95] Hannes Gorniaczyk, Christoph Tresp, Johannes Schmidt, Helmut Fedder, and Sebastian Hofferberth. Single-photon transistor mediated by interstate rydberg interactions. *Phys. Rev. Lett.*, 113(5):053601, 2014.

[96] Daniel Tiarks, Simon Baur, Katharina Schneider, Stephan Dürr, and Gerhard Rempe. Single-photon transistor using a förster resonance. *Phys. Rev. Lett.*, 113(5):053602, 2014.

[97] M. Ebert, M. Kwon, T. G. Walker, and M. Saffman. Coherence and rydberg blockade of atomic ensemble qubits. *Phys. Rev. Lett.*, 115:093601, Aug 2015.

[98] Nicholas LR Spong, Yuechun Jiao, Oliver DW Hughes, Kevin J Weatherill, Igor Lesanovsky, and Charles S Adams. The robustness of a collectively encoded rydberg qubit. *arXiv preprint arXiv:2010.11794*, 2020.

[99] E Urban, Todd A Johnson, T Henage, L Isenhower, DD Yavuz, TG Walker, and M Saffman. Observation of rydberg blockade between two atoms. *Nature Physics*, 5(2):110–114, 2009.

[100] M Saffman and TG Walker. Analysis of a quantum logic device based on dipole-dipole interactions of optically trapped rydberg atoms. *Phys. Rev. A*, 72(2):022347, 2005.

[101] Sarah E Anderson and Georg Raithel. Ionization of rydberg atoms by standing-wave light fields. *Nature communications*, 4(1):1–7, 2013.

[102] Michael Schlagmüller, Tara Cubel Liebisch, Felix Engel, Kathrin S. Kleinbach, Fabian Böttcher, Udo Hermann, Karl M. Westphal, Anita Gaj, Robert Löw, Sebastian Hofferberth, Tilman Pfau, Jesús Pérez-Ríos, and Chris H. Greene. Ultracold chemical reactions of a single rydberg atom in a dense gas. *Phys. Rev. X*, 6:031020, Aug 2016.

[103] Thibault Peyronel, Ofer Firstenberg, Qi-Yu Liang, Sebastian Hofferberth, Alexey V. Gorshkov, Thomas Pohl, Mikhail D. Lukin, and Vladan Vuletić. Quantum nonlinear optics with single photons enabled by strongly interacting atoms. *Nature*, 488(7409):57–60, 2012.

[104] Vera Bendkowsky, Björn Butscher, Johannes Nipper, James P Shaffer, Robert Löw, and Tilman Pfau. Observation of ultralong-range rydberg molecules. *Nature*, 458(7241):1005–1008, 2009.

[105] Clément Sayrin, Igor Dotsenko, Xingxing Zhou, Bruno Peaudecerf, Théo Rybarczyk, Sébastien Gleyzes, Pierre Rouchon, Mazyar Mirrahimi, Hadis Amini, Michel Brune, et al. Real-time quantum feedback prepares and stabilizes photon number states. *Nature*, 477(7362):73–77, 2011.

[106] Giovanni Barontini, Leander Hohmann, Florian Haas, Jérôme Estève, and Jakob Reichel. Deterministic generation of multiparticle entanglement by quantum zeno dynamics. *Science*, 349(6254):1317–1321, 2015.

[107] ZK Minev, SO Mundhada, Shyam Shankar, Philip Reinhold, Ricardo Gutiérrez-Jáuregui, RJ Schoelkopf, Mazyar Mirrahimi, HJ Carmichael, and MH Devoret. To catch and reverse a quantum jump mid-flight. *Nature*, 570(7760):200–204, 2019.

[108] Johannes Zeiher, Peter Schauß, Sebastian Hild, Tommaso Macrì, Immanuel Bloch, and Christian Gross. Microscopic characterization of scalable coherent rydberg superatoms. *Phys. Rev. X*, 5:031015, Aug 2015.

[109] Y Wang, S Shevate, TM Wintermantel, M Morgado, G Lochead, and S Whitlock. Preparation of hundreds of microscopic atomic ensembles in optical tweezer arrays. *New J. Phys.*, 6:54, 2020.

[110] Alexander D Cronin, Jörg Schmiedmayer, and David E Pritchard. Optics and interferometry with atoms and molecules. *Reviews of Modern Physics*, 81(3):1051, 2009.

[111] Kai Bongs, Michael Holynski, Jamie Vovrosh, Philippe Bouyer, Gabriel Condon, Ernst Rasel, Christian Schubert, Wolfgang P Schleich, and Albert Roura. Taking atom interferometric quantum sensors from the laboratory to real-world applications. *Nature Reviews Physics*, 1(12):731–739, 2019.

[112] Immanuel Bloch, Jean Dalibard, and Wilhelm Zwerger. Many-body physics with ultracold gases. *Rev. Mod. Phys.*, 80(3):885, 2008.

[113] Immanuel Bloch, Jean Dalibard, and Sylvain Nascimbene. Quantum simulations with ultracold quantum gases. *Nature Physics*, 8(4):267–276, 2012.

[114] Mark Kasevich and Steven Chu. Laser cooling below a photon recoil with three-level atoms. *Phys. Rev. Lett.*, 69:1741–1744, Sep 1992.

[115] Wolfgang Ketterle and N.J. Van Druten. Evaporative cooling of trapped atoms. volume 37 of *Advances In Atomic, Molecular, and Optical Physics*, pages 181–236. Academic Press, 1996.

[116] Simon Stellmer, Benjamin Pasquiou, Rudolf Grimm, and Florian Schreck. Laser cooling to quantum degeneracy. *Phys. Rev. Lett.*, 110(26):263003, 2013.

[117] Chun-Chia Chen, Rodrigo González Escudero, Jiří Minář, Benjamin Pasquiou, Shayne Bennetts, and Florian Schreck. Continuous Bose–Einstein condensation. *Nature*, pages 1–5, 2022.

[118] Gregory A. Phelps, Anne Hébert, Aaron Krahn, Susannah Dickerson, Furkan Öztürk, Sepehr Ebadi, Lin Su, and Markus Greiner. Sub-second production of a quantum degenerate gas, 2020.

[119] Jiazhong Hu, Alban Urvoy, Zachary Vendeiro, Valentin Crépel, Wenlan Chen, and Vladan Vuletić. Creation of a Bose-condensed gas of ^{87}Rb by laser cooling. *Science*, 358(6366):1078–1080, 2017.

[120] Zachary Vendeiro, Joshua Ramette, Alyssa Rudelis, Michelle Chong, Josiah Sinclair, Luke Stewart, Alban Urvoy, and Vladan Vuletić. Machine-learning-accelerated Bose-Einstein condensation. *Phys. Rev. Res.*, 4:043216, Dec 2022.

[121] K. Burnett, P. S. Julienne, and K.-A. Suominen. Laser-driven collisions between atoms in a Bose-Einstein Condensed Gas. *Phys. Rev. Lett.*, 77:1416–1419, Aug 1996.

[122] Andrew J. Kerman, Vladan Vuletić, Cheng Chin, and Steven Chu. Beyond optical molasses: 3d raman sideband cooling of atomic cesium to high phase-space density. *Phys. Rev. Lett.*, 84:439–442, Jan 2000.

[123] J. Reichel, O. Morice, G. M. Tino, and C. Salomon. Subrecoil raman cooling of cesium atoms. *Europhysics Letters*, 28(7):477, dec 1994.

[124] Pablo Solano, Yiheng Duan, Yu-Ting Chen, Alyssa Rudelis, Cheng Chin, and Vladan Vuletić. Strongly correlated quantum gas prepared by direct laser cooling. *Phys. Rev. Lett.*, 123:173401, Oct 2019.

[125] Tino Weber, Jens Herbig, Michael Mark, Hanns-Christoph Nagerl, and Rudolf Grimm. Bose-Einstein condensation of cesium. *Science*, 299(5604):232–235, 2003.

[126] Toshiya Kinoshita, Trevor Wenger, and David S Weiss. All-optical Bose-Einstein condensation using a compressible crossed dipole trap. *Phys. Rev.* **A**, 71(1):011602, 2005.

[127] Dizhou Xie, Dongyue Wang, Wei Gou, Wenhao Bu, and Bo Yan. Fast production of rubidium Bose–Einstein condensate in a dimple trap. *JOSA B*, 35(3):500–503, 2018.

[128] DM Stamper-Kurn, H-J Miesner, AP Chikkatur, S Inouye, J Stenger, and W Ketterle. Reversible formation of a Bose-Einstein condensate. *Phys. Rev. Lett.*, 81(11):2194, 1998.

[129] S. L. Cornish, N. R. Claussen, J. L. Roberts, E. A. Cornell, and C. E. Wieman. Stable ^{85}Rb Bose-Einstein condensates with widely tunable interactions. *Phys. Rev. Lett.*, 85:1795–1798, Aug 2000.

[130] E. A. Burt, R. W. Ghrist, C. J. Myatt, M. J. Holland, E. A. Cornell, and C. E. Wieman. Coherence, correlations, and collisions: What one learns about bose-einstein condensates from their decay. *Phys. Rev. Lett.*, 79:337–340, Jul 1997.

[131] G. Salomon, L. Fouché, P. Wang, A. Aspect, P. Bouyer, and T. Bourdel. Gray-molasses cooling of ^{39}K to a high phase-space density. *Europhysics Letters*, 104(6):63002, jan 2014.

[132] Yin Hsien Fung, Pimonpan Sompet, and Mikkel F. Andersen. Single atoms preparation using light-assisted collisions. *Technologies*, 4(1), 2016.

[133] D Jacob, E Mimoun, L De Sarlo, M Weitz, J Dalibard, and F Gerbier. Production of sodium Bose–Einstein condensates in an optical dimple trap. *New Journal of Physics*, 13(6):065022, jun 2011.

[134] A Fuhrmanek, R Bourgain, Yvan RP Sortais, and Antoine Browaeys. Light-assisted collisions between a few cold atoms in a microscopic dipole trap. *Phys. Rev.* **A**, 85(6):062708, 2012.

[135] Michael Berry, Nikolay Zheludev, Yakir Aharonov, Fabrizio Colombo, Irene Sabadini, Daniele C Struppa, Jeff Tollaksen, Edward T F Rogers, Fei Qin, Minghui Hong, Xiangang Luo, Roei Remez, Ady Arie, Jörg B Götte, Mark R Dennis, Alex M H Wong, George V Eleftheriades, Yaniv Eliezer, Alon Bahabad, Gang Chen, Zhongquan Wen, Gaofeng Liang, Chenglong Hao, C-W Qiu, Achim Kempf, Eytan Katzav, and Moshe Schwartz. Roadmap on superoscillations. *Journal of Optics*, 21(5):053002, apr 2019.

[136] Edward T. F. Rogers, Jari Lindberg, Tapashree Roy, Salvatore Savo, John E. Chad, Mark R. Dennis, and Nikolay I. Zheludev. A super-oscillatory lens optical microscope for subwavelength imaging. *Nature Materials*, 11(5):432–435, 2012.

[137] Saptarishi Chaudhuri, Sanjukta Roy, and C. S. Unnikrishnan. Realization of an intense cold rb atomic beam based on a two-dimensional magneto-optical trap: Experiments and comparison with simulations. *Phys. Rev. A*, 74:023406, Aug 2006.

[138] Mark Kasevich and Steven Chu. Atomic interferometry using stimulated raman transitions. *Phys. Rev. Lett.*, 67:181–184, Jul 1991.

[139] Holger Müller, Sheng-wey Chiow, Sven Herrmann, Steven Chu, and Keng-Yeow Chung. Atom-interferometry tests of the isotropy of post-newtonian gravity. *Phys. Rev. Lett.*, 100:031101, Jan 2008.

[140] Sylvain de Léséleuc, Vincent Lienhard, Pascal Scholl, Daniel Barredo, Sebastian Weber, Nicolai Lang, Hans Peter Büchler, Thierry Lahaye, and Antoine Browaeys. Observation of a symmetry-protected topological phase of interacting bosons with rydberg atoms. *Science*, 365(6455):775–780, 2019.

[141] William J. Eckner, Nelson Darkwah Oppong, Alec Cao, Aaron W. Young, William R. Milner, John M. Robinson, Jun Ye, and Adam M. Kaufman. Realizing spin squeezing with rydberg interactions in an optical clock. *Nature*, 621(7980):734–739, 2023.

[142] Jacob A. Hines, Shankari V. Rajagopal, Gabriel L. Moreau, Michael D. Wahrman, Neomi A. Lewis, Ognjen Marković, and Monika Schleier-Smith. Spin squeezing by rydberg dressing in an array of atomic ensembles. *Phys. Rev. Lett.*, 131:063401, Aug 2023.

[143] Kritsana Srakaew, Pascal Weckesser, Simon Hollerith, David Wei, Daniel Adler, Immanuel Bloch, and Johannes Zeiher. A subwavelength atomic array switched by a single rydberg atom. *Nature Physics*, 19(5):714–719, May 2023.

[144] Julien Vaneecloo, Sébastien Garcia, and Alexei Ourjoumtsev. Intracavity rydberg superatom for optical quantum engineering: Coherent control, single-shot detection, and optical π phase shift. *Phys. Rev. X*, 12:021034, May 2022.

[145] Mohammadsadegh Khazali, Callum R. Murray, and Thomas Pohl. Polariton exchange interactions in multichannel optical networks. *Phys. Rev. Lett.*, 123:113605, Sep 2019.

[146] Andreas Schreiber, Aurél Gábris, Peter P. Rohde, Kaisa Laiho, Martin Štefaňák, Václav Potoček, Craig Hamilton, Igor Jex, and Christine Silberhorn. A 2d quantum walk simulation of two-particle dynamics. *Science*, 336(6077):55–58, Apr 2012.

[147] C. Tresp, P. Bienias, S. Weber, H. Gorniaczyk, I. Mirgorodskiy, H. P. Büchler, and S. Hofferberth. Dipolar dephasing of rydberg d-state polaritons. *Phys. Rev. Lett.*, 115:083602, Aug 2015.

[148] Wenchao Xu, Aditya V. Venkatramani, Sergio H. Cantú, Tamara Šumarac, Valentin Klüsener, Mikhail D. Lukin, and Vladan Vuletić. Fast preparation and detection of a rydberg qubit using atomic ensembles. *Phys. Rev. Lett.*, 127:050501, Jul 2021.

[149] Charles S Adams, Jonathan D Pritchard, and James P Shaffer. Rydberg atom quantum technologies. *Journal of Physics B: Atomic, Molecular and Optical Physics*, 53(1):012002, 2019.

[150] Katrina Barnes, Peter Battaglino, Benjamin J. Bloom, Kayleigh Cassella, Robin Coxe, Nicole Crisosto, Jonathan P. King, Stanimir S. Kondov, Krish Kotru, Stuart C. Larsen, Joseph Lauigan, Brian J. Lester, Mickey McDonald, Eli Megidish, Sandeep Narayanaswami, Ciro Nishiguchi, Remy Notermans, Lucas S. Peng, Albert Ryou, Tsung-Yao Wu, and Michael Yarwood. Assembly and coherent control of a register of nuclear spin qubits. *Nature Communications*, 13(1):2779, May 2022.

[151] Neville Chen, Lintao Li, William Huie, Mingkun Zhao, Ian Vetter, Chris H. Greene, and Jacob P. Covey. Analyzing the rydberg-based optical-metastable-ground architecture for ^{171}Yb nuclear spins. *Phys. Rev. A*, 105:052438, May 2022.

[152] William Huie, Lintao Li, Neville Chen, Xiye Hu, Zhubing Jia, Won Kyu Calvin Sun, and Jacob P. Covey. Repetitive readout and real-time control of nuclear spin qubits in ^{171}Yb atoms. *PRX Quantum*, 4:030337, Sep 2023.

[153] B. J. Lester, A. M. Kaufman, and C. A. Regal. Raman cooling imaging: Detecting single atoms near their ground state of motion. *Phys. Rev. A*, 90:011804, Jul 2014.

[154] Y. S. Patil, S. Chakram, L. M. Aycock, and M. Vengalattore. Nondestructive imaging of an ultracold lattice gas. *Phys. Rev. A*, 90:033422, Sep 2014.

[155] Karl N. Blodgett, David Peana, Saumitra S. Phatak, Lane M. Terry, Maria Paula Montes, and Jonathan D. Hood. Imaging a ^{6}Li atom in an optical tweezer 2000 times with Λ-enhanced gray molasses. *Phys. Rev. Lett.*, 131:083001, Aug 2023.

[156] Jackson Ang'ong'a, Chenxi Huang, Jacob P. Covey, and Bryce Gadway. Gray molasses cooling of ^{39}K atoms in optical tweezers. *Phys. Rev. Res.*, 4:013240, Mar 2022.

[157] Elmar Haller, James Hudson, Andrew Kelly, Dylan A. Cotta, Bruno Peaudecerf, Graham D. Bruce, and Stefan Kuhr. Single-atom imaging of fermions in a quantum-gas microscope. *Nature Physics*, 11(9):738–742, Sep 2015.

[158] B. Nikolov, E. Diamond-Hitchcock, J. Bass, N. L. R. Spong, and J. D. Pritchard. Randomized benchmarking using nondestructive readout in a two-dimensional atom array. *Phys. Rev. Lett.*, 131:030602, Jul 2023.

[159] Minho Kwon, Matthew F. Ebert, Thad G. Walker, and M. Saffman. Parallel low-loss measurement of multiple atomic qubits. *Phys. Rev. Lett.*, 119:180504, Oct 2017.

[160] Chang Hoong Chow, Boon Long Ng, Vindhiya Prakash, and Christian Kurtsiefer. Fano resonance in excitation spectroscopy and cooling of an optically trapped single atom. *Phys. Rev. Res.*, 6:023154, May 2024.

[161] T. M. Graham, Y. Song, J. Scott, C. Poole, L. Phuttitarn, K. Jooya, P. Eichler, X. Jiang, A. Marra, B. Grinkemeyer, M. Kwon, M. Ebert, J. Cherek, M. T. Lichtman, M. Gillette, J. Gilbert, D. Bowman, T. Ballance, C. Campbell, E. D. Dahl, O. Crawford, N. S. Blunt, B. Rogers, T. Noel, and M. Saffman. Multi-qubit entanglement and algorithms on a neutral-atom quantum computer. *Nature*, 604(7906):457–462, Apr 2022.

[162] Wenchao Xu, Tamara Šumarac, Emily H. Qiu, Matthew L. Peters, Sergio H. Cantú, Zeyang Li, Adrian Menssen, Mikhail D. Lukin, Simone Colombo, and Vladan Vuletić. Bose-einstein condensation by polarization gradient laser cooling. *Phys. Rev. Lett.*, 132:233401, Jun 2024.

[163] Sara Rosi, Alessia Burchianti, Stefano Conclave, Devang S. Naik, Giacomo Roati, Chiara Fort, and Francesco Minardi. λ-enhanced grey molasses on the d2 transition of rubidium-87 atoms. *Scientific Reports*, 8(1):1301, Jan 2018.

[164] David Peana Meng Raymond Chen Jonathan D. Hood Saumitra S. Phatak, Karl N. Blodgett. A generalized theory for optical cooling of a trapped atom with spin, 2024.

[165] S. Zhang, F. Robicheaux, and M. Saffman. Magic-wavelength optical traps for rydberg atoms. *Phys. Rev. A*, 84:043408, Oct 2011.

[166] F Robicheaux. Ionization due to the interaction between two rydberg atoms. *Journal of Physics B: Atomic, Molecular and Optical Physics*, 38(2):S333, 2005.

[167] Wenhui Li, Paul J Tanner, and Thomas F Gallagher. Dipole-dipole excitation and ionization in an ultracold gas of rydberg atoms. *Phys. Rev. Lett.*, 94(17):173001, 2005.

[168] Martin Kiffner, Davide Ceresoli, Wenhui Li, and Dieter Jaksch. Quantum mechanical calculation of rydberg–rydberg autoionization rates. *Journal of Physics B: Atomic, Molecular and Optical Physics*, 49(20):204004, 2016.

[169] Michiteru Mizoguchi, Yichi Zhang, Masaya Kunimi, Akira Tanaka, Shuntaro Takeda, Nobuyuki Takei, Vineet Bharti, Kuniaki Koyasu, Tetsuo Kishimoto, Dieter Jaksch, et al. Ultrafast creation of overlapping rydberg electrons in an atomic bec and mott-insulator lattice. *Physical Review Letters*, 124(25):253201, 2020.

[170] Philipp Neumann, Johannes Beck, Matthias Steiner, Florian Rempp, Helmut Fedder, Philip R. Hemmer, Jörg Wrachtrup, and Fedor Jelezko. Single-shot readout of a single nuclear spin. *Science*, 329(5991):542–544, 2010.

[171] Vladimir B Braginsky and F Ya Khalili. Quantum nondemolition measurements: the route from toys to tools. *Reviews of Modern Physics*, 68(1):1, 1996.

[172] A. D. Tranter, H. J. Slatyer, M. R. Hush, A. C. Leung, J. L. Everett, K. V. Paul, P. Vernaz-Gris, P. K. Lam, B. C. Buchler, and G. T. Campbell. Multiparameter optimisation of a magneto-optical trap using deep learning. *Nature Communications*, 9(1):4360, Oct 2018.

[173] Franco Dalfovo, Stefano Giorgini, Lev P. Pitaevskii, and Sandro Stringari. Theory of bose-einstein condensation in trapped gases. *Rev. Mod. Phys.*, 71:463–512, Apr 1999.

[174] Sylvain de Léséleuc, Daniel Barredo, Vincent Lienhard, Antoine Browaeys, and Thierry Lahaye. Optical control of the resonant dipole-dipole interaction between rydberg atoms. *Phys. Rev. Lett.*, 119:053202, Aug 2017.

[175] Thad G. Walker and M. Saffman. Consequences of zeeman degeneracy for the van der waals blockade between rydberg atoms. *Phys. Rev. A*, 77:032723, Mar 2008.

[176] Sylvain de Léséleuc, Sebastian Weber, Vincent Lienhard, Daniel Barredo, Hans Peter Büchler, Thierry Lahaye, and Antoine Browaeys. Accurate mapping of multilevel rydberg atoms on interacting spin-1/2 particles for the quantum simulation of ising models. *Phys. Rev. Lett.*, 120:113602, Mar 2018.